Magnetization Dynamics of Confined Ferromagnetic Systems

Dissertation

zur Erlangung des Doktorgrades
der Naturwissenschaften (Dr. rer. nat.)
der Fakultät Physik
der Universität Regensburg

vorgelegt von

Ingo Neudecker

aus Trostberg

2006

Promotionsgesuch eingereicht am: 22.03.2006

Tag der mündlichen Prüfung: 17.05.2006

Die Arbeit wurde angeleitet von: Prof. Dr. C. H. Back

Prüfungsausschuss:

Vorsitzender: Prof. Dr. J. Schliemann
1. Gutachter: Prof. Dr. C. H. Back
2. Gutachter: Prof. Dr. D. Weiss
Prüfer: Prof. Dr. S. Ganichev

Contents

Glossary

Acronyms:

BLS	Brillouin Light Scattering
cw	continuous wave
DUT	Device Under Test
FMR	FerroMagnetic Resonance
FT	Fourier Transform
HWHM	Half Width at Half Maximum
hf	high frequency
LL	Landau-Lifshitz
LLG	Landau-Lifshitz-Gilbert
ML	Mono Layer
MOKE	Magneto-Optical Kerr Effect
MSBVW	MagnetoStatic Backward Volume Wave
MSSW	MagnetoStatic Surface Wave
OOMMF	Object Oriented MicroMagnetic Framework
PIMM	Pulsed Inductive Microwave Magnetometry
Py	permalloy ($Ni_{81}Fe_{19}$)
RHEED	Reflection High Energy Electron Diffraction
SKEM	Scanning KErr Microscopy
SNR	Signal to Noise Ratio
SQUID	Superconducting Quantum Interference Device
TR	Time Resolved
VNA	Vector Network Analyzer

Physical constants:

$\mathrm{dB} = 10\ log_{10}(P_{\mathrm{out}}/P_{\mathrm{in}})$	decibel
ε_0	electric permittivity of free space
g	g-factor
$\gamma = g\,\mu_B/h\ = g \times 13.996$ GHz/T	gyromagnetic ratio
$\hbar = h/2\pi$	Planck's constant divided by 2π
$\mu_B = \lvert e\rvert\,\hbar/(2m_e)\ = 9.274 \times 10^{-24}$ Am^2	Bohr magneton
m_e	electron mass
$\mu_0 = 4\pi \times 10^{-7}$ Vs/Am	Permeability

Symbols:

$A = 2J\,S^2\,p/a$	exchange constant
a	nearest neighbor distance
α	damping constant
α_x, α_y, α_z,	directional cosines
$\boldsymbol{B}$	vector of magnetic induction
χ	susceptibility
d	diameter
D_M	effective demagnetizing factor
E	energy
$\varepsilon = E/V$	energy density
f	precessional frequency
F	area
Φ	magnetic flux
$\boldsymbol{H}$	magnetic field vector
$\boldsymbol{h}$	high frequency exciting field vector
IF	intermediate frequency
J	exchange integral
K	anisotropy constant
k	wave vector
$\boldsymbol{L}$	angular momentum vector
l_{ex}	exchange length
$\boldsymbol{M}$	magnetization vector
m, n	number of azimuthal and radial nodes
$\boldsymbol{m} = \boldsymbol{M}/M_{\mathrm{S}}$	reduced magnetization vector
m_l	orbital angular momentum quantum number
M_{S}	saturation magnetization
m_s	spin momentum quantum number
N_x, N_y, N_z	demagnetizing factors
$\omega = 2\pi f$	angular frequency
p	number of sites in the unit cell
P	power
$\boldsymbol{S}$	spin operator
S_{ij}	scattering parameter
s	separation
t	thickness
V	volume
w	signal line width of a coplanar waveguide

All equations and constants in the present work are expressed in SI units [1].

1 Introduction

In recent years an enormous technological progress has been made in the field of fabricating high quality thin films as well as laterally confined elements. By means of lithographical processes, the miniaturization has been pushed down well into the nanometer regime. For applications, this progress amounts to formidable challenges for magneto-electrical devices. Most applications are geared towards novel magnetic recording media as well as sensors [2–4]. Due to its promises concerning speed, storage density, and non-volatility, advanced magnetic recording technology is thought to have the potential to become the long-awaited universal memory. In order to achieve high storage density the memory cells call for small magnetic elements which ideally are free of magnetic stray field and hence avoid crosstalk with neighboring cells. This in turn requires to reduce the dimensions of the single storage cell down into the micrometer or even nanometer size regime. Moreover, since switching times need to be pushed into the gyromagnetic regime, a detailed comprehension of the response of small magnetic elements to high frequency magnetic fields is a central question. For this reason the identification of the excitation spectrum of ferromagnetic elements in the micro- and even nanometer lateral length scale [5–24] as well as the investigation of their switching behavior in the precessional regime [25–27] has attracted much attention in recent years. While these problems can be addressed in the frequency domain using Brillouin Light Scattering (BLS) or Ferromagnetic Resonance (FMR) techniques [7, 28, 29], a direct imaging of the magnetic excitations on the picosecond time scale is presently only possible by Time Resolved Scanning Kerr Microscopy (TR-SKEM) [8, 16, 30] or micro-focus BLS [24, 31] experiments.
The aim of this thesis is to illustrate the effects of reducing the dimensions of a ferromagnetic system on the dynamic response to microwave magnetic fields. As experimental access to the magnetization dynamics, inductive as well as spatially resolved optical techniques are employed. The microwave response is studied either in the time domain by applying a short magnetic field pulse or in the frequency domain by applying a sinusoidal magnetic excitation. Unless the magnetic excitations are eigenmodes of the system, the dynamic response obtained from the two complementary techniques should be transformable into each other via Fourier transformation.

The thesis is organized as follows:
Chapter 2 gives a brief introduction to the physics of magnetism and the relevant concepts of magnetization dynamics.
The employed experimental setups are described in **Chapter 3**. In the first part of this chapter the details concerning the inductive techniques are provided. In doing so, the differences between the various approaches are discussed, namely the conventional Ferromagnetic Resonance (FMR), the novel Vector Network Analyzer Ferromagnetic

Resonance (VNA-FMR), and the Pulsed Inductive Microwave Magnetometry (PIMM) technique. In the second part of Chapter 3 the spatially resolved optical techniques are described. Two different attempts are employed: while for TR-SKEM the magnetization is disturbed by means of a short magnetic field pulse, a sinusoidal excitation is applied for the ferromagnetic resonance-SKEM setup. At the end of Chapter 3 a brief introduction to micromagnetic simulations is given.
Chapter 4 reports of the effect on the dynamic response when confining the dimension of a magnetic system perpendicular to its substrate. A well characterized ultrathin Fe film prepared on GaAs(001) is studied by both inductive and optical techniques. First, the results from VNA-FMR measurements are analyzed by emphasizing the characteristic features of this novel inductive technique. Subsequently, the data from VNA-FMR are compared to the experimental results from PIMM, TR-SKEM, and conventional FMR in terms of frequency and damping of the resonant response. Finally, the various techniques are compared with respect to their signal to noise ratio.
In **Chapter 5** the influence of additionally confining the lateral dimensions on the magnetization dynamics is addressed. The microwave response of cylindrical disks is studied both in the remanent vortex state and as a function of an externally applied magnetic in-plane bias field. First, thin permalloy disks with a diameter of 200 nm are studied by means of inductive VNA-FMR and BLS technique. The VNA-FMR measurements demonstrate the potential of this technique for the investigation of nano-structured elements with nonuniform magnetization configuration. The observed modes are identified by comparing the data to numerical calculations. In the second part of Chapter 5 the experimentally revealed modal patterns of cylindrical disks are presented and discussed by means of disks with 4 μm diameter. Inductive as well as spatially resolved optical techniques yield a very comprehensive description of the microwave response both at zero field and as a function of an external bias field. In order to confirm the experimental results they are compared to micromagnetic simulations. The normal mode structure of the cylindrical disks investigated in Chapter 5 was found to alter when the disk center is removed and the perpendicular component in this region is absent. In this case a ring structure is obtained which should be free of stray field for the flux-closure magnetization configuration. In such a structure neighboring elements are do not influence each other statically, which might prove useful for high density storage media [2]. Therefore, ring structures have been intensively investigated, recently in terms of their static properties [32–36]. However, for high speed memory and sensor applications the dynamic properties are of paramount interest. In **Chapter 6** the microwave response of Co ring elements is presented and discussed. Using inductive VNA-FMR and spatially resolved optical FMR-SKEM techniques the eigenmode spectrum of the ring structures is determined again both in their remanent states and as a function of an external in-plane bias field. Finally the effect of dynamic inter-ring coupling on the modes in their remanent states is evinced. The experimental results are again confirmed by those from micromagnetic simulations.

The thesis closes with a summary and an outlook.

2 Theory

2.1 Introduction to Magnetism and Magnetostatics

In Sep. 1888 O. Smith was the first to publish a description of a magnetic recording device. Indeed, only a few decades later magnetic recording became one of the most important techniques of information storage [37]. This was, however, not the first application of magnetic properties. The appearance of magnetism was already mentioned 600 BC by Greek philosophers and its ability to align in the Earth magnetic field when freely suspended, was used for compasses around 1000 AD. Despite this early application the microscopic origin of magnetism was hidden until the development of quantum mechanics, since in fact magnetism is a purely quantum mechanical phenomenon.
The aim of this section is to briefly introduce the principle mechanisms responsible for the appearance of magnetism. In solid states, magnetism mainly originates from the magnetic properties of the electrons. Partly, the magnetic moment of the electron is mediated by the angular momentum associated with its motion around the nucleus. The component of this *orbital* angular momentum along a distinct axis (usually one chooses the z-axis) is defined by the quantum number m_l and is given by $m_l\hbar$, where $\hbar$ is Planck's constant divided by 2π. Associated with this angular momentum the electron has a magnetic moment along the z-axis of

$$-\, g_l\, m_l\, \mu_\mathrm{B}, \tag{2.1}$$

where $\mu_\mathrm{B} = e\hbar/(2m_e)$ is the Bohr magneton and g_l being the g-factor of the *orbital* momentum. Moreover, in addition to the *orbital* angular momentum the electron possesses an intrinsic angular momentum called *spin*. It is accounted for by the spin quantum number $m_s = \pm 1/2$, which defines the component of the spin angular momentum along a fixed direction (again the z-axis) given by $m_s\hbar$. The associated magnetic moment along the z-axis reads

$$g_s\, m_s\, \mu_\mathrm{B}, \tag{2.2}$$

where $g_s = 2$ is the g-factor of the electron spin.
In the following subsections at first, the mechanisms of the different magnetic interactions are discussed. Since magnetism is a collective phenomenon, the magnetic moments need to communicate with each other. The responsible mechanisms for the different possible interactions are outlined in the following subsections. The contributions to the free energy defined by these interactions are conferred in the second part of this section. Their detailed knowledge is crucial in order to derive the equilibrium orientation of the magnetic moments.

2.1.1 Magnetic Interactions

This subsection outlines the origin of magnetic interactions by emphasizing ferromagnetic ordering, since ferromagnets are the subject of this research project.

- **Magnetic dipolar Interaction**

  Consider two magnetic dipoles $\boldsymbol{\mu}_1$ and $\boldsymbol{\mu}_2$, each immersed in the magnetic field generated by the other dipole. In this case the corresponding magnetic energy reads [1]

  $$E_{\text{dipole}} = \frac{\mu_0}{4\pi r^3}\left[\boldsymbol{\mu}_1 \cdot \boldsymbol{\mu}_2 - \frac{3}{r^2}(\boldsymbol{\mu}_1 \cdot \boldsymbol{r})(\boldsymbol{\mu}_2 \cdot \boldsymbol{r})\right], \tag{2.3}$$

  where μ_0 is the permeability. Since $\boldsymbol{r}$ is the vector connecting the two dipoles, the energy decreases with the 3^{rd} order of their distance. Its magnitude additionally depends on the mutual orientation of the dipoles and is of the order of approximately 10^{-6} eV for two neighboring atomic moments, which corresponds to a temperature of $\sim$ 1 K. Indeed, ferromagnetic ordering is observed up to $\sim$ 1000 K, so that dipolar interaction is not sufficient for the observed long range order, in general. However, as it is shown later in this chapter, dipolar interaction is accountable for effects such as demagnetizing field and spin waves in the long wave length regime.

- **Exchange Interaction**

  When assuming two electrons with overlapping wave functions, their electronic states are inevitably correlated. As a consequence, their common wave function has to be antisymmetric. This indeed is an alternative way of formulating Pauli's exclusion principle, since it implies the probability to find two electrons with parallel spins in the same state to vanish. Therefore, the Coulomb energy of electrons with parallel spins is lowered on account of their spatial separation. The corresponding exchange energy of two electrons with spin operators $\hat{S}_1$ and $\hat{S}_2$ can be expressed as

  $$E_{\text{ex}} = -2J_{12}\hat{S}_1 \cdot \hat{S}_2, \tag{2.4}$$

  where J_{12} denotes the exchange integral. For $J_{12} > 0$ the interaction causes parallel alignment of the spins, which corresponds to ferromagnetic ordering. In a continuum approximation of the crystal lattice, the exchange energy of a cubic crystal is given by [1]

  $$E_{\text{ex}} = A \int \mathrm{d}V (\nabla \boldsymbol{m})^2, \tag{2.5}$$

  with the exchange constant $A = 2\,J\,S^2\,p/a$ and the normalized magnetization $\boldsymbol{m} = \boldsymbol{M}/M_{\text{S}}$. $\boldsymbol{M}$ and M_{S} being the magnetization vector and the saturation magnetization, respectively. The exchange integral is J, the distance between the nearest neighbors is a, and the number of sites in the unit cell is denoted by p.
  Since the exchange constant depends on the overlap of the single electron wave

functions, which is taken into account by a, J generally vanishes except for neighboring electrons. Consequently, the exchange interaction is only very short ranged. However, due its magnitude which is of the order of 10^{-2} eV, it can exclusively account for magnetic long range ordering and causes a mutual alignment of the permanent magnetic moments below a critical temperature.

- **Spin-Orbit Interaction**

  As already discussed in the introduction to this chapter, electrons generally have an orbital magnetic moment (see Eq. 2.1) arising from their angular momentum, and a spin magnetic moment (see Eq. 2.2) mediated by their intrinsic spin momentum. The spin magnetic moment of the electron indeed interacts with its own orbital magnetic moment. This coupling is referred to as spin-orbit interaction and causes a splitting of the electronic states. For hydrogen-like atoms the energy splitting due to spin-orbit interaction reads [1]

$$E_{\mathrm{SO}} = \beta \frac{\langle \boldsymbol{S} \cdot \boldsymbol{L} \rangle}{n^3 l(l+1/2)(l+1)}, \tag{2.6}$$

  with n and l being the principle and angular momentum quantum numbers, respectively. The angular and the spin moment are given by $\hbar \boldsymbol{L}$ and $\hbar \boldsymbol{S}$, respectively. The pre-factor β is

$$\beta = \frac{Z^4 e^2 \hbar^2}{4\pi\varepsilon_0 a_0^3}, \tag{2.7}$$

  where Z is the atomic number and a_0 is the Bohr radius. For atoms in a crystal lattice the magnitude of the splitting is of the order of 10^{-4} to 10^{-3} eV.
  Since the arrangement of the atomic orbitals is determined by the atomic ordering within the crystal lattice, the orientation of the angular magnetic moments in turn is determined by the crystal symmetry. Consequently, by virtue of spin-orbit interaction the crystal symmetry is mediated to the spin system, which represents one origin of magnetic anisotropies. Moreover, by linking the spin system to the crystal lattice, spin-orbit coupling represents a channel for energy transfer between the two systems, which is essential for intrinsic magnetic damping.

2.1.2 The Energy Functional of a Magnet

The total internal magnetic field $\boldsymbol{H}_{\mathrm{eff}}$ acting on the magnetic moments inside a solid results from the functional derivative of the total energy density $\varepsilon_{\mathrm{tot}} = E_{\mathrm{tot}}/V$ with respect to the reduced magnetization $\boldsymbol{m}(\boldsymbol{r}) = \boldsymbol{M}(\boldsymbol{r})/M_{\mathrm{s}}$

$$\boldsymbol{H}_{\mathrm{eff}} = -\frac{1}{\mu_0} \frac{\delta \varepsilon_{\mathrm{tot}}}{\delta \boldsymbol{m}}, \tag{2.8}$$

where V is the sample volume. The free energy density of a magnetic system is given by

$$\varepsilon_{\mathrm{tot}} = \varepsilon_{\mathrm{zee}} + \varepsilon_{\mathrm{ani}} + \varepsilon_{\mathrm{dem}} + \varepsilon_{\mathrm{ex}}, \tag{2.9}$$

where ε_{zee} represents the Zeeman, ε_{ani} the anisotropy, ε_{dem} the demagnetizing, and ε_{ex} the exchange energy density. The various contributions are briefly discussed in the following.

- **Zeeman Energy**

  The Zeeman term arises from interaction of the magnetization $\boldsymbol{M}$ with an external field $\boldsymbol{H}_0$

  $$\varepsilon_{\text{zee}} = \frac{1}{V} \int \mathrm{d}V \, \boldsymbol{M} \cdot \boldsymbol{H}_0, \tag{2.10}$$

  It favors parallel alignment of the magnetization along the external field direction.

- **Anisotropy Energy**

  In magnetic crystals the total energy is usually dependent on the orientation of the magnetization with respect to preferential directions inside the crystal. The exchange energy only depends on the angle between neighboring spin moments but not on the orientation regarding the crystallographic axes. However, as already mentioned in conjunction with spin-orbit interaction, the lattice potential leads to nonuniform spatial distribution of the electronic wave functions. As a consequence, the orientation of the orbital magnetic moments is determined by the local ordering of the atoms. By virtue of spin-orbit interaction, the electron spin moments in turn also orient towards these distinct directions.
  Magnetic anisotropy arising from crystalline symmetries is referred to as magnetocrystalline anisotropy. In cubic systems the energy density due to crystal anisotropy reads

  $$\varepsilon_{\text{ani}} \;=\; K_1(\alpha_x^2\alpha_y^2 + \alpha_y^2\alpha_z^2 + \alpha_z^2\alpha_x^2) + K_2\alpha_x^2\alpha_y^2\alpha_z^2, \tag{2.11}$$

  where α_{i} are the directional cosines of the normalized magnetization $\boldsymbol{m}$ with respect to the cartesian axes of the lattice. K_1 and K_2 are the crystalline anisotropy constants of first and second order, respectively. In addition to the intrinsic ordering arising from the crystal lattice, atomic ordering may also be caused by surfaces and interfaces and hence is of particular importance in confined magnetic systems. For crystals exhibiting uniaxial anisotropy, the energy density is

  $$\varepsilon_{\text{ani}} \;=\; K_U\alpha_x^2, \tag{2.12}$$

  with the uniaxial anisotropy constant K_U.

- **Demagnetizing Energy**

  When a magnetic sample has a net magnetization $\boldsymbol{M}$, due to exchange interaction the magnetic moments inside the sample always find neighboring moments oriented parallel. Therefore, the magnetic stray field is effectively suppressed. However, on account of the sample's finite volume the magnetic moments inevitably meet the sample boundaries, where every magnetization component normal to the surface gives rise to uncompensated magnetic charges. The magnitude

of the surface charge density given by the divergence of $\boldsymbol{M}$ causes an opposite divergence of the demagnetizing field. Since $\nabla \cdot \boldsymbol{B}$ is zero, it is given by

$$\nabla \cdot \boldsymbol{H}_{\mathrm{dem}} = -\nabla \cdot \boldsymbol{M}. \tag{2.13}$$

This field points opposite to the internal field, and thus tends to demagnetize the magnetic sample. Consequently, it is called demagnetizing field. Applying equation 2.3 to a single dipole reveals a finite energy of the dipole due to its own magnetic stray field. For a magnetized sample this concept yields a stray field energy of

$$\varepsilon_{\mathrm{dem}} = -\frac{1}{2V}\int \mathrm{d}V\, \boldsymbol{H}_{\mathrm{dem}} \cdot \boldsymbol{M}. \tag{2.14}$$

The expression for the demagnetizing field of an arbitrarily shaped element generally constitutes a very complex function of position. It is, however, uniform in the case of an homogeneously magnetized ellipsoid and thus simplifies to

$$\mu_0 H_{\mathrm{dem}} = -\overleftrightarrow{N}\,\mu_0\,\boldsymbol{M}, \tag{2.15}$$

with the dimensionless demagnetizing tensor $\overleftrightarrow{N}$, which can be diagonalized if the magnetization points along a principle axis of the ellipsoid:

$$\overleftrightarrow{N} = \begin{pmatrix} N_x & 0 & 0 \\ 0 & N_y & 0 \\ 0 & 0 & N_z \end{pmatrix}. \tag{2.16}$$

The trace of $\overleftrightarrow{N}$ satisfies $N_x + N_y + N_z = 1$.
Note that a thin film as shown in Fig. 2.1 represents a good approximation of a flat ellipsoid. When the film is magnetized in-plane, the stray field can be neglected on account of infinitely separated boundaries (see Fig. 2.1(a)). In contrast, when the magnetization points out of the film plane, the magnetic monopoles at the surfaces give rise to a field of

$$\boldsymbol{H}_{\mathrm{dem}} = -\hat{z} M_{\mathrm{S}} \tag{2.17}$$

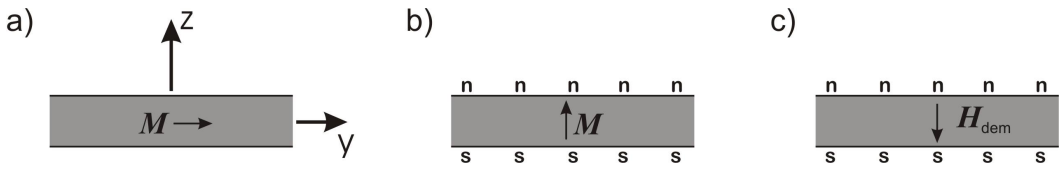

Figure 2.1: *A thin film magnetized parallel (a) and perpendicular ((b) and (c)) to its plane. Due to the large separation of the film boundaries in the parallel configuration (a) the monopoles at the film surfaces (left and right) induced by the magnetic field can be neglected. However, in the case of perpendicular magnetization, apparent magnetic monopoles at the up and down film surfaces generate a strong demagnetizing field* $\boldsymbol{H}_{\mathrm{dem}}$ *orientated opposite to the magnetization* $\boldsymbol{M}$ *(c).*

pointing opposite to the magnetization $\boldsymbol{M}$ (see Fig. 2.1(c)). Hence, the in-plane demagnetizing factors vanish ($N_x = N_y = 0$), whereas the perpendicular component is maximum ($N_z = 1$). As a consequence of energy minimization, the demagnetizing field tends to prevent the magnetic moments from aligning perpendicular to the sample surface. As shown in Chapters 5 and 6, the minimization of the effective demagnetizing field may lead to flux-closure configurations in the case of laterally confined in-plane magnetized elements.

- **Exchange Energy**

  The exchange term has already been discussed above (see Eq. 2.5). The corresponding energy density reads

$$\varepsilon_{\mathrm{ex}} = \frac{A}{V} \int \mathrm{d}V (\nabla \boldsymbol{m})^2. \tag{2.18}$$

2.2 Dynamic Magnetism

The crucial difference of magnetization dynamics compared to static phenomena (usually in the millisecond time range) is the time scale on which the magnetic system is disturbed by an external stimulus and of course on which time scale one in turn observes its response. When applying quasi static fields to a magnetic system, the magnetization appears to be always in equilibrium since the dynamic processes happen on the nanosecond timescale or faster. In contrast, when applying alternating magnetic fields with a frequency equal to the resonance frequency of the system, the magnetization configuration is resonantly disturbed from its equilibrium position. The underlying physical concepts and the theoretical description of the dynamic response of the magnetization are illustrated in this section.

2.2.1 Equation of Motion

The effect of applying an external magnetic field $\boldsymbol{H}_0$ to a single atom is to lift the degeneracy of the electronic states with respect to the orbital and spin magnetic quantum numbers. This splitting known as the Zeeman effect is given by:

$$\Delta E_{ik} = g\,\mu_{\mathrm{B}}\,\Delta m_{ik}\,\mu_0(1+\overleftrightarrow{\chi})\,\boldsymbol{H}_0, \tag{2.19}$$

with Δm_{ik} being the difference of the magnetic quantum numbers of the states i and k, and $\overleftrightarrow{\chi}$ being the susceptibility. Due to rigid selection rules the only allowed transitions are $\Delta m_{ik} = \pm 1$. These transitions can be induced by an alternating magnetic field $\boldsymbol{h}$ with appropriate frequency. In practice, instead of dealing with a single isolated atom, the magnetic system usually consists of a large number of atoms, with a large number of electrons interacting by virtue of exchange coupling. Thus, one can merge from the individual states of the single atom with magnetic moment $\boldsymbol{m}$ to the quasi continuous

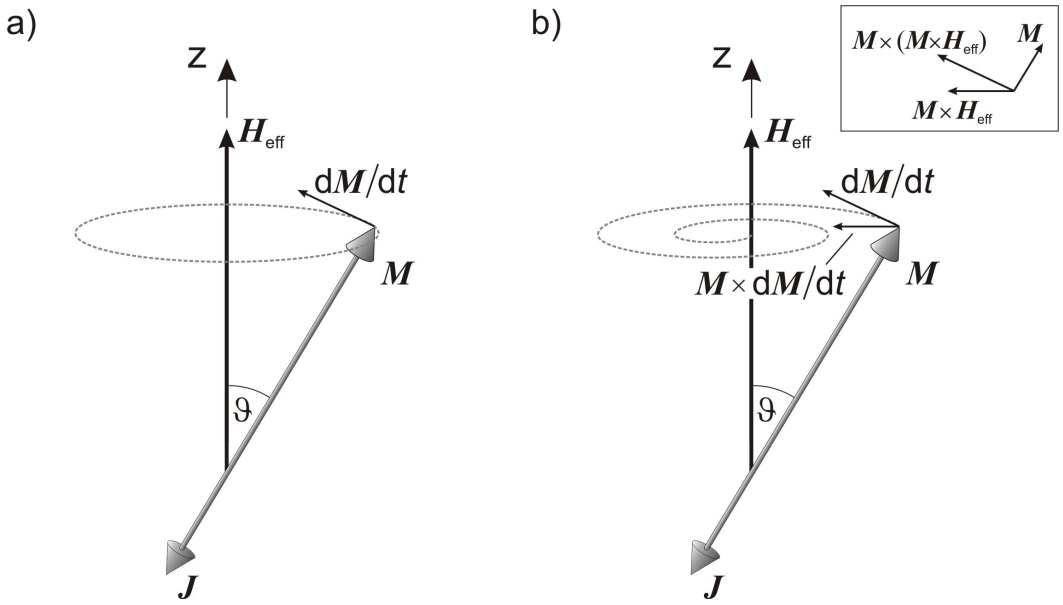

Figure 2.2: *When disturbing the equilibrium configuration, the magnetic moment* $\boldsymbol{M}$ *associated with the total angular momentum* $\boldsymbol{J}$ *precesses around the effective magnetic field* $\boldsymbol{H}_{\text{eff}}$ *(a). The torque acting on the moment is given by Eq. 2.20. When introducing damping, the magnetization follows a helical trajectory back to its equilibrium position (b), described by Eq. 2.22. The inset in (b) shows the coordinate system spanned by the three orthogonal vectors.*

treatment in a macroscopic description with magnetization $\boldsymbol{M} = n\,\boldsymbol{m}$, where n is the number of microscopic magnetic moments per unit volume [38]. Consequently, the magnetization within the unit volume can be dealt with in a macrospin description. As already shown in Subsection 2.1.2, the total magnetic field acting on the magnetic moments inside a solid contains not only the external Zeeman field $\boldsymbol{H}_0$ but also local exchange, local anisotropy, and dipolar fields. The various contributions to the magnetic field are accounted for by introducing the effective field $\boldsymbol{H}_{\text{eff}}$.
When the equilibrium configuration is disturbed, the magnetization is at an angle $\vartheta \neq 0$ regarding the magnetic field $\boldsymbol{H}_{\text{eff}}$. By virtue of energy minimization, the magnetization tends to align parallel to the field. However, as shown in Chapter 2.1, a magnetic moment is inevitably associated with a total angular momentum $\boldsymbol{J}$[1], so that a torque is exerted on the magnetization. Since torque corresponds to a rate of change of the angular momentum, the magnetization starts to precess around the static field $\boldsymbol{H}_{\text{eff}}$, as shown in Fig. 2.2(a). This precession is described by the classical equation of motion

$$\frac{\mathrm{d}\,\boldsymbol{M}}{\mathrm{d}t} = -\gamma\mu_0\,\boldsymbol{M} \times \boldsymbol{H}_{\text{eff}}, \tag{2.20}$$

where $\gamma = g\,|e|/(2m_e)$ is the gyromagnetic ratio. Note that due to the negative sign of the electron charge, the precessional sense is opposite for the magnetic and the

[1]The angular and spin moments generally are couple, so that the total angular momentum needs to be introduced

angular moment, namely counterclockwise and clockwise, respectively. According to equation 2.20 the magnetic moment precesses around the static field at a constant cone angle ϑ without reaching the equilibrium position. This, however, contradicts the experimental observation, which shows that the magnetic moment reaches equilibrium after a finite time. To account for this finding, an additional component has to be added to the precessional term which points toward the effective field. The trajectory of the magnetic tip can be described by means of a system of three orthogonal vectors. However, when assuming the length of $\boldsymbol{M}$ to be preserved, a linear combination of the two orthogonal vectors $[\boldsymbol{M} \times \boldsymbol{H}_{eff}]$ and $[\boldsymbol{M} \times (\boldsymbol{M} \times \boldsymbol{H}_{eff})]$ is sufficient to describe the corresponding motion (see inset in Fig. 2.2(b)). By employing this concept, in 1935, Landau and Lifshitz [39] formulated the equation of motion including damping:

$$\frac{\mathrm{d}\,\boldsymbol{M}}{\mathrm{d}t} = -\gamma\,\mu_0\,\boldsymbol{M} \times \boldsymbol{H}_{\mathrm{eff}} - \frac{\lambda}{M_{\mathrm{S}}^2}\,\boldsymbol{M} \times (\boldsymbol{M} \times \boldsymbol{H}_{\mathrm{eff}}). \tag{2.21}$$

As pre-factor for the damping term, they introduced the phenomenological damping constant $\lambda = 1/\tau$ which corresponds to the inverse relaxation time τ. This expression is referred to as the Landau-Lifshitz (LL) equation. Since this approach causes very fast precession in the case of very large damping, it generally does not describe the behavior correctly in the large damping regime. In 1955, Gilbert [40] circumvented this problem by introducing a viscous damping term to the torque equation 2.20

$$\frac{\mathrm{d}\,\boldsymbol{M}}{\mathrm{d}t} = \underbrace{-\gamma\,\mu_0\,\boldsymbol{M} \times \boldsymbol{H}_{\mathrm{eff}}}_{\text{precessional term}} + \underbrace{\frac{\alpha}{M_{\mathrm{S}}}\left(\boldsymbol{M} \times \frac{\mathrm{d}\,\boldsymbol{M}}{\mathrm{d}t}\right)}_{\text{damping term}}, \tag{2.22}$$

with α being the phenomenological and dimensionless damping parameter. This attempt is referred to as the Landau-Lifshitz-Gilbert (LLG) equation. Eqs. 2.21 and 2.22 consist of a precessional and a damping term. As a result of the damping term, the motion of the magnetization follows a helical trajectory as shown in Fig. 2.2(b). Note that in the case of small damping, the LL and the LLG equation are equivalent.
Regarding the damping parameter the term phenomenological already implies that the microscopic origin of the magnetic damping is still not completely understood in detail and constitutes a very active area of research. Possible relaxation mechanisms can be divided into intrinsic and extrinsic processes. Unavoidable processes, like direct coupling of the magnons to the lattice via spin-orbit interaction and eddy currents mediated by free electrons present in conducting materials are refereed to as intrinsic processes. Scattering processes due to sample imperfections leading to magnon-magnon scattering [41–44] are extrinsic contributions to damping. An experimental access to purely intrinsic damping is given by conventional FMR, as described in Subsection 3.1.1. However, in general, nonuniform excitation and a small bias field range prevent the separation of extrinsic and intrinsic contributions to damping. The mixture of the two contributions are accounted for in this work by introducing an effective damping constant α^*.

2.2.2 The Dynamic Susceptibility

In this subsection the solution of the LLG equation is sketched exemplarily for the case of a weak alternating high frequency (hf) magnetic field $\boldsymbol{h}$. Both the hf field and the magnetization configuration of the excited ferromagnetic sample are assumed to be uniform. Thus, in the following also the precession of the magnetization can be considered to be uniform throughout the whole magnetic sample. The crystal anisotropy of the sample is assumed to have an easy axis along the x-direction. Other contributions to anisotropy are neglected for simplicity. In addition the static external field and therefore also the magnetization point along the x-direction. When assuming a weak exciting field $\boldsymbol{h}$, only small precessional cone angles are excited. In this case the magnetization vector can be separated into constant and time dependent components. Since the exciting field points along the y-direction, the precession is limited to the y-z-plane. Let the demagnetizing tensor be diagonal, so that the demagnetizing field can be written as

$$\mu_0 \boldsymbol{H}_{\mathrm{dem}} = -\mu_0 N_x M_s \,\hat{x} - \mu_0 N_y m_y \,\hat{y} - \mu_0 N_z m_z \,\hat{z}, \tag{2.23}$$

where m_i are the high frequency alternating components of $\boldsymbol{M}$. Thus, the effective field and the magnetization are given by

$$\boldsymbol{H}_{\mathrm{eff}} \;=\; (H_0 \,+ H_{\mathrm{ani}} - N_x M_{\mathrm{S}})\hat{x} + (h - N_y m_y)\,\hat{y} - N_z m_z \,\hat{z} \tag{2.24}$$

and

$$\boldsymbol{M} \;=\; M_{\mathrm{s}}\,\hat{x} + m_y\,\hat{y} + m_z\,\hat{z}, \tag{2.25}$$

respectively. Substituting 2.24 and 2.25 into the LLG equation 2.22 yields

$$\begin{aligned}
0 &= -\gamma\,\mu_0\,(-m_y\,N_z m_z - \,m_z\,(h - N_y m_y)) + \frac{\alpha}{M_{\mathrm{s}}}\left(m_y\,\frac{\mathrm{d}m_z}{\mathrm{d}t} - m_z\,\frac{\mathrm{d}m_y}{\mathrm{d}t}\right)\\
\frac{\mathrm{d}m_y}{\mathrm{d}t} &= -\gamma\,\mu_0\,(m_z\,(H_0 + H_{\mathrm{ani}} - N_x M_{\mathrm{S}}) - M_{\mathrm{S}}\,N_z m_z) - \alpha\,\frac{\mathrm{d}m_z}{\mathrm{d}t}\\
\frac{\mathrm{d}m_z}{\mathrm{d}t} &= -\gamma\,\mu_0\,\left(M_{\mathrm{S}}\,(h - N_y m_y) - m_y\,(H_0 + H_{\mathrm{ani}} - N_x M_{\mathrm{S}})\right) + \alpha\,\frac{\mathrm{d}m_y}{\mathrm{d}t}.
\end{aligned}$$

Because for small angles of precession $h \ll H$ and $m_i \ll M_s$, only terms which are linear in h and m are considered. When introducing the time dependence of $m \propto e^{-i\omega t}$, the relevant resulting equations read

$$0 \;=\; -i\,\omega\,m_y \,+ (\omega_H + (N_z - N_x)\omega_M - i\,\alpha\,\omega)\;m_z \tag{2.26}$$

$$\omega_M\,h \;=\; i\,\omega\,m_z + (\omega_H + (N_y - N_x)\omega_M - i\,\alpha\,\omega)\;m_y, \tag{2.27}$$

where the following convenient abbreviations have been used

$$\omega_M \;=\; \gamma\,\mu_0\,M_{\mathrm{S}} \tag{2.28}$$

$$\omega_H \;=\; \gamma\,\mu_0\,(H_0 + H_{\mathrm{ani}}). \tag{2.29}$$

From Eqs. 2.26 and 2.27 one finally obtains an equation for $\boldsymbol{h}$ related to $\boldsymbol{m}$

$$\begin{pmatrix} 0 \\ h \end{pmatrix} \omega_M = \begin{bmatrix} -i\omega & \omega_H + (N_z - N_x)\omega_M - i\alpha\omega \\ \omega_H + (N_y - N_x)\omega_M - i\alpha\omega & i\omega \end{bmatrix} \begin{pmatrix} m_y \\ m_z \end{pmatrix}. \tag{2.30}$$

The damping constant is usually small, so that only linear terms in α are considered and $1 + \alpha \sim 1$ is used. Since $\boldsymbol{m} = \overleftrightarrow{\chi}\ \boldsymbol{h}$, some algebraic transformations yield the real and imaginary parts of the susceptibility as a function of the angular frequency of the exciting field ω

$$\chi'_{yy} = \frac{\omega_M(\omega_H + (N_z - N_x)\omega_M)(\omega_r^2 - \omega^2)}{[\omega_r^2 - \omega^2]^2 + \alpha^2\omega^2[2\omega_H + (N_y + N_z - 2N_x)\omega_M]^2} \tag{2.31}$$

$$\chi''_{yy} = \frac{\alpha\omega\omega_M[(\omega_r^2 - \omega^2) + (\omega_H + (N_z - N_x)\omega_M)(2\omega_H + (N_y + N_z - 2N_x)\omega_M)]}{[\omega_r^2 - \omega^2]^2 + \alpha^2\omega^2[2\omega_H + (N_y + N_z - 2N_x)\omega_M]^2}. \tag{2.32}$$

While the imaginary part of the hf susceptibility represents the precessional amplitude and has a Lorentzian shape with a maximum at the resonance frequency ω_r, the real part represents the dispersion and is antisymmetric with respect to ω_r (see Fig. 2.3). For small damping the resonance condition of the ferromagnetic sample is given by

$$\omega_r^2 = [\omega_H + (N_z - N_x)\omega_M][\omega_H + (N_y - N_x)\omega_M]. \tag{2.33}$$

This expression is referred to as the Kittel equation [45]. The frequency linewidth $\Delta\omega$ of the susceptibility is defined as the Half Width at Half Maximum (HWHM) of the

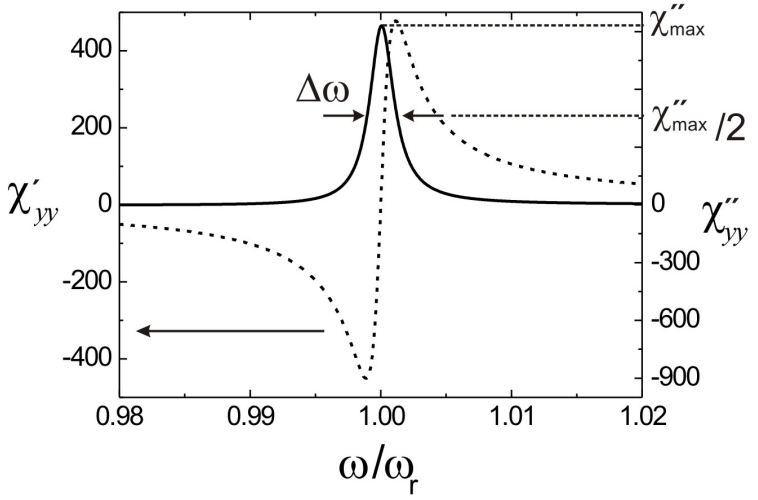

Figure 2.3: *The real (dashed line) and the imaginary (solid line) part of the complex hf susceptibility of an ellipsoid ($N_x = N_y = N_z = 1/3$) plotted for a damping constant of $\alpha = 0.008$.*

imaginary part (see Fig. 2.3) and is directly related to the damping constant by the relation

$$\alpha = 2\Delta\omega / \left[2\omega_H + (N_z + N_y - 2N_x)\omega_M\right]. \tag{2.34}$$

This relation is valid for frequency swept techniques, e.g. in a vector network analyzer ferromagnetic resonance experiment, discussed in Subsection 3.1.2. If one keeps the exciting frequency constant and sweeps the applied magnetic field as employed in conventional ferromagnetic resonance (see Subs. 3.1.1), the HWHM field linewidth ΔH is related to α by

$$\alpha = \gamma\mu_0\Delta H/\omega_r. \tag{2.35}$$

Note that the derivation of the hf susceptibility shown in this subsection is only valid for uniform magnetization configuration and consequently uniform precession of the magnetization. In general, the derivation of the hf susceptibility constitutes a complex problem, so that an analytical expression can be found only for simple cases like a uniformly magnetized film.

2.2.3 Spin Waves

So far, magnetization dynamics was discussed in the limit of uniform precession of the magnetization throughout the sample volume. The so-called uniform mode implies that all magnetic moments precess at the same frequency and phase. However, higher order excitations may cause the magnetic moments to precess with the same frequency but at different phases and are referred to as spin waves. Since the exchange interaction is short ranged compared to dipolar interaction (cf. Subs. 2.1.1), spin waves can be classified depending on their wavelength into dipole or exchange dominated. In the long wavelength regime, spin waves are dipole dominated and referred to as *magnetostatic*. In contrast, for small wave lengths the spin wave properties are dominated by exchange interaction. In this case one refers to as simply *spin waves*. This subsection presents a general description of the spin waves observed within this research project.

Magnetostatic Spin Waves:

Approaching from long wavelengths the contributions of dipole-dipole interaction is discussed first. Maxwell's equations in the magnetostatic approximation read

$$\nabla \times \boldsymbol{H} = 0, \tag{2.36}$$

$$\nabla \cdot \boldsymbol{B} = 0. \tag{2.37}$$

By using the definition of the magnetic induction

$$\boldsymbol{B} = \mu_0(1 + \overleftrightarrow{\chi})\,\boldsymbol{H}, \tag{2.38}$$

with $\overleftrightarrow{\chi}$ being the hf susceptibility derived in the previous subsection, one arrives at a wave equation for the spatial part of the magnetostatic scalar potential Ψ

$$(1+\chi)\left[\frac{\partial^2\Psi}{\partial x^2}+\frac{\partial^2\Psi}{\partial y^2}\right]+\frac{\partial^2\Psi}{\partial z^2}\;=\;0, \tag{2.39}$$

where the exciting field is given by $\boldsymbol{h}=\nabla\Psi$. This equation is known as the Walker equation [46] and describes magnetostatic modes in homogeneous media. A detailed derivation of Eq. 2.39 can be found in [47]. For $\chi=-1$ the solution corresponds to the uniform precession with frequency ω_r given by Eq. 2.33. The solutions for $\chi\neq-1$ are found to be propagating magnetostatic spin waves. Different geometries are accounted for by means of properly chosen boundary conditions.
Both, the propagation properties and the amplitude distribution of the spin waves depend on the geometry of their propagation direction with respect to the static magnetization and the film plane. All the observed modes are dominated by the in-plane magnetization of the samples[2]. Additionally, only spin waves propagating in the sample plane were found. Therefore, the discussion is limited to the two possible geometries shown in Figure 2.4(right).
The dispersion relations shown in Fig. 2.4 reveal the different characters of the spin waves arising from dipole interaction. Dependent on the relative orientation between the magnetization $\boldsymbol{M}$ and the in-plane wave vector $\boldsymbol{k}_\parallel$, the group ($\nu_g=\partial\omega/\partial k$) and phase ($\nu_p=\omega/k$) velocities have equal or opposite signs. As a result the magnetostatic spin waves show positive and negative dispersion. These two modes are referred to as *surface* and *backward volume* waves:

- **Magnetostatic Surface Waves (MSSW)**:
  The static magnetization $\boldsymbol{M}$ and the in-plane wave vector $\boldsymbol{k}_\parallel$ enclose an angle of $\varphi_{k_\parallel}=90°$. The corresponding dispersion relation reads [47]

  $$\omega^2_{\mathrm{MSSW}}:=\omega_H(\omega_H+\omega_M)+\frac{\omega_M^2}{4}(1-e^{-2k_\parallel t}). \tag{2.40}$$

  At $k_\parallel=0$, its frequency corresponds to ω_r given by Eq. 2.33. It is worth noting that the amplitude of this mode is highest in the vicinity of the top and bottom surface of the sample and decays exponentially inwards. The modes located at the two surfaces propagate in opposite directions. This type of spin wave mode, with positive dispersion as shown in Fig. 2.4 (dipole dominated) was first found by Damon and Eshbach [48] and thus is often referred to as Damon Eshbach (DE) mode.

- **Magnetostatic Backward Volume Waves (MSBVW)**:
  In this case the in-plane wave vector and the magnetization are collinear. An approximation of the dispersion relation derived by Kalinikos and Slavin [49] is given by

  $$\omega^2_{\mathrm{MSBVW}}:=\omega_H\left[\omega_H+\omega_M\left(\frac{1-e^{-k_\parallel t}}{k_\parallel t}\right)\right]. \tag{2.41}$$

[2]The out-of-plane component in the case of the vortex configuration (cf. Chapter 5) mainly acts as a perturbation of the normal modes. The characteristic features of the modes, however, are still assigned by the in-plane magnetization.

Since group and phase velocity point in opposite directions, negative dispersion is observed (see dipole dipole dominated regime in Fig. 2.4). As a consequence, they are referred to as magnetostatic *backward volume* waves. The amplitude of these spin wave modes is distributed throughout the whole thickness of the sample. At $k_{\parallel} = 0$ its frequency corresponds to ω_r (Eq. 2.33) and thus is degenerate to the magnetostatic surface wave.

The origin of the different frequency behavior of the Damon Eshbach and the backward volume modes is illustrated in Fig. 2.5. In the case of MSBVW the wave vector $\boldsymbol{k}_{\parallel}$ lies parallel to the static magnetization $\boldsymbol{M}$. The dynamic magnetization $\boldsymbol{m}$ points perpendicular to the film surface (z-direction), which causes a dynamic stray field $h_{\mathrm{hf}}^{\mathrm{stray}}$. As $\boldsymbol{m}$ reverses its direction after a distance of $\lambda/2$, the energy associated with the stray field depends on the wavelength of the magnetostatic mode. Therefore, when increasing $\boldsymbol{k}_{\parallel}$ the antiparallel moments approach each other and the stray field energy decreases. Indeed, the energy and therefore the frequency of the backward volume modes decreases with increasing wave vector.
For the Damon Eshbach spin wave mode the situation differs in terms of the orientation of $\boldsymbol{k}_{\parallel}$ with respect to $\boldsymbol{M}$. Here the wave vector points perpendicular to the static magnetization. Although, on account of the out-of-plane dynamic magnetization

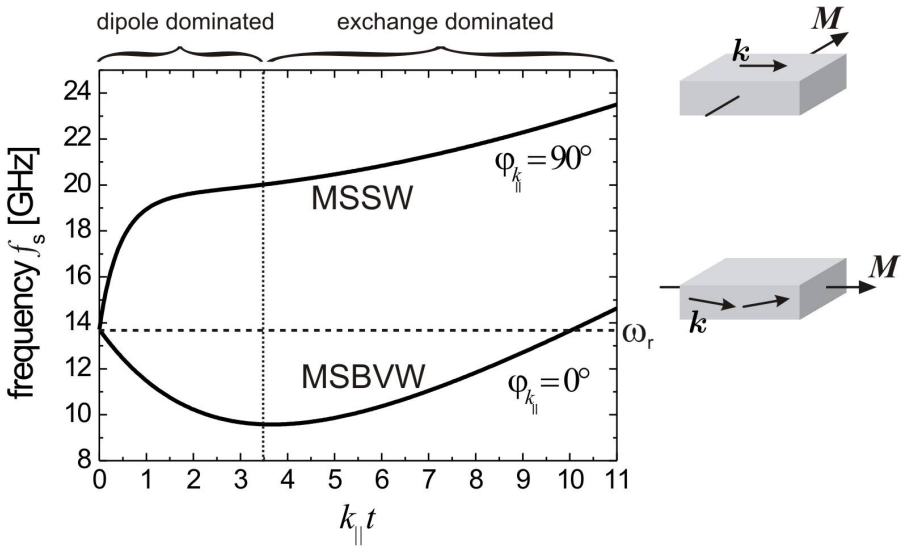

Figure 2.4: *The dispersion relations of spin wave modes as a function of the in-plane wave vector $k_{\parallel}$ times the film thickness t for two possible geometries. As illustrated by the images, the wave vectors are aligned parallel and perpendicular to the static magnetization in the case of backward volume and surface waves, respectively. At $k_{\parallel} = 0$ the two modes are found at the same frequency ω_{r} (cf. Eq. 2.33). While for small wave vectors the spin waves are dominated by dipolar interaction, the contribution from exchange interaction becomes dominant for large $k_{\parallel}$. The curves were calculated for $\mu_0 H_0 = 200\ mT$, $\mu_0 M_{\mathrm{S}} = 1$ T, $g = 2$, $A = 2 \times 10^{-11}$J/m, $t = 150$ nm.*

component the stray field energy still decreases with increasing in-plane wave vector, a second mechanism is dominant for the frequency behavior of the DE modes. After a distance $\lambda/2$, antiparallel moments $\boldsymbol{m}$ can be found pointing towards each other as shown in Fig. 2.5(b). When decreasing the wavelength the antiparallel moments approach each other and their mutual dipolar fields increases the wave energy. Thus the frequency raises with increasing $\boldsymbol{k}_{\parallel}$ as found in Fig. 2.4.

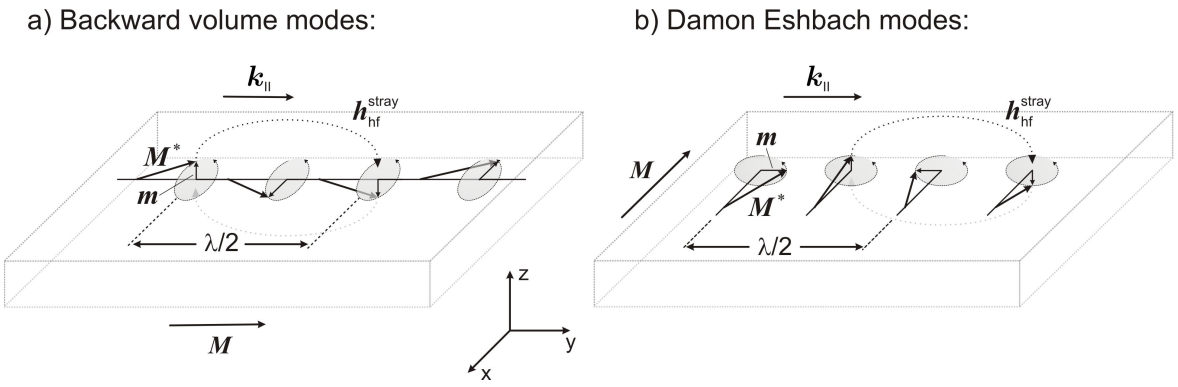

Figure 2.5: *The microscopic origin of the different frequency behavior of the backward volume (a) and the Damon Eshbach (b) magnetostatic modes.* $\boldsymbol{M}^*$ *denotes the combination of the static and dynamic magnetization* $\boldsymbol{M}$ *and* $\boldsymbol{m}$*, respectively. The dynamic stray field* $\boldsymbol{h}_{\mathrm{hf}}^{\mathrm{stray}}$ *of the magnetization along the z-component is indicated by the dotted lines. [50]*

Exchange dominated Spin Waves:

When increasing the wave vector, neighboring moments start to deviate from parallel alignment and as a consequence exchange interaction (cf. Eq. 2.4) needs to be taken into account. Exchange interaction becomes dominant when the spin wave length is of the order of the exchange length which is given by

$$l_{ex} = \frac{\sqrt{2A\,\mu_0}}{M_{\mathrm{S}}}, \tag{2.42}$$

with A being the exchange constant (see Eq. 2.5). Within the exchange length the dipole interaction is dominated by the exchange interaction. Arias and Mills [41] derived an expression for the contribution of the exchange energy to the spin wave dispersion

$$\omega_{\mathrm{ex}}^2 = \gamma(2\omega_H + \omega_M)\frac{2A}{M_{\mathrm{S}}}k_{\parallel}^2, \tag{2.43}$$

where $\omega_{H,M}$ are given by Eqs. 2.29 and 2.28. Note that the contribution arising from exchange does not depend on the orientation between $\boldsymbol{k}$ and $\boldsymbol{M}$ (see exchange dominated regime in Fig. 2.4).

Spin Wave Modes in confined magnetic Structures:

Up to now the general properties of spin waves in extended systems have been discussed. Indeed, when the dimensions of the magnetic system are reduced, the boundary conditions at the surfaces modify the spin wave spectrum. In small magnetic elements with dimensions of the order of the wavelength of the spin wave, modal patterns can arise due to the formation of standing spin waves.
A more illustrative picture to the phenomenon of resonant excitation can be given by mechanically vibrating systems. Here, it is well understood that due to reflections of acoustic waves at the physical boundaries of a resonant body, standing waves are generated and in turn form vibrational patterns. First experiments on this subject were carried out by E. Chladni already in the 18^{th} century [51]. By means of a violin bow he forced metallic plates to resonantly vibrate (see Fig. 2.6(a)). In order to visualize the vibrational pattern he sprinkled fine sand across the plate which accumulates at the positions which do not move (nodes). In doing so, the sand indicates nodal lines of the acoustic modes as shown in Figs. 2.6(a) and (b) for a square and a circular plate, respectively.
Similar patterns due to standing spin waves can be observed when exciting small magnetic elements by means of high frequency magnetic fields [21, 24, 53]. The physical boundaries of the element give rise to a 'potential well' for the magnetic excitations, which supports standing waves only when the wavelength satisfies $\lambda/2 = n\mathrm{w}$ (see Fig. 2.7), where the number of nodes n being an integer. The width w and depth of the well are defined by the lateral dimensions of the element and the energy density of the system (see Eq. 2.9), respectively. As discussed before, the energy as a function of the number of nodes depends on the character of the magnetostatic spin waves. As shown in Fig. 2.7(a) and (b) the energy raises for surface waves and decreases for backward volume waves with increasing node number. Concerning the orientation of the

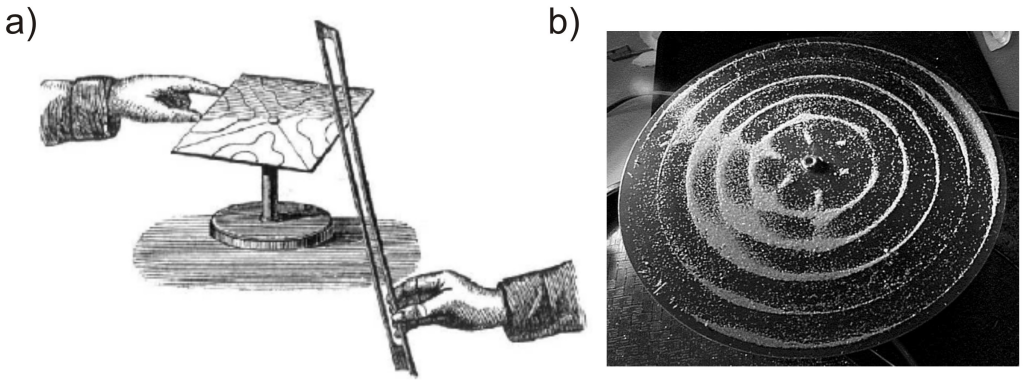

Figure 2.6: *The intriguing experiments of E. Chladni (a). Acoustic waves are excited in a square metallic plate by means of a violin bow. Fine sand visualizes the resulting standing waves by accumulating at the nodes of the mode pattern. The acoustic modal structure of a circular plate is depicted in (b) and shows clear, distinct radial nodes. Azimuthal nodes are indicated. [52].*

wave-vectors regarding the static magnetization, radial magnetic modes correspond to surface waves. Their number of nodes is labeled by n. Azimuthal magnetic modes, in contrast, correspond to backward volume waves. Their number of nodes is labelled by m. This convention shown in Fig. 2.7 was introduced by Buess et al. [21]. Note that for counting the number of nodes, each termination of the waves at the boundaries of the well is accounted for by a 1/2 node. According to this convention, for instance the number of nodes of the lowest mode shown in Fig. 2.7(a) is n = 1.
In general, micron sized elements favor the formation of dipolar dominated spin wave modes. However, on account of inhomogeneities of the internal fields, even in micron sized ferromagnetic elements exchange dominated excitations may be observed [13, 18]. In addition, when exciting higher order modes, the problem might be even more complicated for elements in the magnetostatic size regime. As shown in Fig. 2.4, when increasing the wave vector exchange interaction can no longer be ignored and the dynamic response gradually changes from purely magnetostatic to exchange dominated [54]. In this case also the boundary conditions for the magnetization change continuously from quasi-pinned (in case of dipole dominated) to unpinned (in case of exchange dominated) conditions [43, 45, 55–57].

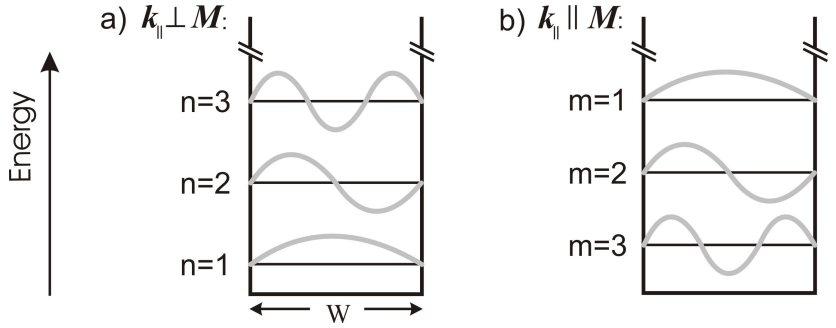

Figure 2.7: *Due to the confinement of the spin waves inside a 'potential well' with width* w *only modes with wavelength satisfying* $\lambda = n\mathrm{w}/2$ *are supported. While the energy of magnetostatic surface waves increases (a), it decreases for the magnetostatic backward volume waves (b), when rising the number of nodes. In the case of radial and azimuthal modes, the node numbers are labeled by n and m, respectively.*

3 Experimental Techniques and Introduction to Micromagnetics

The experimental setups which were employed in this research project to obtain the presented results are described in this chapter. In doing so emphasis is put on the two resonance techniques, namely the inductive network analyzer ferromagnetic resonance and the spatially resolved resonance Kerr microscopy. These two novel techniques were assembled as a part of this thesis and most of the presented results are obtained by these techniques. Furthermore, conventional ferromagnetic resonance, pulsed inductive microwave magnetometry, and time resolved Kerr microscopy which were also employed within this thesis are illustrated. Finally, since micromagnetic simulations are used to back up the experimental results, the concepts of micromagnetics are briefly introduced in the last part of the chapter.

3.1 Inductive Techniques

3.1.1 Conventional Ferromagnetic Resonance

One of the most established techniques to study spin waves in magnetic systems is conventional Ferromagnetic Resonance (FMR) [45, 58]. A magnetic system is exposed to a sinusoidal electromagnetic radiation at a fixed frequency typically in the microwave range. As shown in Section 2.2 the resonance frequency is determined by the effective field which includes the external field. Therefore, by sweeping a static external field the magnetic system can be driven through the ferromagnetic resonance by the external field. When measuring the absorption of the microwave radiation by the magnetic sample the resonance field is found at maximum absorption. In order to enhance the signal to noise ratio (SNR) the external magnetic field is modulated to allow for lock-in detection. As a consequence, the measured FMR signal is proportional to the field derivative of the imaginary part of the hf-susceptibility ($\partial\chi''/\partial H$). For details concerning the experimental realization of a FMR setup see B. Heinrich and J.A.C. Bland [58] or the dissertation of G. Woltersdorf [59].
Due to its high sensitivity conventional FMR is an excellent technique to study spin waves in magnetic bulk material and extended films exhibiting a single domain magnetization configuration. However, this technique is not applicable to investigate magnetic elements with a complex domain configuration, since sweeping an external field would alter the magnetization configuration and thereby the resonance condition during the measurement. This problem can be circumvented by sweeping the frequency instead of the external field which can be realized by using a vector network analyzer.

3.1.2 Vector Network Analyzer Ferromagnetic Resonance

In contrast to conventional FMR, this technique exploits the possibility to investigate the resonant dynamic response of a magnetic system by sweeping the frequency of the exciting hf field at a constant external field. This can be realized by connecting a Vector Network Analyzer (VNA) to a high bandwidth waveguide. In doing so, the VNA serves as the source as well as the detector of the sinusoidal high frequency (hf) signal. The VNA automatically sweeps the frequency of the outgoing signal across a specified range, which is maximum 45 MHz to 20 GHz for the employed model (Agilent PNA E8362A). As in the case of conventional FMR the signal excites the magnetization inside the sample. However, only near the resonance frequency of the system, energy is transferred from the incident wave to the sample. In addition, this signal is phase shifted by π at resonance, which causes destructive interference with the incident wave. These two effects in turn cause a decrease of the transmitted signal amplitude, which can be detected by the VNA. A detailed description of the VNA architecture can be found in Appendix A.1.
The VNA-FMR setup is shown in Fig. 3.1(a). The signal from the VNA is guided via microwave coaxial cables and air coplanar probes (Cascade Microtech Microprobes, 150 μm pitch and matched to 50 Ω) to a coplanar waveguide with the magnetic system placed on top of its signal line. In order to investigate the resonance behavior of the sample as a function of an externally applied magnetic field, the waveguide is mounted in the center of an electromagnet with four orthogonal poles (not shown) allowing the application of magnetic fields of up to 120 mT in any direction in the plane of the sample. Noise is prevented by mounting the setup onto an optical table with an air cushioning system.
Note that this setup also allows to measure the dynamic response by means of sweeping the external field at constant excitation frequency, just as for conventional FMR. In this case the network analyzer output is fixed to a single frequency, while driving the magnetic system through the resonance by sweeping the external field. This technique is advantageous only for some special cases e.g. magnetic systems with large damping and consequently large resonance linewidth.

3.1.3 Pulsed Inductive Microwave Magnetometry

A complementary approach to inductively measure the magnetization dynamics using a coplanar waveguide is to excite the spins by a short magnetic field pulse. For this purpose one side of the setup used for the VNA-FMR is connected to a pulse generator (picosecond pulse labs 10,060A), as shown in Fig. 3.1(b). If the rise or decay time of the pulse is short enough to trigger the precession of the magnetization, the inductive voltage reinduced into the waveguide can be detected by using a fast sampling oscilloscope (HP 54120A) connected to the second microprobe. In contrast to the two frequency domain techniques described in the beginning of this chapter, the so-called Pulsed Inductive Microwave Magnetometry (PIMM) yields the magnetic response as a function of time [60, 61]. For further details concerning the PIMM setup see the

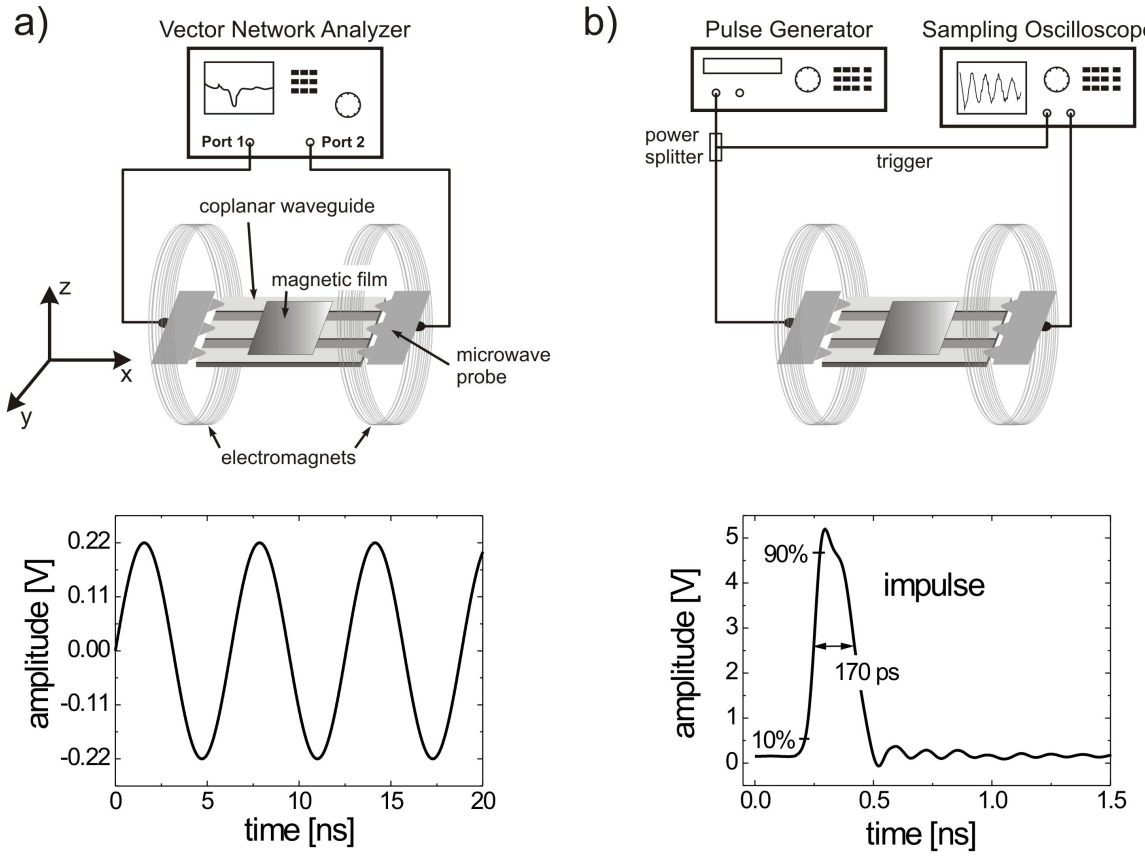

Figure 3.1: *The experimental setups for the VNA-FMR (a) and the PIMM (b) technique. The coplanar waveguide with the sample on top of the signal line is connected via air coplanar microwave probes. In (a) the VNA acts as the source and the detector of the continuous wave excitation. For the PIMM setup in (b) the magnetic pulses are generated by a pulse generator. The magnetic response is detected by the sampling oscilloscope. The graphs below show the continuous wave and impulse excitation employed for the VNA-FMR and the PIMM technique, respectively.*

dissertation of S. Ganzer [62]. The rise time of the applied pulses is less than 65 ps (10% - 90%) with a maximum amplitude of 10 V and a repetition rate of 100 kHz. For the measurements presented in Chapter 4, impulse excitation was employed with a pulse width of ~ 170 ps at half maximum (see bottom of Fig. 3.1(b)). Jitter from the internal trigger of the pulse generator is avoided by triggering the oscilloscope with a portion of the pulse separated by using a power splitter. The oscillation of the magnetization is recorded after switching off the pulse.

In order to increase the SNR both for the VNA-FMR and PIMM techniques, reference data is taken. For the reference data two different measurement schemes are employed. First, by applying an in-plane magnetic field $\boldsymbol{H}_{\mathrm{ref}}$ perpendicular to the waveguide the magnetization is pinned parallel to the excitation field $\boldsymbol{h}_{\parallel}$. As a consequence, the torque in Eq. 2.22 vanishes and the precession of the magnetization is

suppressed. Alternatively the reference field is applied along the waveguide. Hence, the resonance frequency is shifted to high frequencies. Subsequently, this reference spectrum is subtracted from the measurement at the corresponding bias fields $\boldsymbol{H}_0$ to remove the background. Both the VNA-FMR and the PIMM setup were automated by means of a computer control unit.
A detailed sketch of the coplanar waveguide is shown in Figure 3.2. The magnetic hf field generated by the waveguide can be assumed to be transverse near the center of the conductors and perpendicular in the vicinity of their edges (see Fig. 3.3). For a more thorough discussion of the coplanar waveguide including the hf field see Appendix A.2.

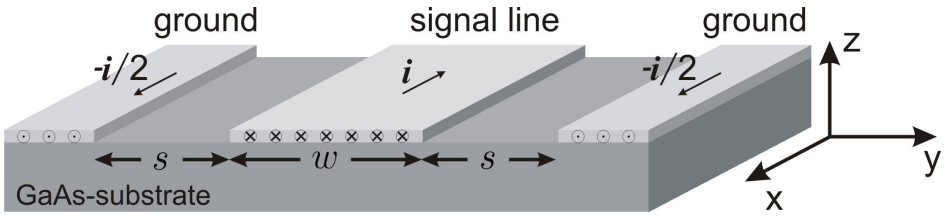

Figure 3.2: *The coplanar waveguide on GaAs substrate consists of a central signal line with width w carrying a current* $\boldsymbol{i}$*. At a distance s it is surrounded by two ground planes each carrying the current* $-\boldsymbol{i}/2$*.*

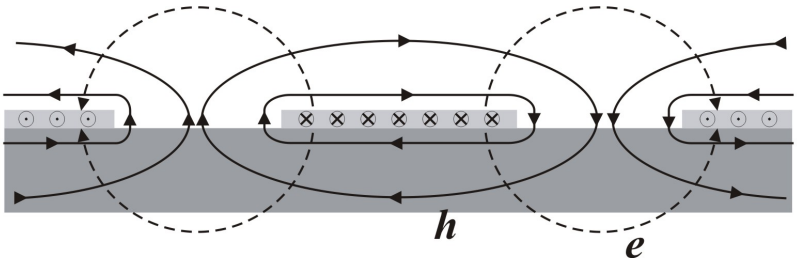

Figure 3.3: *The current travelling along the metallization of the waveguide generates a magnetic field* $\boldsymbol{h}$ *which is transverse in-plane at the center and perpendicular near the edges. In addition, an electric field* $\boldsymbol{e}$ *is created, which perpendicularly intersects the magnetic h-field lines.*

3.2 Optical Techniques

The term *optical* techniques arises from the employed detection scheme. Instead of inductively querying the dynamic response of the magnetization to an exciting hf field, the motion of the magnetic moments is locally probed by means of the Magneto-Optical Kerr Effect (MOKE).

3.2.1 The Magneto-Optical Kerr Effect

The magneto-optical Kerr effect was discovered by J. Kerr in 1877 [63, 64] and causes an incident linearly polarized light to rotate its polarization plane and become elliptically polarized upon reflection on a surface of a magnetic sample. In the classical picture the electric field $\boldsymbol{E}$ of the incident light forces the electrons inside the material to oscillate along the field direction. Due to the magnetic field generated by the magnetization $\boldsymbol{M}$ inside the material the electrons additionally experience a Lorentz force, which results in a small oscillatory component ν_{Lor} perpendicular to $\boldsymbol{M}$ and $\boldsymbol{E}$. This oscillation in turn radiates linear polarized light, which is superimposed on the reflected light. As a result the polarization of the reflected light is rotated slightly with respect to the incident beam. For materials with complex permittivity a phase lag of the generated light causes ellipticity of the reflected beam. Depending on the relative orientation of the light polarization to the magnetization and the surface plane, three different geometries for Kerr measurements can be distinguished (see Fig. 3.4):

- **Polar configuration:** The magnetization lies parallel to the surface normal. The rotation of the reflected light is maximum for perpendicular incidence ($\psi = 0$) and independent on the initial polarization direction.
- **Longitudinal (parallel) configuration:** The magnetization points along the plane of the incident light, parallel to the surface. Only for $\psi \neq 0$ the polarization of the reflected beam suffers rotation.
- **Transverse configuration:** The magnetization lies perpendicular to the plane of incidence and parallel to the sample surface. In case of parallel polarized light the transversal Kerr effect changes the intensity of the reflected beam.

The intrigued reader can find a more detailed description of the Kerr effect in [65].

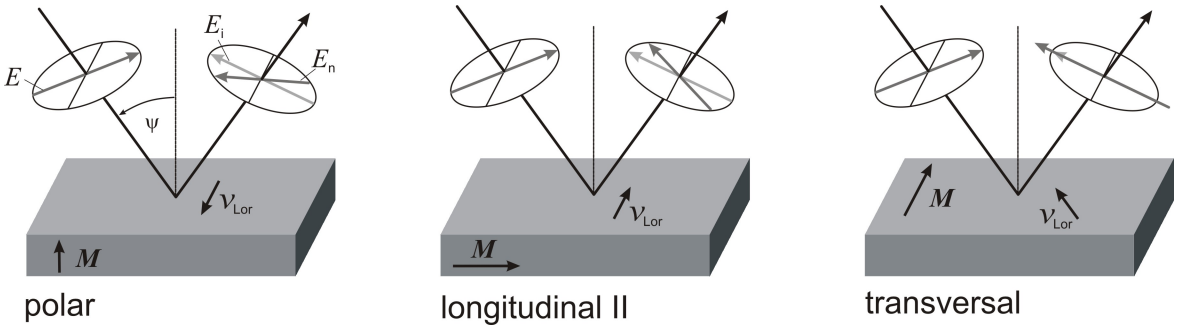

Figure 3.4: *Schematic sketch of the three different geometries for the magneto-optical Kerr effect. The magnetization is indicated by* $\boldsymbol{M}$*, the electric field of the incident beam is labeled by* $\boldsymbol{E}$*. Interaction with the electrons in the material causes an oscillatory motion* ν_{Lor} *induced by the Lorentz force. After being reflected, the new electric field amplitude of the light beam is labeled by* $\boldsymbol{E}_{\mathrm{n}}$*. The initial amplitude of the beam is denoted by* $\boldsymbol{E}_{\mathrm{i}}$*.*

3.2.2 Time Resolved Scanning Kerr Microscopy

This technique is based on the excitation of the magnetic sample using a short magnetic field pulse – such as used for the PIMM measurements (see Subs. 3.1.3) – and stroboscopically record the response of the magnetization by using a short optical pulse. The corresponding setup is shown in Fig. 3.5. A Ti:sapphire laser system provides optical pulses with a duration of ~ 150 fs and a wavelength of ~ 800 nm. Due to diffraction the spatial resolution is mainly limited by the wavelength λ of the light. Therefore, the initial laser beam is frequency doubled in order to enhance the spatial resolution which is given by [66]

$$r = 0.61\lambda/A, \tag{3.1}$$

where A is the numeric aperture of the objective lens. According to this equation, 200 nm maximum resolution can be achieved when using an oil immersed lens. For the purpose of frequency doubling the laser beam is focused onto a lithium borate (LiB_3O_5) crystal, which doubles the frequency of a fraction of the incident beam via second harmonic generation. The two components are separated behind the crystal by using a dichroic mirror. The 800 nm beam is guided via a variable optical delay line onto a fast photoconductive switch, which is connected to the waveguide with the magnetic sample. The metallic finger structure of the switch is fabricated onto GaAs substrate as shown in Fig. 3.5. When illuminating the photo switch, free carriers are created inside the GaAs substrate between the fingers. As a consequence, the switch becomes conductive, so that by virtue of the applied voltage a current pulse is launched into the waveguide. For details concerning the photoconductive switch refer to Gerrits et al. [67]. The current pulses travelling along the waveguide generate a magnetic field which in turn excites the magnetic system.
The frequency doubled part of the beam ($\lambda = 400$ nm) is focused onto the magnetic sample by means of a polarization conserving microscope (Zeiss Axiomat). After being reflected from the sample, the light is split by a Wollaston prism into two orthogonal linear polarization components. These components are detected separately using photodiodes. The difference between the two signals is sensitive to the Kerr rotation. Note that on account of a finite cone angle ϑ of the incident beam leads to a mixing of the various Kerr effect geometries described above (see Fig. 3.6). However, the detected Kerr signal is averaged over the whole beam diameter, so that contributions from opposite incident angles arising from longitudinal and transversal Kerr effect are mutually erased. Therefore, all optical measurements presented in this thesis are sensitive to the polar component of the dynamic magnetization.
Spatial resolution is achieved by laterally scanning the sample under the objective lens. In addition to the spatial resolution the optical delay allows one to record the dynamic response as a function of the delay time between the pump and the probe beam. This is the reason why this technique is referred to as Time Resolved Scanning Kerr Microscopy (TR-SKEM).
The signal to noise ratio is increased by using lock-in detection which is accomplished by gating the pump beam using an optical chopper. The chopper frequency serves as the reference for the phase sensitive detection scheme of the lock-in amplifier, which allows to extract the modulated dynamic response of the magnetic sample. Averaging

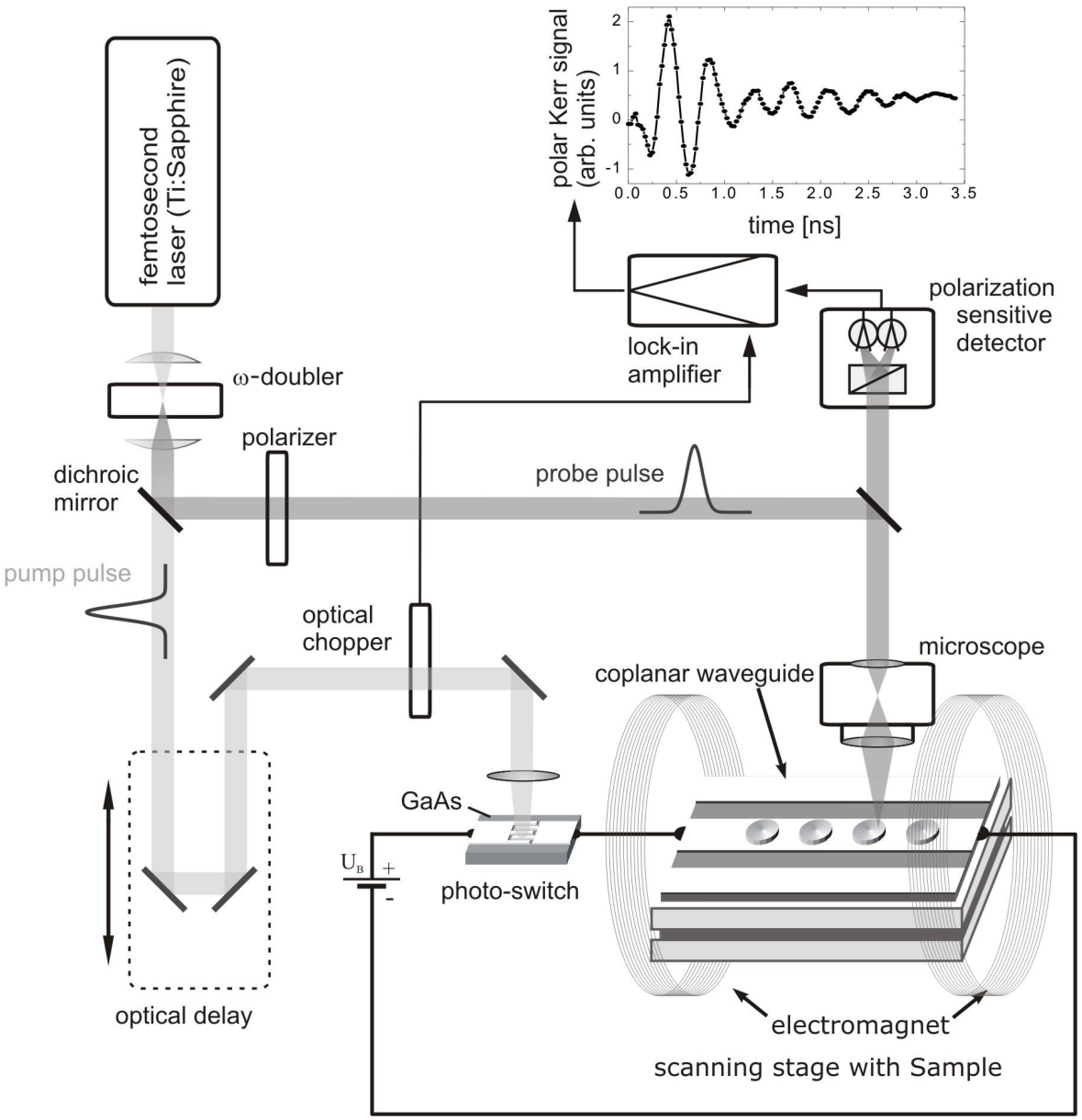

Figure 3.5: *The time resolved scanning Kerr microscopy (TR-SKEM) setup. The 800 nm (pump pulse) beam from the Ti:sapphire laser system is focused onto a photo switch in order to launch a magnetic pulse into the waveguide. By means of the magneto-optical Kerr effect in polar geometry, the magnetic response is probed by the frequency doubled laser beam (probe pulse) focused onto the magnetic sample. The optical delay allows to record the dynamic response as a function of the time delay between the pump and the probe pulses. The polarization of the reflected beam is detected using a Wollaston prism and two photodiodes. A scanning stage allows for spatial resolution by laterally scanning the magnetic sample. The red laser beam is chopped in order to enable lock-in detection.*

over many pulses further increases the SNR.
As described above the TR-SKEM technique yields the magnetization dynamics as a function of time and position on the sample. In order to find the frequencies of the different modes, global Fourier transformation (FT) of the averaged time domain data is performed. Additionally, in order to gain a deeper insight into the structure of the excited modes the time domain image sequence is transformed into the frequency domain by employing a phase-sensitive local Fourier transformation procedure [10, 68] described in Subsection 3.3.

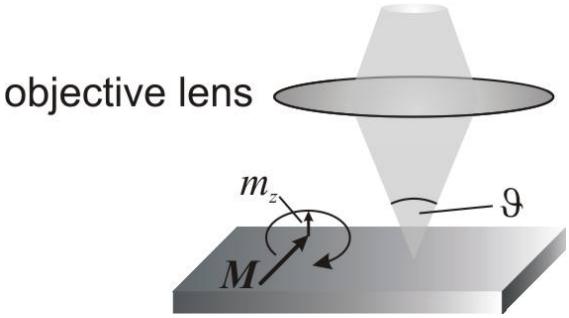

Figure 3.6: *Due to the cone angle ϑ of the incident beam which is determined by the objective lens, a part of the incoming beam deviates from perpendicular incidence. As a consequence, one detects a mixture of the polar, the longitudinal, and the transversal Kerr effect (see Fig. 3.4). However, by averaging over all directions, the longitudinal and transversal components are erased. Thus the setup is sensitive only to the polar component m_z.*

3.2.3 Ferromagnetic Resonance Scanning Kerr Microscopy

A more direct access to the modal structure of confined magnetic elements can be obtained by combining conventional TR-SKEM (described above) with continuous wave excitation [9, 69, 70]. This novel technique is referred to as Ferromagnetic Resonance Scanning Kerr Microscopy (FMR-SKEM). A sketch of the setup is shown in Fig. 3.7. In contrast to the previously discussed pulsed excitation [21, 68], which launches a complicated superposition of modes, now only a certain eigenmode of the magnetic system is selectively excited. This allows the direct imaging of the structure of a given mode with the high spatial resolution of the Kerr setup of maximum ~ 200 nm.
The cw hf excitation is generated by the vector network analyzer operated at a fixed frequency. In this case lock-in detection is realized by gating the excitation from the VNA using a fast p-i-n diode as microwave chopper. The conductivity of the intrinsic region of the pin diode is controlled by a square wave signal. Since again averaging over many pulses is needed a fixed correlation between the phase of the excitation and the probe beam has to be guaranteed. For this reason the Ti:sapphire oscillator and the VNA are locked to an external clock. The repetition rate of the laser is locked to 80 MHz by means of a piezo-mirror, which tunes the cavity to the required length. The VNA is synchronized to this clock at 80/8 MHz = 10 MHz (see Fig. 3.8). As a result the minimum step for sweeping the frequency is given by 80 MHz which corresponds

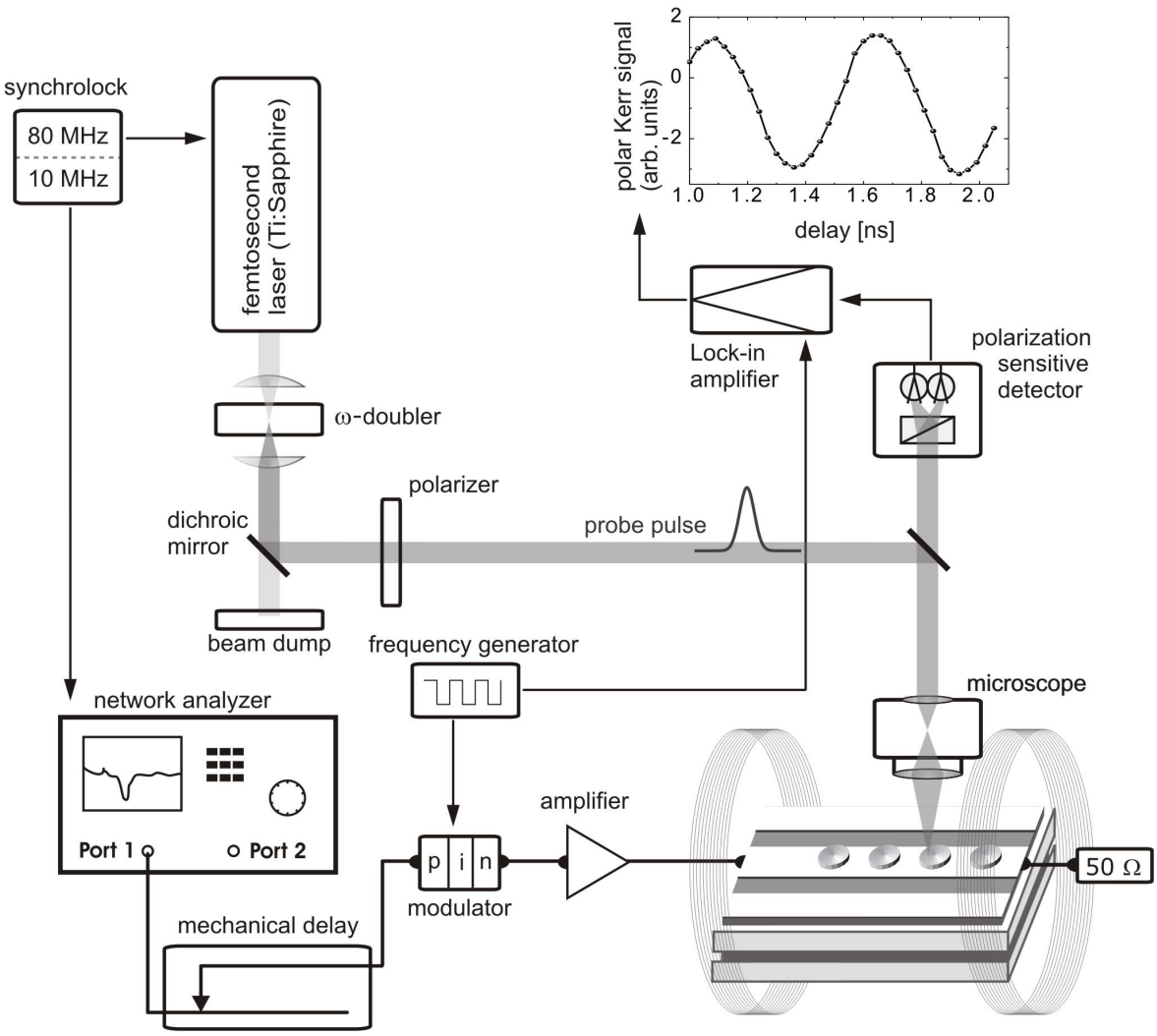

Figure 3.7: *The ferromagnetic resonance scanning Kerr microscopy (FMR-SKEM) setup. Since the network analyzer generates a sinusoidal high frequency signal to excite the sample, the 800 nm laser beam is not used for this technique. The frequency doubled beam (probe pulse) is focused onto the magnetic sample using a microscope. By means of the magneto-optical Kerr effect in polar geometry, the magnetic response is probed by the laser beam. The network analyzer allows to excite the magnetic sample in a frequency range from 45 MHz to 20 GHz. In addition, the mechanical delay enables one to investigate the dynamic response at any phase of the exciting cw signal. The polarization of the reflected beam is detected using a Wollaston prism and two photodiodes. In order to ensure fixed correlation between the excitation and the probe beam, both the laser system and the network analyzer are locked to an external clock (synchrolock). Scanning the sample allows for spatial resolution. A pin modulator acts as a switch to enable lock-in detection.*

to the repetition rate of the laser. It is important to note, that for the resonance technique the magnetic response is measured at a fixed phase, meaning that the phase information is now hidden in the experimentally determined parameters and the resulting Kerr contrast now corresponds to the product of amplitude and phase of the pulsed experiment described above. In order to investigate the magnetic response at various phases of the excitation, the hf signal passes through a mechanical trombone delay. When changing the delay length one effectively shifts the phase of the exciting wave as shown in Fig. 3.8.
The described setup shown in Fig. 3.7 allows the imaging of the structure of dynamic eigenmodes as a function of the exciting frequency. Moreover, with this technique, resonance lines – like with the VNA-FMR technique – can be obtained optically and recorded as a function of the position on the sample. To do so, the laser spot is left at one point on the sample while scanning the frequency of the cw excitation. At every frequency the phase of the excitation is adjusted such that the maximum amplitude of the Kerr signal is obtained. The resonance frequency is reached when the Kerr rotation has a maximum.

In order to minimize noise due to mechanical vibrations both optical setups are mounted onto an optical table with air cushioning system. Note that the images from the optical setup correspond to the convolution of the z-component of the dynamic magnetization with the Gaussian probe beam. Therefore, some dynamic signal is observed even outside of the physical boundaries of the magnetic samples.

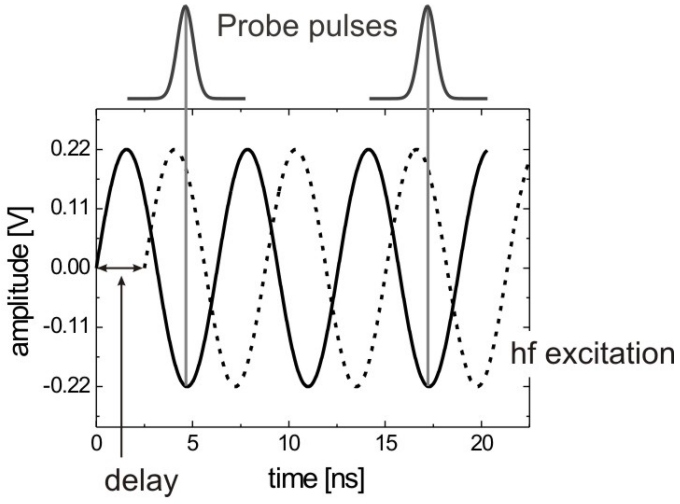

Figure 3.8: *The correlation between the continuous wave excitation and the probe pulses for the resonant Kerr technique (see Fig. 3.7). The laser pulses arrive at a repetition rate of 80 MHz. Locking the cw source (VNA) to the clock of the laser at 10 MHz ensures the laser pulses to arrive always at the same phase of the excitation (shown for 160 MHz cw excitation). A mechanical time delay between the source of the excitation and the sample allows one to shift the phase of the excitation with respect to the laser pulses. Thus, the response of the magnetic sample can be investigated at any phase of the exciting wave.*

3.3 Introduction to Micromagnetics

The resonant modal spectra (cf. Subs. 2.2.3) of magnetic elements with nonuniform magnetization configuration are often not accessible by analytical methods. However, micromagnetic simulations can be employed to confirm the experimentally obtained data. In doing so the magnetic sample is divided into small cells with uniform magnetization. For each cell the effective field $\boldsymbol{H}_{\text{eff}}$ is calculated including external fields, nearest neighbor exchange interactions, local anisotropy, and dipolar interactions. Combining Maxwell's equations and the LLG equation 2.22, both the magnetostatic fields and the temporal evolution of the magnetization can be calculated using micromagnetic simulations. Dynamic spectra are obtained from numerically integrating the equations of motion after disturbing the equilibrium configuration with an instantaneous field pulse. In order to find the frequencies of the different modes, a global Fourier transformation of the averaged time domain data is performed. The structure of the different modes can be revealed when the time domain output is transferred into the frequency domain by performing a phase sensitive local Fourier transform, illustrated in Fig. 3.9. For each pixel, the time domain data stream is Fourier transformed and subsequently reassembled in order to obtain the amplitude and phase distribution across the magnetic object as a function of frequency.
Moreover, the results from simulations are filtered by means of a 300 nm – the spatial resolution of the optical setup – two-dimensional Gaussian window in order to compare them to the experimental data. When comparing the experimental to the simulated data one has to keep in mind that simulations assume an ideal system without taking

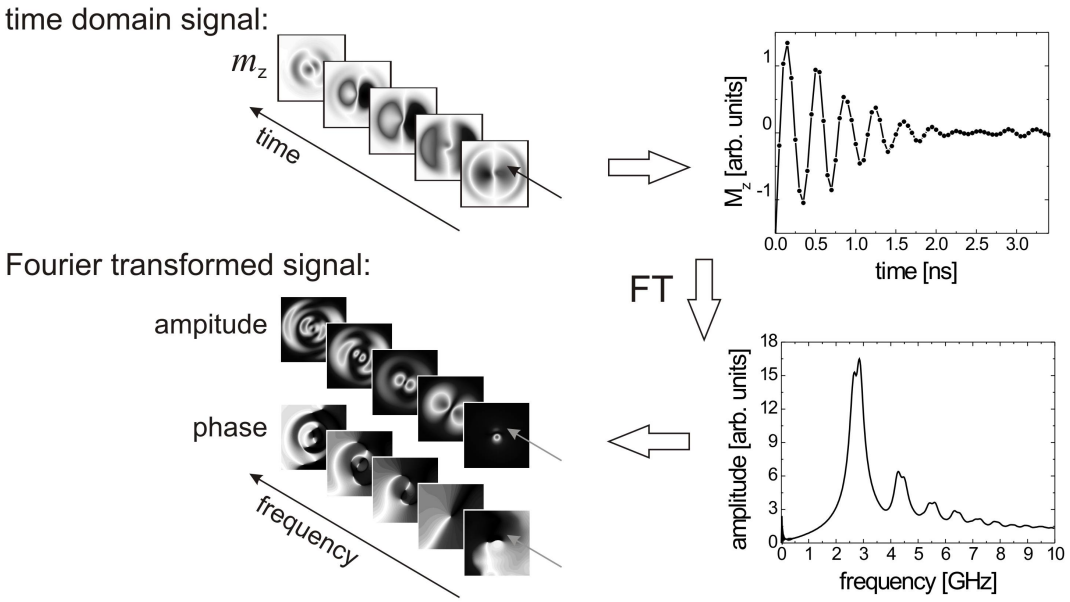

Figure 3.9: *Illustration of the local Fourier transform procedure. Each point of the image sequence in the time domain is Fourier transformed and subsequently reassembled. As a result one obtains two image sequences representing the local amplitude and phase of the excitation as a function of the frequency. See also [71].*

into account fluctuations of the magnetic properties of the sample. The results presented in this thesis are obtained from the LLG Micromagnetic Simulator programm [72] and the Object Oriented Micromagnetic Framework (OOMMF) programm [73].

4 Ultrathin Fe Film on GaAs

In this chapter the dynamic behavior of an ultrathin 16 monolayer (ML) thick epitaxial Fe film prepared on GaAs(001) substrate are presented and discussed. The focus is put on the results of Vector Network Analyzer Ferromagnetic Resonance (VNA-FMR) measurements. Since the VNA-FMR experimental setup was assembled within this thesis, its characteristic features are outlined in detail. Moreover, in order to test its reliability, in the second part of this chapter the results from VNA-FMR are compared to pulsed inductive microwave magnetometry, time resolved scanning Kerr microscopy, and conventional ferromagnetic resonance in terms of precessional frequency and effective damping. In addition, the various techniques are compared with respect to their signal to noise ratio.

4.1 Static Characterization

Details concerning the fabrication of the Fe film can be found in Appendix A.4. As shown in Section 2.2 the resonance condition can be determined by means of the effective field which can be derived from the energy functional of the system (see Eq. 2.8). The contributions arising from anisotropy are as follows. The cubic symmetry of the crystal's unit cell induces a crystalline anisotropy term equal to the one of bulk Fe [74]. In addition, the interface to the GaAs(001) substrate gives rise to an uniaxial in-plane anisotropy contribution [75]. Finally, the reduced symmetry of the film in z-direction causes an uniaxial out-of-plane anisotropy term [74]. The resulting anisotropy energy density of the system with in-plane ($\parallel$) and out-of-plane ($\perp$) contributions reads

$$\varepsilon_{\mathrm{ani}} = -\frac{K_1^{\parallel}}{2}(\alpha_x^4 + \alpha_y^4) - \frac{K_1^{\perp}}{2}\alpha_z^4 - K_{\mathrm{U}}^{\parallel,\mathrm{s}}\frac{(\hat{\boldsymbol{n}}\cdot\boldsymbol{M})^2}{tM_{\mathrm{S}}^2} - \frac{K_{\mathrm{U}}^{\perp,\mathrm{s}}}{t}\alpha_z^2, \tag{4.1}$$

where K_1 denotes the cubic crystalline anisotropy constant. Only first order terms are considered since the second term of the crystalline anisotropy vanishes for Fe(100) due to its cubic symmetry. K_{U} and $\hat{\boldsymbol{n}}$ are the uniaxial anisotropy constant and the unit vector along the direction of the uniaxial anisotropy, respectively. Note that both surface anisotropy terms $K^{\parallel,\mathrm{s}}$ and $K^{\perp,\mathrm{s}}$ are inversely dependent on the film thickness t. The directional cosines α_i are defined with respect to the [100] and the [001] axis, respectively (confer to Fig. 4.1). Since only in-plane fields are applied in the presented measurements, the out-of-plane angle ϑ is assumed to be always $\pi/2$. Thus, the

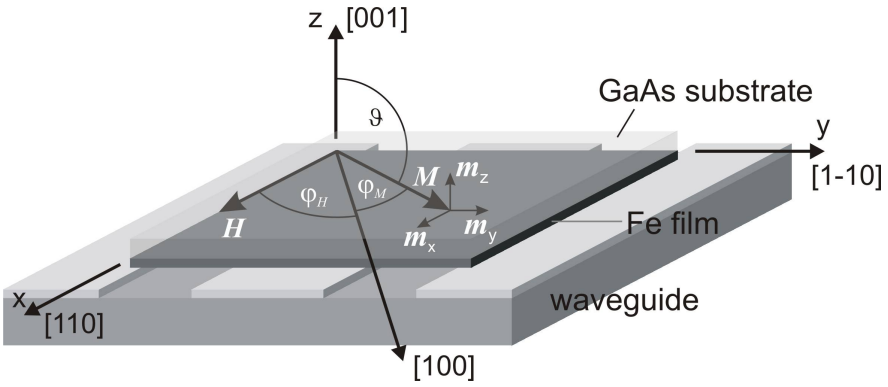

Figure 4.1: *The Fe film on top of a coplanar waveguide. The direction of the magnetic field* $\boldsymbol{H}$ *and the magnetization* $\boldsymbol{M}$ *is determined by the in-plane angle* φ *and the out-of-plane angle* ϑ*, which are defined with respect to the [100] and the [001] axis, respectively. As long as the excitation acts like a weak tipping field, the dynamic parts of the magnetization* m_i *can be separated. For small amplitude of precession, the magnetization can be separated into constant (*$\boldsymbol{M}$*) and alternating parts (*$\boldsymbol{m_i}$*).*

directional cosines are given by

$$\alpha_x = \frac{1}{M_\mathrm{S}}(M_x cos\varphi_M - M_y sin\varphi_M) \tag{4.2}$$

$$\alpha_y = \frac{1}{M_\mathrm{S}}(M_x sin\varphi_M - M_y cos\varphi_M) \tag{4.3}$$

$$\alpha_z = \frac{M_z}{M_\mathrm{S}}, \tag{4.4}$$

where φ_M is the angle between the [100] axis and the magnetization. The demagnetizing energy density of the film (see Eq. 2.14) reads

$$\varepsilon_\mathrm{dem} = \frac{\mu_0 D_M M_z^2}{2}, \tag{4.5}$$

where D_M is the effective demagnetizing factor. When the film thickness is smaller than a few MLs the demagnetizing field cannot be treated anymore in a magnetic continuum model. In this case the local dipolar field has to be taken into account. As a consequence, the dipolar field decreases when approaching the film surface. This effect leads to a reduction of the demagnetizing field, which in the case of fcc(001) layers can be accounted for by lowering the demagnetizing factor $D_M = 1 - 0.2338/L$ [58]. L is the number of atomic planes.
Substituting the directional cosines (Eqs. 4.2, 4.3, and 4.4) into 4.1 and applying 2.8 one obtains the effective anisotropy and demagnetizing field of the Fe film

$$\begin{aligned}\mu_0 H_x^\mathrm{ani} = {} & \frac{K_1^\parallel}{2M_\mathrm{S}^4}[M_x^3(cos4\varphi_M + 3) - 3M_x^2 M_y sin4\varphi_M + 3M_x M_y^2(1 - cos4\varphi_M) \\ & + M_y^3 sin4\varphi_M] \\ & + \frac{K_\mathrm{U}^\parallel}{M_\mathrm{S}^2}[M_x(1 + cos2(\varphi_M - \varphi_U)) - M_y sin2(\varphi_M - \varphi_U)]\end{aligned} \tag{4.6}$$

$$\begin{aligned}\mu_0 H_y^{\mathrm{ani}} &= \frac{-K_1^{\parallel}}{2M_{\mathrm{S}}^4}[M_x^3 sin4\varphi_M - 3M_x^2 M_y(1-cos4\varphi_M) - 3M_x M_y^2(1-sin4\varphi_M) \\ &\qquad -M_y^3(cos4\varphi_M+3)] \\ &- \frac{K_{\mathrm{U}}^{\parallel}}{M_{\mathrm{S}}^2}[M_x sin2(\varphi_M-\varphi_{\mathrm{U}}) - M_y(1-cos2(\varphi_M-\varphi_{\mathrm{U}}))] \qquad (4.7)\end{aligned}$$

$$\mu_0 H_z^{\mathrm{ani}} = \frac{K_{\mathrm{U}}^{\perp}}{M_{\mathrm{S}}^2 t} M_z + \frac{2K_1^{\perp}}{M_{\mathrm{S}}^4} M_z^3, \qquad (4.8)$$

with φ_U being the angle between the easy axis of the uniaxial anisotropy and the [100] axis.

The direction of the internal effective field $\boldsymbol{H}_{\mathrm{eff}}$ and consequently the equilibrium position of the magnetization can be determined from calculating $\partial\varepsilon_{\mathrm{tot}}/\partial M = 0$ at zero external field ($\boldsymbol{H}_0 = 0$) (cf. Eq. 2.8). Using typical anisotropy values reported for the 16 ML Fe/GaAs(001) system [75], one obtains $\varphi_M = -45°$, i.e. the easy axis is parallel to the [110] direction. This result shows that for a 16 ML Fe film the free energy in the film plane is dominated by the uniaxial interface anisotropy, in agreement with static Kerr effect measurements, shown in Fig. 4.2. The saturation magnetization and the anisotropy constants were determined by conventional FMR [76] and were found to be $\mu_0 M_{\mathrm{S}} = 2.1$ T, $K_1 = 2.7 \times 10^4$ J/m^3, and $K_\perp = 4.3 \times 10^5$ J/m^4. The dominant uniaxial in-plane anisotropy constant was found to be $K_{\mathrm{U}} = -6.15 \times 10^4$ J/m^3.

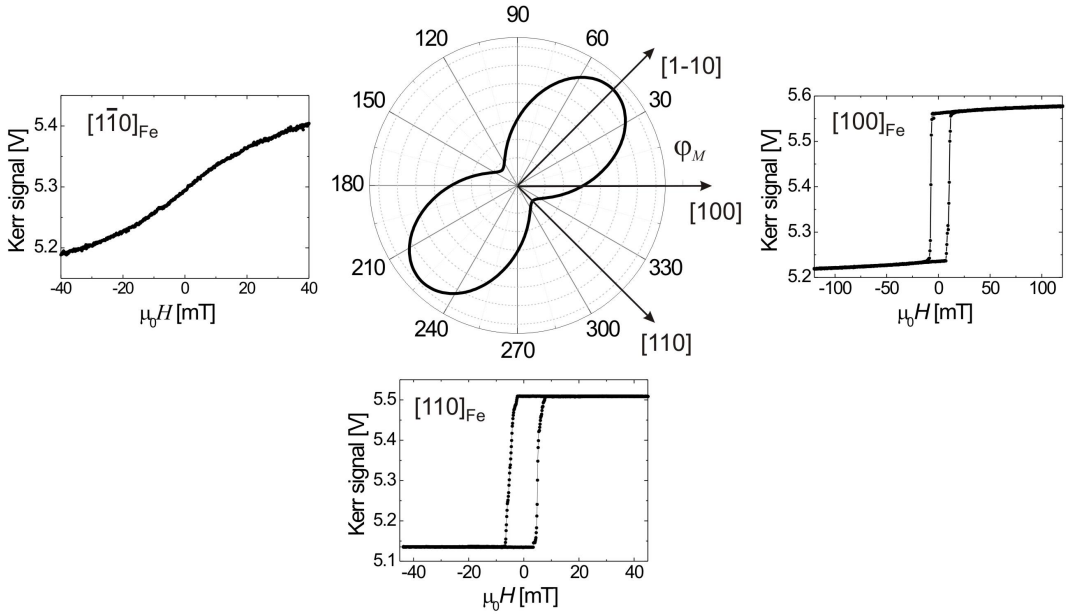

Figure 4.2: *The polar plot shows the free energy of the 16 ML thick Fe film in the plane of the film as a function of the azimuthal angle φ_M. Corresponding static Kerr effect loops are shown for the [110]- (easy axis), the [100]-, and the [1-10]-direction (hard axis).*

4.2 Dynamic Susceptibility

For dynamic measurements the static external field was applied along the x-direction and the exciting hf field along the y-direction (cf. Fig. 4.1). Under these assumptions the corresponding hf susceptibility of the system can be derived for the Fe film in a procedure similar to the one discussed in Subsection 2.2.2 and reads

$$\chi'_{yy} = \frac{\omega_M\omega_B(\omega_r^2-\omega^2)+\omega_M\omega_H\omega^2\alpha^2}{[\omega_r^2-\omega^2(1+\alpha^2)]^2+\alpha^2\omega^2(\omega_B+\omega_H)^2} \tag{4.9}$$

$$\chi''_{yy} = \frac{\alpha\omega\omega_M(\omega_B^2+\omega^2(1+\alpha^2))}{[\omega_r^2-\omega^2(1+\alpha^2)]^2+\alpha^2\omega^2(\omega_B+\omega_H)^2}, \tag{4.10}$$

containing the following convenient abbreviations (cf. Eqs. 2.28 and 2.29)

$$\omega_M = \gamma\,\mu_0\,M_\mathrm{S} \tag{4.11}$$

$$\omega_B = \gamma\,\mu_0\left(H_0+M_\mathrm{eff}+\frac{K_1^{\parallel}}{M_\mathrm{S}}\right) \tag{4.12}$$

$$\omega_H = \gamma\,\mu_0\left(H_0-\frac{2K_1^{\parallel}}{M_\mathrm{S}}-\frac{2K_U^{\parallel}}{M_\mathrm{S}}\right), \tag{4.13}$$

where the demagnetizing and the perpendicular uniaxial anisotropy fields are combined to the effective demagnetizing field

$$\mu_0 M_\mathrm{eff} = \mu_0 D_M M_\mathrm{S} - \frac{2\,K_\mathrm{U}^{\perp}}{M_\mathrm{S}t}. \tag{4.14}$$

The resonance condition now is given by

$$\omega_\mathrm{r}^2 = \omega_B\omega_H, \tag{4.15}$$

which is referred to as the Kittel equation [45] and describes the uniform precession of the magnetization as a function of the static external magnetic field H_0. In the present case, where the film is magnetized along its easy axis one obtains

$$f_\mathrm{r} = \frac{\gamma}{2\pi}\mu_0\sqrt{\left(H_0+M_\mathrm{eff}+\frac{K_1}{M_\mathrm{S}}\right)\left(H_0-\frac{2K_1}{M_\mathrm{S}}-\frac{2K_\mathrm{U}}{M_\mathrm{S}}\right)}. \tag{4.16}$$

Since frequencies instead of angular frequencies are measured, for the sake of convenience, from now on one mainly deals with the precession frequency $f = \omega/2\pi$ in place of the angular frequency ω.

4.3 Inductive VNA-FMR Investigations

4.3.1 The Excitation Field Amplitude

Analysis of the data in the linear regime is justified as long as the cone angle of the magnetic precession is small enough to apply the linearized LLG equation as it has been employed for the derivation of the susceptibility discussed in the previous subsection. In order to validate the linear approximation, the excitation field strength and the corresponding precessional cone angle was estimated for the VNA technique.
The transverse in-plane profile of the exciting magnetic field $\boldsymbol{h}_{\parallel}$ for the waveguide excitation can be calculated by applying the Karlqvist equation (see Eq. A.2 in Appendix A.2). It is depicted in Fig. 4.3 for assuming a realistic current density throughout the conductors, which is given by Emtage [77]

$$j(y) \;=\; C[1-(2y/w)^2)]^{-1/2}, \tag{4.17}$$

where w is the width of the conductor. The constant C was calculated using a commercial E-M software package [78]. A detailed discussion of the coplanar waveguide characterization can be found in Appendix A.2. All VNA measurements were carried out with a microwave power of 1 mW. Assuming an attenuation of the setup from the source to the sample of -2 dB, an amplitude of $\mu_0\,\boldsymbol{h}_{\parallel} \sim 0.02$ mT is obtained at a distance of 0.5 μm above the center of the signal line.
In order to estimate an upper limit of the maximum cone angle of the precessional motion one can compare the effective in-plane anisotropy field of $\mu_0 H_{\text{eff}} = \mu_0(K_1/M_{\text{S}} + K_u/M_{\text{S}}) \sim 50$ mT to the amplitude of the transverse in-plane excitation field $\boldsymbol{h}_{\parallel}$. When taking into account the increase of the susceptibility of $\chi \sim 160$ at resonance (see Eq. 4.10), the resulting cone angle for the VNA-FMR technique is $\theta_{\parallel} \sim 1°$. The angle of precession as a function of excitation field amplitude can be derived from the LLG equation 2.22. In the single spin approximation linear behavior was found in case of the 16 ML Fe film, for angles exceeding $\theta_{\parallel} \sim 1.5°$. As a consequence, linear approximation is justified for the VNA-FMR technique.

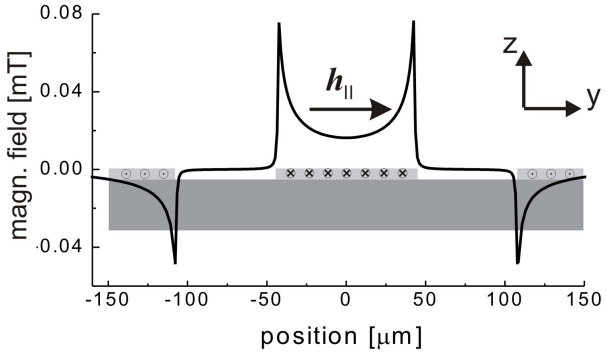

Figure 4.3: *The field profile of the transverse hf field $\boldsymbol{h}_{\parallel}$ as a function of the position on the coplanar waveguide (90 μm signal line width) at a distance $z = 0.5$ μm above the metallization. Because of nonuniform current density the field shows distinct peaks near the conductor edges.*

4.3.2 Precessional Frequency and Effective Damping

Using the vector network analyzer, the information about the dynamic properties of the magnetic sample is obtained by measuring the scattering parameters S_{ij}. However, it is still the dynamic susceptibility of the sample which contains the desired information. Since a change of the magnetic susceptibility causes a variation of the transmitted and reflected signal of the waveguide, the susceptibility can be derived from the scattering parameters obtained by the VNA. An introduction of the scattering parameters and how to convert these parameters into the susceptibility is given in Appendix A.3. By virtue of the relation between the scattering and the impedance matrix a conversion from one single parameter is possible only when measuring a reflection parameter S_{ii} and using a shorted waveguide. When measuring in transmission geometry with a continuous waveguide, the knowledge of only one scattering parameter is not sufficient for a direct conversion into χ. However, the measurements revealed that the signal to noise ratio (SNR) is clearly higher when recording a transmission parameter S_{ij}. Therefore, in the first part of this subsection the resonance line obtained from S_{12} in transmission geometry is compared to the susceptibility obtained from measuring S_{22} in reflection geometry. The reflection measurements are carried out by using a shorted waveguide with the magnetic sample placed directly in front of the short (see illustration in Fig. 4.4(a)). Data from the reflection parameter S_{22} are converted into the susceptibility by means of the procedure discussed in Appendix A.3. The resulting resonance lines for $\mu_0 H_0 = 18$ mT together with the theoretically derived susceptibilities from Eqs. 4.9 and 4.10 are depicted in Figure 4.4(a). The imaginary part of

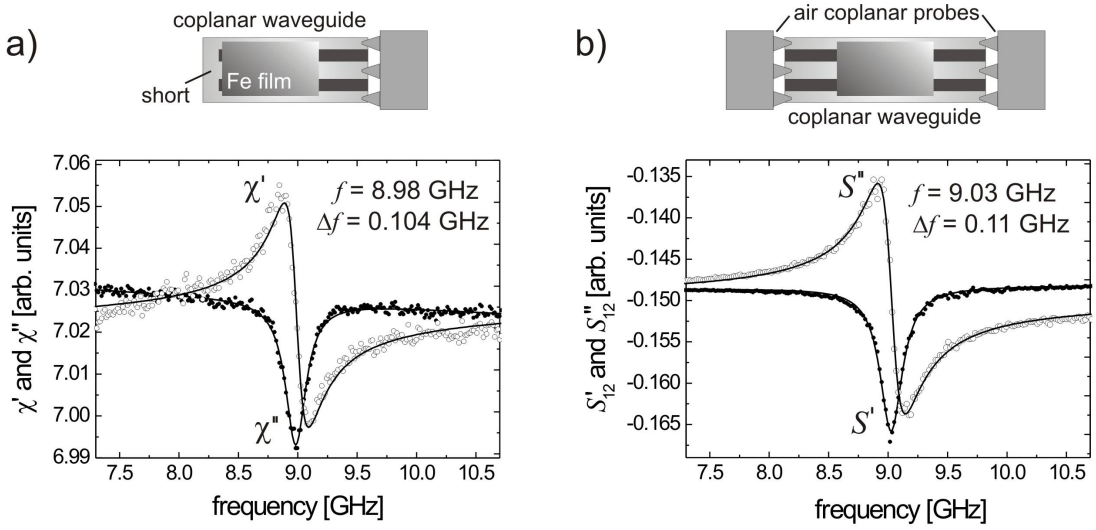

Figure 4.4: *The real and imaginary part of the susceptibility obtained from reflection measurements (S_{22}) (a) and the real and imaginary part of S_{12} obtained from transmission measurements (b). The sketches on top illustrate the measurement geometries. All data was recorded at $\mu_0 H_0 \sim 18$ mT. The solid lines represent the theoretically derived susceptibilities from Eqs. 4.9 and 4.10 for $\alpha = 0.004$. The discrepancy of the resonance frequency between the two curves might arise from bias field uncertainties.*

the susceptibility (χ'') represents the resonance absorption and thus shows symmetric line-shape. The real part of the susceptibility (χ') in turn reports of the variation of the dielectric constant and shows an antisymmetric curve. Note that both the real and the imaginary part of the resonance line are shifted by π[1] with respect to the theoretically derived susceptibility shown in Fig. 2.3. This shift arises because the experimentally determined susceptibility is measured via the absorption of the incident signal.
The resonance lines obtained from measuring S_{12} in transmission geometry (see illustration in Fig. 4.4(b)) are phase shifted in order to obtain pure symmetric and antisymmetric real and imaginary parts for S_{12}, respectively. The procedure is discussed in detail in Appendix A.1. The resulting curves are shown in Figure 4.4(b) together with the theoretically derived susceptibilities from Eqs. 4.9 and 4.10. Figs. 4.4(a) and (b) demonstrate that the measured resonance line behavior is in very good agreement with the theoretically derived curves for both the reflection and the transmission geometry. Thus, direct measuring of the susceptibility by means of a reflection parameter (S_{22}) with a shorted waveguide as well as measuring a transmission parameter (S_{12}) with a continuous waveguide yields data which show qualitatively identical behavior.
In order to extract the frequency and the linewidth from the resonance lines, the symmetric curves (χ'' and S'_{12}) are fitted to Lorentzian lines as shown in Fig. 4.5 (left and right hand side). Performing this procedure to data recorded at different static external fields yields the frequency of the precession as a function of H_0 as shown in Fig. 4.5 (center). The observed deviation of the two curves of $\sim 3\%$ likely results from external field uncertainties. Since two different waveguides were used for the transmission and reflection measurements, the position of the sample inside the electromagnet differs for the two measurements, which causes a variation of the externally applied magnetic field.
When extracting the linewidth from the Lorentzian fits, the effective damping constant α^*[2] can be derived by means of Eq. 2.34, which for the Fe film reads

$$\alpha^* = 4\pi\Delta f/(\omega_B + \omega_H), \tag{4.18}$$

$\omega_{B,H}$ are given by Eqs. 4.12 and 4.13, respectively. As shown in Fig. 4.6, again good agreement is found for the values obtained from the two different measurement geometries (transmission and reflection). Therefore, the scattering parameter obtained from transmission measurements can be assumed to be in good approximation proportional to the susceptibility of the investigated sample. In general, the desired information on the dynamic properties of a resonance spectrum includes the resonance frequency and the linewidth. Since both can be extracted from measuring the transmission scattering parameter S_{ij} as shown above and because of the higher SNR, all measurements presented from now on were carried out in transmission geometry.
In order to evaluate the experimental data, the resonance frequency as a function of the external field is fitted to the Kittel equation 4.16 (see solid line in Fig. 4.5 (center)).

[1] This phase shift arises when applying the Kramers-Kronig relation described in Appendix A.1. A phase shift of π results in a horizontal flip of both parts of the resonance line.

[2] As already mentioned, the effective damping constant α^* was introduced in order to account for the fact that the measurements do not allow to separate extrinsic and intrinsic contributions to damping.

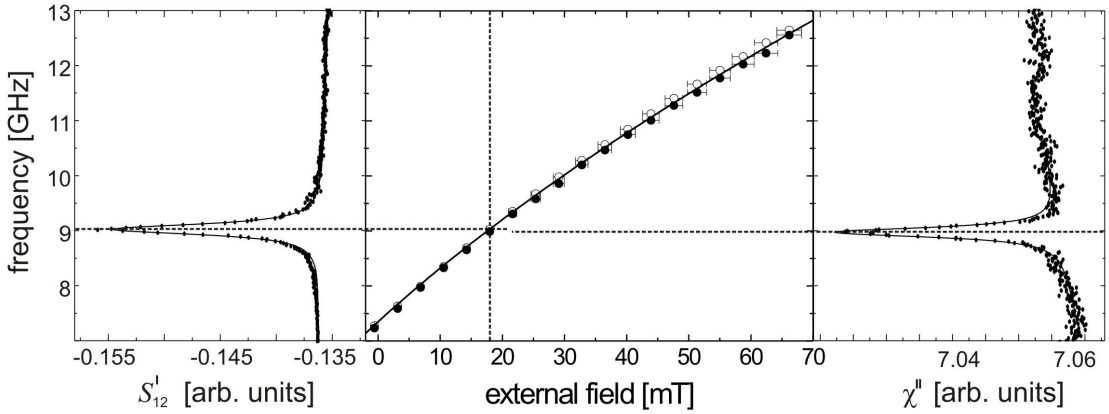

Figure 4.5: *The resonance frequency as a function of the static external field (center) extracted from S'_{12} in transmission geometry (open dots) and from χ'' in reflection geometry (solid dots). The plot on the left and right hand side show the resonance curves obtained from S'_{12} and χ'' at $\mu_0 H_0 \sim 18$ mT. The solid lines in the left and right plot are Lorentzian fits. The solid line in the center represents a fit to the Kittel equation 4.16.*

The gyromagnetic ratio is set to $\gamma = 184$ GHz/T, with a g-factor of $g = 2.09$ [79]. For the saturation magnetization M_S and the anisotropy constants K_1 and $K_\perp$ the values determined by conventional FMR were taken (cf. Subs. 4.1). The dominant uniaxial in-plane anisotropy constant was allowed to vary and used as a fitting parameter resulting in $K_U = -5.8 \times 10^4$ J/m^3. The deviation of approximately 6% from the value found by conventional FMR, might arise from aging processes of the film. However, good agreement is found between the experimental data points and the fit to the Kittel equation.

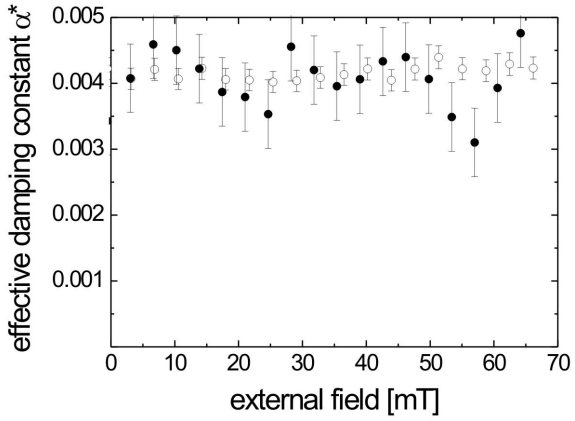

Figure 4.6: *The effective damping constant $\alpha^\star$ as a function of the static external field extracted from S'_{12} obtained in transmission geometry (open dots) and from χ'' obtained in reflection geometry (solid dots). The errors mainly arise from uncertainties of the fit $\sim 4\%$ for the transmission technique and $\sim 10\%$ for the reflection technique.*

4.3.3 Effect of Waveguide Excitation

The finite size of the waveguide and the nonuniform current density across the waveguide gives rise to an inhomogeneous magnetic excitation (see Fig. 4.3 and for details Appendix A.2). This nonuniform hf field in turn causes the excitation of spin waves, where the wave-vectors k of the excited spin waves are given by the Fourier transform of the magnetic field distribution above the coplanar waveguide. This field distribution has a maximum k-vector at $k_{\max} = \pi/\Delta y \sim 3.5 \times 10^4$ m^{-1}, where Δy is the minimum step size for the Fourier transform. The amplitude of the field Fourier transform decays to 50 % of its maximum value at $k_{50\%} \sim 10^4$ m^{-1}. As discussed by Counil et al. [80] the generation of spin waves affects both, the measured resonance frequency and the linewidth. According to reference [80] the resulting shift of the resonance frequency is given by

$$\delta f(k_{\max}, \varphi_{k_\parallel}) = \frac{1}{2}\left[f_{\mathrm{s}}(k_{\max}, \varphi_{k_\parallel}) - f_{\mathrm{r}} \right], \tag{4.19}$$

where $\varphi_{k_\parallel}$ is the angle of the in-plane wave vector $k_\parallel$ with respect to the magnetization. An expression for the spin wave frequency was derived by Arias and Mills [41]:

$$f_{\mathrm{s}}^2(k_\parallel) = f_r^2 - \frac{t}{8\pi^2}\omega_M(\omega_H - \omega_B sin^2\varphi_{k_\parallel})k_\parallel + \frac{\gamma}{4\pi^2}(\omega_B + \omega_H)\frac{2A}{M_{\mathrm{S}}}k_\parallel^2. \tag{4.20}$$

While the first part of the equation corresponds to the contribution of dipolar interaction (cf. Eq. 2.41[3]), the second part accounts for the effect of exchange interaction in case of large $k_\parallel$ (cf. Eq. 2.43). The frequency of the uniform precession f_{r} is given by 4.16. The angular frequencies ω_M, ω_H, and ω_B are defined by Eqs. 4.13, 4.11, and 4.12. Figure 4.7 shows the dispersion relation obtained from Eq. 4.20. Due to energy conservation spin wave excitation is most probable when $f_{\mathrm{s}} \sim f_{\mathrm{r}}$. Because of the strong dependence of the dispersion on the angle between the wave vector and the magnetization, spin wave excitation is effective only for small $\varphi_{k_\parallel}$. In contrast, the inhomogeneous hf field points along the y-direction and therefore favors the excitation mainly perpendicular to the static magnetization ($\varphi_{k_\parallel} = 90°$), which corresponds to Damon Eshbach spin waves. As a consequence, the resulting frequency shift is only ~ 10 MHz and thus can be neglected in the presented measurements.
Counil et al. [80] also derived an expression for the effect of linewidth broadening arising from waveguide excitation. Again the creation of spin waves on account of nonuniform hf field excitation has to be taken into account. The corresponding increase of the linewidth reads

$$\Delta f(k_{\max}) = \Delta f_{\mathrm{r}} \sqrt{1 + \left(\frac{f(k_{\max}, \varphi_{k_\parallel}) - f_{\mathrm{r}}}{\Delta f_{\mathrm{r}}} \right)^2}, \tag{4.21}$$

where Δf_{r} is the linewidth for uniform exciting field which is of the order of 0.2 GHz. The resulting linewidth broadening for the 16 ML Fe film is approximately 1 MHz for $\varphi_{k_\parallel} = 90°$ and thus can also be neglected.

[3] The expression for the magnetostatic spin waves from Arias and Mills [41] represents an approximation of Eqs. 2.40 and 2.41, where only terms linear in $k_\parallel$ have been considered.

However, the measured values of the effective damping constant α^* are almost two times bigger than the intrinsic value of α expected for bulk Fe [81]. This enhancement is most likely caused by the modified electronic structure of the ultrathin film compared to the bulk in combination with impurity and interface scattering. Safonov and Bertram demonstrated that an enhancement of the Gilbert damping can be caused by electron-magnon scattering due to impurities and defects [82]. An increase of damping by virtue of two magnon scattering in ultrathin Fe films was also demonstrated by Lindner et al. [83].

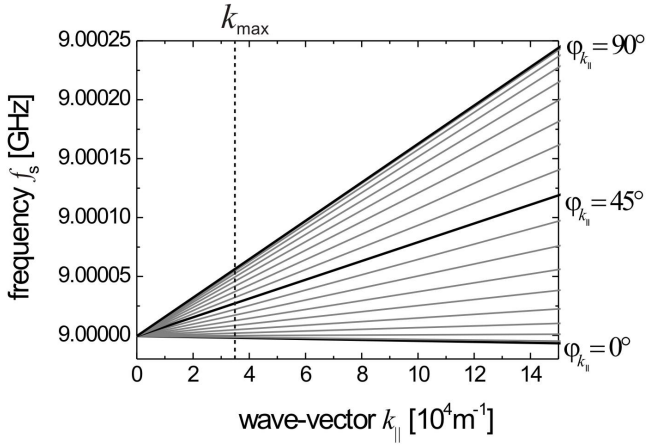

Figure 4.7: *The dispersion relation calculated from 4.20 for $f_r = 9$ GHz as a function of the angle enclosed by the wave vector and the magnetization $\varphi_{k_{||}}$. $\varphi_{k_{||}} = 0°$ and 90° correspond to the magnetostatic backward volume waves and the magnetostatic surface waves, respectively (cf. Subs. 2.2.3). The maximum k-vector k_{max} is indicated by the vertical dashed line. Since degenerate states (with respect to f_r) are essential, spin wave excitation is effective only for small $\varphi_{k_{||}}$.*

4.4 Comparison to Other Techniques

In order to prove the reliability of the novel VNA-FMR technique, the obtained results are compared in this section to Pulsed Inductive Microwave Magnetometry (PIMM), Time Resolved Scanning Kerr Magnetometry (TR-SKEM) (both methods in the time domain), and conventional Ferromagnetic Resonance (FMR) (measured by sweeping the bias field). In addition, field swept FMR measurements using the VNA-FMR setup were carried out. The experimental details concerning the different techniques have already been described in Chapter 3.

In the case of the TR-SKEM technique the magnetization configuration was not disturbed by means of waveguide excitation as described in Subsection 3.2.2. The pulse beam was instead directly focused onto the Fe film. In doing so, one generates a photocurrent across the Schottky junction at the Fe/GaAs-interface by pumping electrons inside the semiconductor. This photocurrent in turn gives rise to a circular in-plane magnetic field pulse with a rise time of a few picoseconds. The corresponding transient field disturbs the magnetization configuration. For details concerning the generation

of the magnetic field pulse by means of the Schottky diode see [71, 84].
Also for these techniques the criterion of small precession angles has to be proven before applying the linearized LLG equation (2.22). For the PIMM measurements the applied field pulses have a maximum amplitude of $\mu_0 \boldsymbol{h}_{\parallel} \sim 0.6$ mT. When comparing the hf field amplitude to the effective in-plane anisotropy field one obtains a maximum cone angle in the film plane of $\theta_{\parallel} \sim 0.7°$. Applying this procedure to the maximum field of 2.5 mT for the TR-SKEM technique results in $\theta_{\parallel} \sim 3°$. In TR-SKEM, however, the pulse duration is much shorter than a precessional period and the quasi-static approximation grossly overestimates the precessional cone angle. Moreover, in case of impulse excitation the angle of precession strongly depends on the pulse length. This effect is a consequence of the suppressed ringing when the pulse length corresponds to a half period of the magnetization precession [85].
The strength of the exciting field for the conventional FMR technique is approximately the same as for the VNA-FMR and thus results in the same angle of precession: $\theta_{\parallel} \sim 1°$. Therefore, for all techniques the linear approximation, which is valid for angles smaller than $\sim 1.5°$ can be applied.

4.4.1 Precessional Frequency and Effective Damping

In order to illustrate how the resonance frequency and the damping constant are extracted from the different techniques, the corresponding raw data are shown in Fig. 4.8.

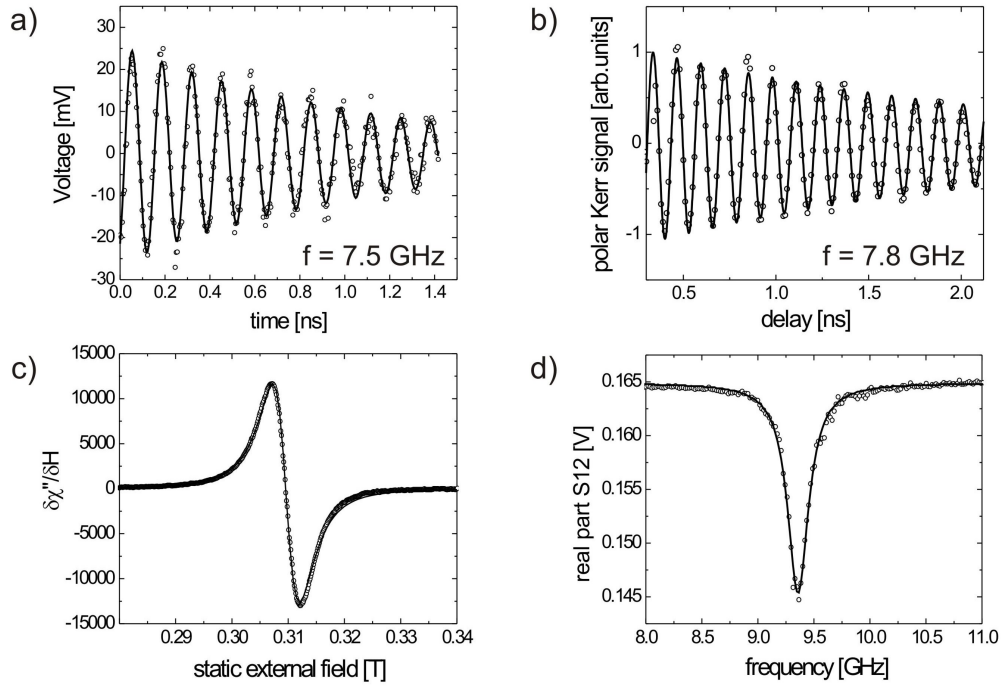

Figure 4.8: *The figure shows raw data recorded by PIMM (a), TR-SKEM technique (b) both at $\mu_0 H_0 = 0$ T, conventional FMR at a microwave frequency of 9.5 GHz (c), and VNA-FMR at $\mu_0 H_0 = 21$ mT (d). In all graphs the open circles denote the measured data points and the lines correspond to curves obtained from fits to the raw data.*

The time domain data (PIMM and TR-SKEM) is fitted to a sinusoidal function with exponential decay (see Fig. 4.8(a) and (b)). Due to lock-in detection the field domain data from conventional FMR corresponds to the derivative of a Lorentzian curve, as outlined in Subsection 3.1.1 (see Fig. 4.8(c)). The frequency domain data from VNA-FMR is fitted to a Lorentzian curve (see Fig. 4.8(d)), as mentioned in Subsection 4.3.2. A comparison of the resonance frequencies obtained from the different techniques is shown together with a fit to the Kittel equation 4.16 in Fig. 4.9. Fig. 4.9(a) depicts data from VNA-FMR, PIMM and TR-SKEM measurements. In addition data from conventional FMR measurements are shown, obtained by using the VNA-FMR setup but sweeping the bias field at fixed excitation frequency. Due to its larger field range, the conventional FMR data is depicted together with data from VNA-FMR measurements in Fig. 4.9(b). As discussed in the previous section, the influence of waveguide excitation on the resonance frequency can be neglected. Therefore, perfect agreement for the resonance frequencies obtained from VNA-FMR, TR-SKEM, PIMM, and conventional FMR techniques is expected and was indeed found (see Fig. 4.9).
In order to compare the magnetic damping both the relaxation rate from the time domain techniques and the linewidths from the frequency domain techniques are converted into the dimensionless effective damping constant α^*. The decay time τ of the induced precessional motion can be transformed into the effective damping constant by applying

$$\alpha^* = 2/(\tau(\omega_B + \omega_H)), \tag{4.22}$$

where ω_B and ω_H are given by Eqs. 4.12 and 4.13, respectively.

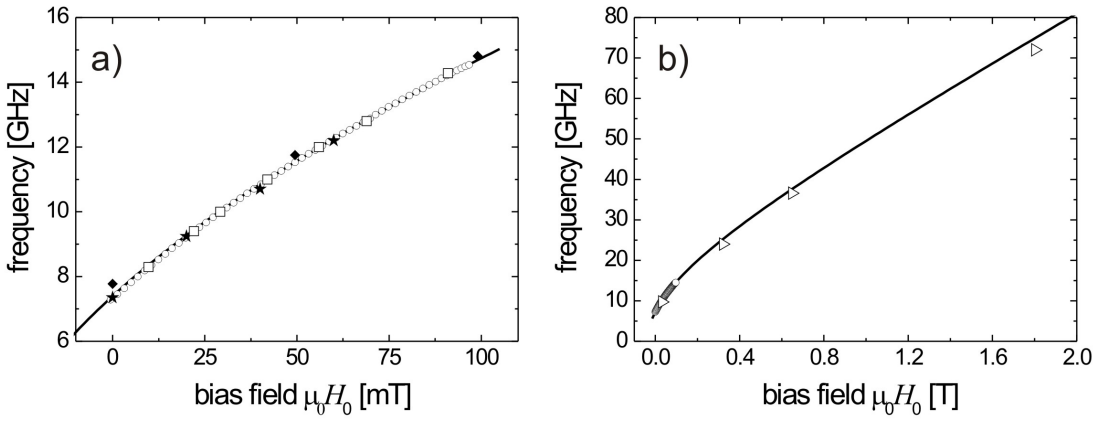

Figure 4.9: *The resonance frequency as a function of bias field H_0. (a) shows VNA-FMR data measured by sweeping the frequency (open circles) and by sweeping the bias field (open squares). Data points from PIMM and from TR-SKEM measurements are represented by stars and by diamonds, respectively. In (b) data from VNA-FMR (open circles) and conventional FMR measurements (triangles) are depicted. In both graphs the solid lines represent a fit to the Kittel equation 4.16.*

In the case of the field-swept technique the conversion from the linewidth of the resonance line reads

$$\alpha^* = \gamma\mu_0\Delta H/(2\pi f_\mathrm{r}), \tag{4.23}$$

where ΔH is defined as the half width at half maximum field linewidth (see Fig. 4.8(c)). Figure 4.10 shows the damping constants as a function of the static external field obtained from the different techniques. The larger error in the PIMM data mainly arises from the timing jitter during the measurements. The contribution from magnetic inhomogeneities to the effective damping parameter can be deduced from a decay of α^* as a function of the bias field [86]. This effect is only observable in a large range of magnetic bias fields, as it is accessible by conventional FMR (see Fig. 4.10(b)). Evidently, the contribution of inhomogeneities to the measured damping constant can not entirely explain the observed deviation from the intrinsic bulk value of approximately 50%. This finding supports the assumptions stated in the previous subsection, namely that the observed enhancement is caused by a symmetry breaking and an associated increase of impurity and interface scattering on account of the small thickness of the film.
However, the observed decrease of the damping in the TR-SKEM data of approximately 20% regarding all other techniques, might indeed arise from the influence of inhomogeneities. The probed area in the TR-SKEM technique ($\sim$ 1 μm^2) is much smaller than in any of the other techniques ($\sim$ 1 mm^2). On this length scale the magnetic properties of the sample are more homogeneous and thus the effect of line width broadening due to inhomogeneities is weaker.

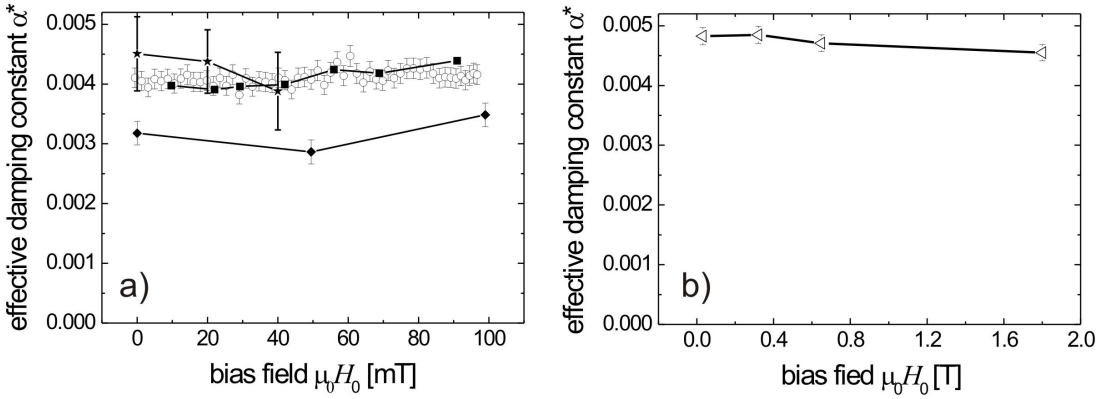

Figure 4.10: *(a) the effective damping constant α^* as a function of the external bias field H_0 obtained from VNA-FMR by sweeping the frequency (open circles) and by sweeping the bias field (solid squares). Data from PIMM and from TR-SKEM are represented by stars and diamonds, respectively. (b) shows data from conventional FMR measurements as a function of the external field.*

4.4.2 Signal to Noise Ratio

In Table 1 the SNR extracted from the measurements shown in Fig. 4.8 and the corresponding probed areas are summarized for all techniques. The SNR normalized to the number of spins for the PIMM measurements lies clearly below the values of the other techniques. The TR-SKEM technique has by far the highest SNR per spin on account of the small area which is probed. However, the VNA-FMR data has the highest SNR per spin of the inductive non-local techniques.
To achieve the mentioned SNR with the VNA-FMR technique the intermediate frequency (IF) bandwidth (cf. Appendix A.1) was set to 70 Hz and the signal was averaged over 5 measurements. The time needed to record one curve (including reference and probe measurement) was roughly 100 s.

technique	area [mm^2]	numb. of spins [μ_B]	SNR [abs.]	detect. limit [μ_B]
PIMM	0.36	1.5×10^{14}	< 10 **(1)**	6.6×10^{14}
FMR	2.0	8.5×10^{14}	~ 90 **(2)**	1.06×10^{13}
TRMOKE	2.0×10^{-7}	8.5×10^{7}	< 11 **(3)**	1.3×10^{7}
VNA-FMR	0.36	1.5×10^{14}	~ 40 **(4)**	2.6×10^{13}

Table 4.1: *The probed areas (for 16 ML film thickness), the number of Bohr magnetons within the probed volume, the absolute signal to noise ratios, and the detection limit for the different techniques.* **(1)** *at* $\mu_0 H_0 = 0$ *mT;* **(2)** *at 24 GHz;* **(3)** *at* $\mu_0 H_0 = 0$ *mT;* **(4)** *at* $\mu_0 H_0 = 60$ *mT.*

5 Confined Magnetic Structures I – Cylindrical Disks

In the previous chapter the effect of breaking the symmetry regarding the z-direction on the magnetization dynamics was illustrated by means of an ultrathin Fe film. As already addressed in Subsection 2.2.3, the confinement of the lateral dimensions down to the regime of spin wave wavelengths considerably changes the dynamic response of the magnetic system by introducing quantized excitation modes (see Fig. 2.7). A detailed understanding of the underlying physical mechanisms responsible for the modal patterns is a central question. Therefore, substantial effort has been put into the identification of the excitation spectrum of small ferromagnetic elements [5–24] and into the investigation of their switching behavior in the precessional regime [25–27], in recent years.
This chapter presents the results from detailed investigations of the eigenmode spectrum of small magnetic cylindrical permalloy (Py – $Ni_{81}Fe_{19}$) disks. In the first part the modal spectrum of disks with a diameter of 200 nm and a thickness of 15 nm is discussed on the basis of results from VNA-FMR and Brillouin light scattering measurements. Numerical calculations are employed to identify the observed modes.
In the second part of the chapter the microwave response of Py disks with a diameter of 4 μm and a thickness of 20 nm is addressed. The disks were investigated using inductive as well as spatial resolved optical techniques both in the remanent vortex state and as a function of an externally applied magnetic field. Micromagnetic simulations are employed to back up the experimental results.

5.1 Permalloy Disks with 200 nm Diameter

This section reports of the excitation spectrum of a (2×2) mm^2 sized array of permalloy disks with a diameter of $d = 200$ nm and a thickness of $t = 15$ nm. The disks were fabricated onto a Si substrate with a separation (edge to edge) of d in order to prevent inter-disk coupling. Details concerning the fabrication of the disks can be found in Appendix A.4.
By using the VNA-FMR technique the magnetic response was inductively recorded as a function of a static external bias field. As mentioned in Section 3.1, VNA-FMR measurements differ from conventional FMR in one important point: using a VNA one can sweep the frequency at a fixed external bias field while in conventional FMR the exciting hf-frequency is fixed and the external field is swept through the resonance. Thus, by means of VNA-FMR, the nonuniform spin configuration of micron sized

magnetic structures may be conserved at a fixed bias field and the resonance of this configuration is found by sweeping the frequency.

5.1.1 The Flux-Closure Vortex Configuration and its Bias Field Behavior

The ability to measure the resonant response at a fixed bias field is relevant in particular for the investigated Py disks, since their ratio of disk diameter to thickness leads to a vortex ground state [87–89]. In order to reduce the magnetic stray field energy, the magnetization vector of the element lies in the plane of the disk and curls around the center. Due to exchange interaction the spins in the center of the element assume a perpendicular orientation (see Fig. 5.1). The direction of the flux-closure and the center spin results in four different possible magnetization configurations. However, considering the symmetries of the four cases, they reduce to two different chiralities. The magnetization distribution leads to a homogeneous internal field within the flux-closed region with substantial deviations only at the edge of the element and at the vortex core. A sketch of the vortex configuration and a cross section of M_z are depicted in Fig. 5.1.
Static MOKE measurements revealed the hysteresis loops of the disks, as shown in Fig. 5.2. By virtue of the Zeeman interaction (cf. Subs. 2.1.2), the magnetic moments energetically favor parallel alignment to an external magnetic field. Therefore, in the case of the vortex configuration, a static in-plane field increases the size of the domain with parallel orientation. This effect in turn causes a displacement of the vortex core perpendicular to the bias field [90, 91], as illustrated by insets (b) and (d) in Figure 5.2. For bias fields larger than the annihilation field of $\mu_0 H_{\mathrm{ann}} \sim 70$ mT, the vortex core is expelled from the disk and a quasi uniform magnetization configuration is obtained (see

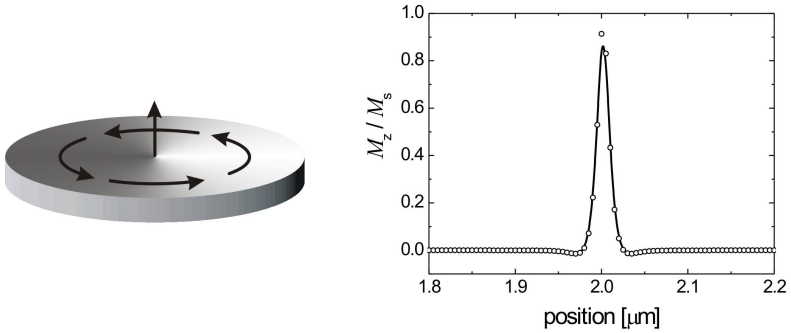

Figure 5.1: *The magnetization configuration of a vortex ground state (left). Except for the perpendicular magnetization component at the disk center, the magnetization forms a flux-closure configuration. Right: a line-scan across the disk center reveals the magnetization profile for M_z. The magnetization profile represents a zoom into the center region of a disk with 4 µm diameter, extracted from micromagnetic simulations using the LLG code [72] with 5 nm discretization. The demagnetizing field leads to a region around the vortex core having a perpendicular magnetization component opposite to the vortex core magnetization. The solid line represents a guide to the eye.*

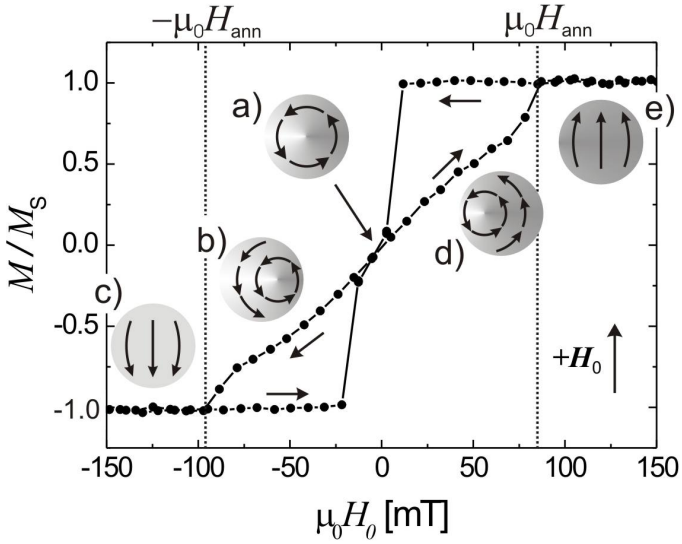

Figure 5.2: *The hysteresis loop for the Py disks with a diameter of 200 nm and a thickness of 15 nm recorded by static Kerr measurements. The insets illustrate the magnetization configuration during the hysteresis loop. The vertical dotted lines denote the vortex annihilation field at* $\mu_0 H_{\mathrm{ann}} = \pm 70\ mT$.

insets (c) and (e) in Fig. 5.2). Returning back to zero field, the vortex core nucleates again in the disk (see inset (a) in Fig. 5.2). Indeed, due to the transition threshold from the uniform to the vortex configuration and vice versa, the nucleation field is considerably smaller compared to the annihilation field, which causes the observed hysteretic field behavior.

5.1.2 Dynamic Measurements and Numerical Calculations

For the VNA-FMR measurements, the disks on the Si substrate were placed on top of the signal line of a coplanar waveguide (signal line width $w = 90\ \mu$m). The external bias field was applied in the disk plane parallel to the waveguide. The results from the VNA-FMR measurements are compared to data from numerical calculations and Brillouin Light Scattering (BLS) experiments previously obtained for the same sample (see Giovannini at al. [19]). The numerical calculations are based on the subdivision of the particle into small cells and the development of a dynamical matrix approach which allows simultaneous determination of the frequency and the dynamical magnetization profile of all the normal modes of the disk. In this model dipolar, Zeeman, and exchange interactions are considered. For further details concerning the theoretical method see Giovannini et al. [19].

The BLS experiments were carried out in the Group of High resolution Optic Spectroscopy and related Techniques (GHOST) laboratory at the University of Perugia. For details see [19, 92].

Figure 5.3 shows the resonance frequencies as a function of the bias field obtained from VNA-FMR and BLS measurements and numerical calculations. In the vortex state up to 8 distinct modes (see also Fig. 5.4(a), which reveals 7 distinct peaks) and in

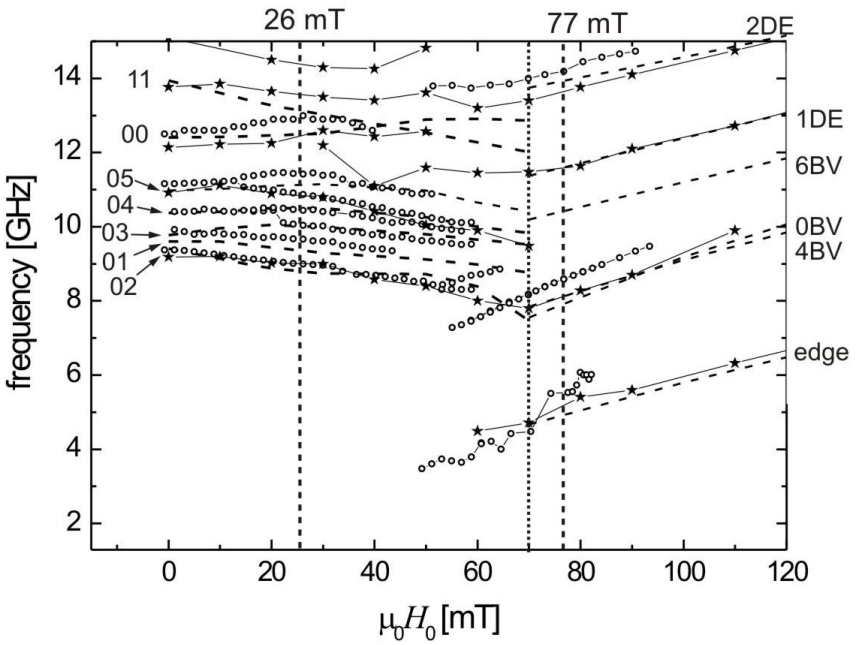

Figure 5.3: *Experimental data from VNA-FMR (open circles) and BLS (stars) together with calculated frequencies (dashed lines) for the Py disks as a function of the external bias field H_0. The vertical dotted line at $\mu_0 H_{\mathrm{ann}} = 70\ mT$ assigns the transition from the vortex to the saturated state. The calculated lines are labeled by (n = number of radial nodes, m = number of azimuthal nodes) for the vortex state and by BV (backward volume like) and DE (Damon Eshbach like) for the saturated state with the corresponding number of nodal lines. The vertical dashed lines at $\mu_0 H_0 = 26\ mT$ and 77 mT indicate the positions where corresponding raw data is shown in Fig. 5.4(a) and (b), respectively.*

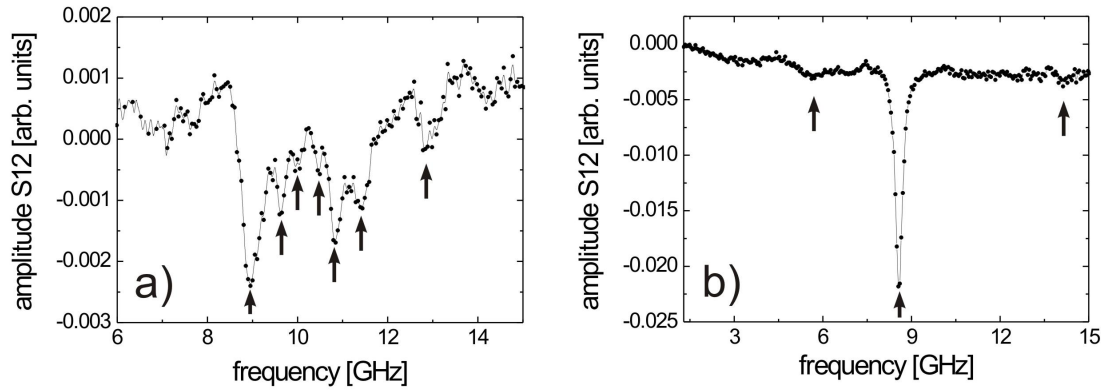

Figure 5.4: *Raw data for the VNA-FMR measurements of the Py disks. (a) In the vortex state the spectrum shows 7 distinct absorption peaks at $\mu_0 H_0 = 26\ mT$. (b) In the uniform magnetized configuration above the vortex annihilation field 3 distinct peaks are observed at $\mu_0 H_0 = 77\ mT$.*

the saturated state up to 3 distinct modes (see Fig. 5.4(b)) were observed by means of VNA-FMR. They show very good agreement with both the BLS data and the calculated frequencies. Absorption peaks arising from ferromagnetic resonance were identified in the VNA-FMR spectra by means of their dependence on the external magnetic bias field. Peaks which do not change position as a function of the bias field have not been considered here. The modal structures were derived from the numerical calculations as shown in Fig. 5.5 and reveal the number of nodal lines. Accordingly, the calculated frequencies in Fig. 5.3 are labeled by (n = number of radial nodes, m = number of azimuthal nodes) for the vortex state and by BV (backward volume like) and DE (Damon Eshbach like) for the saturated state with the corresponding number of nodal lines. The branch in Fig. 5.3 labeled by 'edge' represents the mode localized at the disk edges as shown in Fig. 5.5(n). When analyzing the VNA-FMR data, above the vortex annihilation field one finds a dominant mode in the raw data at $f = 8.6$ GHz and $\mu_0 H_0 = 77$ mT (see Fig. 5.4(b)), which can be identified from calculations to be the fundamental BV mode. This mode corresponds to the quasi uniform precession of

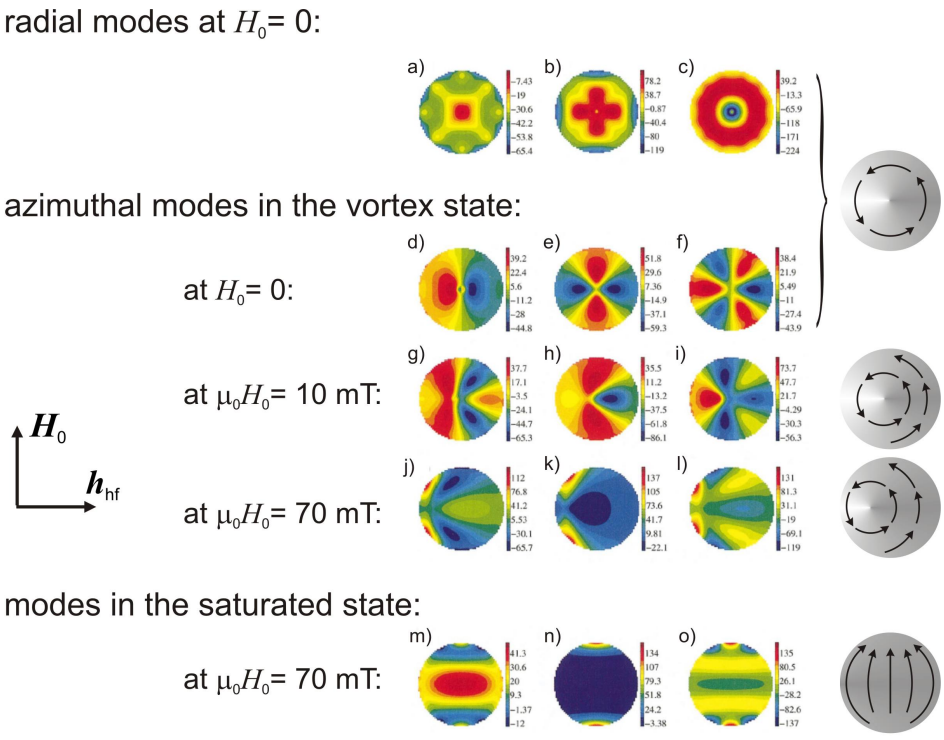

Figure 5.5: *The real part of $\delta m_z(r)$ of the disk with 200 nm diameter obtained from numerical calculations. Pictures (a)-(c) and (d)-(f) represent radial and azimuthal modes at zero bias field, respectively. Pictures (g)-(i) and (j)-(l) show azimuthal modes at $\mu_0 H_0 = 10$ mT and 70 mT, respectively in the vortex state for an up-sweep. Pictures (m)-(o) show modes at $\mu_0 H_0 = 70$ mT in the saturated state for a down-sweep. Up and down sweeps correspond to the two directions of the hysteresis loop shown in Fig. 5.2. Illustrations on the right hand side clarify the corresponding magnetization configuration. The images of the modes are taken from [19].*

the magnetic moments throughout the disks. In addition, the second DE mode and an edge localized mode has been observed by means of VNA-FMR. The fourfold symmetry observed in the structure of the radial mode (2, 0) depicted in Fig. 5.5(c) might arise from the cubic discretization of the disk. In the case of mode (0, 0) and (1, 0) depicted in Fig. 5.5(a) and (b), respectively, this effect may additionally be enhanced by mode coupling [19].

5.1.3 The Dispersion of the Observed Modes

When analyzing the radial and azimuthal modes concerning the orientation of their wave vectors with respect to the static vortex magnetization configuration, one finds the wave vector to be perpendicular to $\boldsymbol{M}$ in case of the radial modes and parallel to $\boldsymbol{M}$ in case of the azimuthal modes. These two different orientations correspond to the magnetostatic surface and backward volume spin waves, respectively, described in Subsection 2.2.3. Indeed, the frequency behavior of the two modes as a function of their number of nodes depicted in Fig. 5.6 shows positive dispersion for the radial modes and negative dispersion for the azimuthal modes for less than three nodes. Due to the small lateral size of the disks, the dominant interaction determining the nature of the modes, changes from dipolar to exchange already for modes with three nodes. As a consequence, for the azimuthal modes the modal frequency assumes a minimum for two nodes and again increases when adding additional nodes (see solid triangles in Fig. 5.6). For the radial modes the exchange interaction causes a steeper increase of the frequency which also starts at three nodes (see solid dots in Fig. 5.6). Exactly the same behavior was derived theoretically as shown in Subsection 2.2.3.
In addition, also in the saturated state, modes with Damon Eshbach (labelled DE) and backward volume (labelled BV) like behavior are found. This indicates that the two modes are quantized parallel and transversal to the static magnetization, respectively.

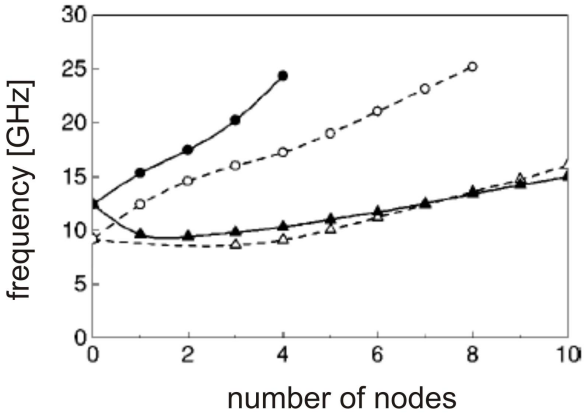

Figure 5.6: *The dispersion of the various modes obtained from numerical calculations. Solid circles and triangles show the behavior of radial and azimuthal modes, respectively for the vortex state. Open circles and triangles correspond to surface and backward like modes, respectively in the saturated state of the disks. The graph is taken from [19]*

Even though, the dispersion relation of the saturated state qualitatively shows the same behavior as the one of the vortex state, the transition form dipole to exchange dominated modes is shifted to higher node numbers for the DE modes regarding the radial modes of the vortex state. This shift arises from weaker lateral confinement of the waves in the saturated state. While the domain of the saturated state is extended throughout the whole disk, the vortex state consists of two domains regarding the dynamic response to an in-plane hf field (see illustrations top and middle on the right hand side in Fig. 5.5).

Although good agreement between the VNA-FMR data, the BLS data, and the calculated frequencies is found, the observed discrepancies might mainly arise from errors due to the fitting of the experimental data and from bias field uncertainties.
It is worth noting that the extent of the disk array of (2×2) mm^2 was larger than the width of the signal line of the waveguide (90 μm). Therefore, the hf-field was not in the plane of the dots throughout the whole array but had a strong out-of-plane component near the edges of the waveguide (cf. Appendix A.2). Since for the waveguide excitation the coupling of the hf-field to the different modes is crucial, the VNA-FMR measurement was sensitive not only to modes with an odd number of azimuthal nodes, as expected for pure in-plane excitation (explained in detail in Section 6.3). Indeed, the out-of-plane component of the excitation field allowed to observe modes also with an even number of azimuthal nodal lines as shown in Fig. 5.3.

5.2 Permalloy Disks with 4 μm Diameter

The potential of VNA-FMR for the investigation of nano-structured magnetic elements having nonuniform magnetization configuration has been demonstrated in the last section. Thereby, the spatial structure of the modes has been derived from numerical calculations. In contrast, the optical techniques described in Section 3.2 allow to directly observe the modal pattern. However, since the spatial resolution is limited to 200 nm minimum, the modes of the disks with 200 nm diameter cannot be resolved by means of these techniques. Thus, in order to experimentally resolve the modal structure of cylindrical dots, Py disks with 4 μm diameter were investigated. The obtained results are discussed in this section.
In a first approach the magnetic response of the individual disks are imaged by applying both pulsed (TR-SKEM) and continuous wave (FMR-SKEM) excitation. These experiments were performed in zero bias field. Subsequently, VNA-FMR and FMR-SKEM experiments disclose the dynamic behavior of the disks as a function of a static in-plane magnetic bias field. Micromagnetic simulations are employed to confirm the experimental results.

5.2.1 Static Characterization

The sample studied experimentally is an array of 1 × 100 ferromagnetic permalloy ($Ni_{81}Fe_{19}$) disks with a diameter of $d = 4$ μm fabricated by e-beam lithography and

lift-off technique directly on top of the signal line of a coplanar waveguide (signal line width $w = 10$ μm). In order to prevent inter-disk coupling an edge to edge distance of $d/2$ was chosen. For corrosion protection the disks were capped with 2 nm Aluminium. A detailed description of the sample preparation can be found in Appendix A.4. X-ray fluorescence was used to obtain the sample thickness on a wafer prepared at the same time as the actual samples. On the same wafer the magnetic moment of the permalloy samples was determined by means of Superconducting Quantum Interference Device (SQUID) magnetometry. These measurements yielded a saturation magnetization and a thickness of $\mu_0 M_S = 1.0$ T and $t = 20$ nm, respectively.
The diameter to thickness ratio of the disks again leads to a vortex ground state (see Figs. 5.1 and 5.7 (a)), which was confirmed by X-ray photo emission electron microscopy measurements using the circular magnetic dichroism (XMCD) at the Surfaces/Interaces Microscopy beam line of the Swiss Light Source (see Fig. 5.7(b)).

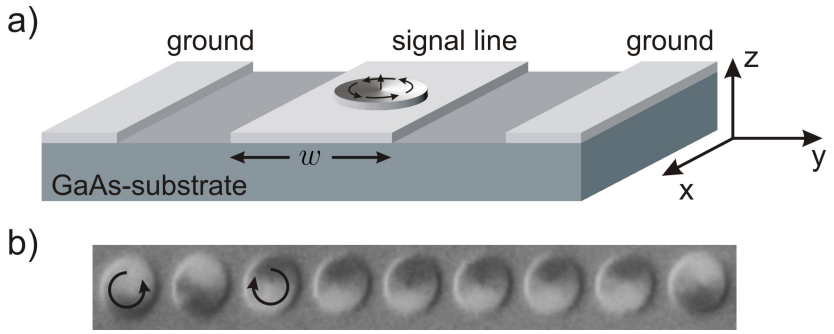

Figure 5.7: *A permalloy disk on top of the coplanar waveguide. The schematic sketch in (a) illustrates the flux-closure vortex configuration. (b) photoemission electron microscopy investigations confirm the equilibrium ground state of the disks to be a vortex. The black/white contrast represents the y-component of the magnetization* $\boldsymbol{M}$.

5.2.2 Energetics and Micromagnetics

The normal mode spectrum of ferromagnetic elements is governed by the total internal field $\boldsymbol{H}_{\text{eff}}$ (see Eq. 2.8) and the relevant boundary conditions. In this size and thickness regime it is justified to use purely dipolar boundary conditions to describe the low lying normal eigenmodes [28, 53]. In a two dimensional approximation the components of $\boldsymbol{M}$ which are perpendicular to the boundaries lead to an infinite magnetostatic energy, which can be avoided by strictly pinning the magnetic moments at the boundaries of the sample. In the case of a vortex configuration the exchange contribution at the core region can be accounted for by a second boundary condition, which implies a pinning of the magnetic moments at the vortex core [93]. In contrast, in micromagnetic simulations the behavior of the magnetic moments at the boundaries is naturally described by Maxwell's equations. A more thorough analysis of the normal mode spectrum of flux-closed ferromagnetic disks can be found in [94–96] and references therein.
The small anisotropy field of permalloy is ignored in the following and the external exciting field serves merely as a tipping hf field. In the micromagnetic simulations, the

disks are subjected to a short instantaneous field pulse $\boldsymbol{h}_{\text{pulse}}$ with 0.5 mT amplitude and a duration of 50 ps. The external hf and static field were applied along the y- and x-direction, respectively. The magnetic properties of the permalloy disks used in the simulations are as follows: exchange constant $A = 13 \times 10^{-12}$ J/m, anisotropy constant $K_{\text{u}} = 0$, saturation magnetization $\mu_0 M_{\text{S}} = 1$ T, and damping constant $\alpha = 0.008$. Micromagnetic simulations were performed using the LLG code [72] unless stated otherwise, on a 5 nm and 15 nm grid for disks with and without vortex core, respectively. The equations of motion were integrated in 0.5 ps steps from $t = 0$ to 5 ns. For the simulations with the LLG code, edge corrections were applied to the boundary of the disk. In order to find the frequencies of the different modes global Fourier transformation of the averaged time domain data was performed. A deeper insight into the structure of the excited modes was obtained by employing the phase-sensitive local Fourier transformation procedure described in Subsection 3.3, which transforms the time domain image sequence into the frequency domain.

5.2.3 Normal Mode Structure at Zero Bias Field

Fig. 5.8 shows the z-component of the magnetization at $H_0 = 0$ averaged over one half of the disk as a function of time elapsed after application of the tipping field pulse. The magnetic field pulse is generated via focusing the red laser pulse onto a photoconductive switch, which launches a current pulse into the coplanar waveguide (cf. Subs. 3.2.2). The current pulse shown as inset in Fig. 5.8(a) was recorded by using a 20 GHz sampling oscilloscope and has a maximum amplitude of ~ 44 mA[1]. The transverse field amplitude calculated by employing Eq. A.2 is ~ 3 mT. For the detailed high frequency field profile see Appendix A.2.
In Figs. 5.8(a) and (b) the experimental and simulated data, respectively obtained from a 3.4 ns (experiment) and 5 ns (simulation) long image sequence is shown. In both cases one immediately realizes that more than a single frequency is responsible for the time evolution. Fourier Transformation (FT) into the frequency domain confirms this finding and shows peaks at 2.6 GHz (2.65 GHz and 2.85 GHz), 4.0 GHz (4.37 and 4.47 GHz), and 5.4 GHz (5.43 and 5.61 GHz) for the experimental (simulated) results (see Figs. 5.8(c) and (d)). Note that in this enumeration only peaks which are found both in experiment and simulation have been considered. Zero-filling and a Hamming cutoff window were used in the FT. Note that all peaks in the micromagnetic simulation show a doublet structure, which is discussed later in this subsection when analyzing the locally Fourier transformed data.
When zooming into the central region of the element, in the micromagnetic simulation one observes the precession of the vortex core around the center of the disk with a frequency of 70 MHz as shown in Figs. 5.9. This gyrotropic oscillation of the vortex core was described in detail by Thiele [97] and was observed experimentally in [16, 20, 70, 98]. Since the maximum scan length of the experimental time delay is 3.4 ns, which corresponds to a resolution of approximately 0.3 GHz in the Fourier transformed data, the gyrotropic mode cannot be detected in this experiment.

[1] An attenuation of -3 dB from the sample to the oscilloscope was assumed

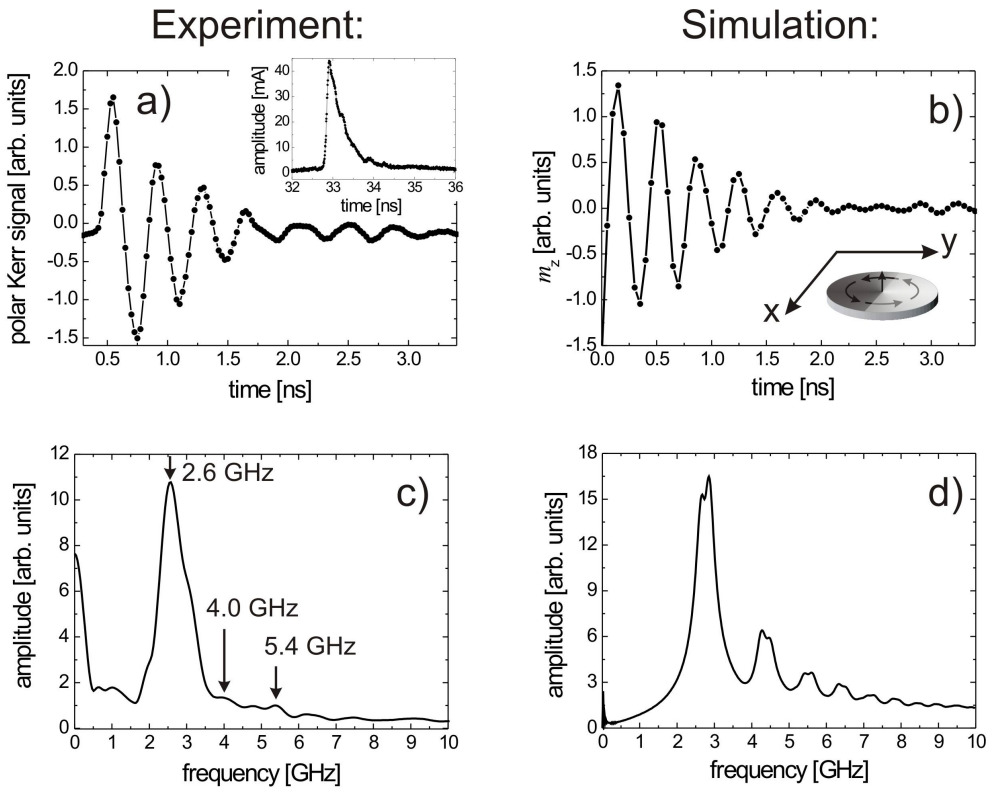

Figure 5.8: *The dynamic z-component of the magnetization* $\boldsymbol{M}$ *as a function of time obtained from time-resolved magneto-optical Kerr microscopy (a) and micromagnetic simulation (b) averaged over one half of the disk (see inset in (b)). The corresponding Fourier transform of the experimental and the simulated data is shown in (c) and (d), respectively. The inset in (a) depicts the tipping pulse applied in the TR-SKEM experiment.*

In order to analyze the excited modes with greater detail, local Fourier transformations of the data were performed as explained in Subsection 3.3 (see Fig. 5.10(a)). The corresponding modal structure is reminiscent of Bessel functions of first order [21, 93], but shows an additional node in the azimuthal direction caused by the asymmetry of the torque on account of the in-plane field pulse excitation. For a field pulse applied along the y-direction, the two sides of the disk experience an opposite initial torque. This phase shift by π can be observed in the phase of the modes. The modes in Fig. 5.10 are labeled by (n, m = 1) according to the number of radial (n) and azimuthal (m) nodes. For these normal modes the frequency increases with increasing radial node number as shown by Buess et al. [53], where a simple model based on purely dipolar excitations is employed. In a more sophisticated approach Zivieri and Nizzoli [96] calculated the modal spectrum of cylindrical dots by taking into account the influence of both surface and volume dynamic exchange interaction and dipolar fields. Here, the analysis is limited to the comparison to micromagnetic simulations. In the simulations, shown in Fig. 5.10(b), also Bessel function like modes (n, m = 1) are observed.

As already mentioned, the global FT (see Fig. 5.8(d)) of the simulated data reveals a doublet peak structure. When analyzing the local FT obtained from the raw image

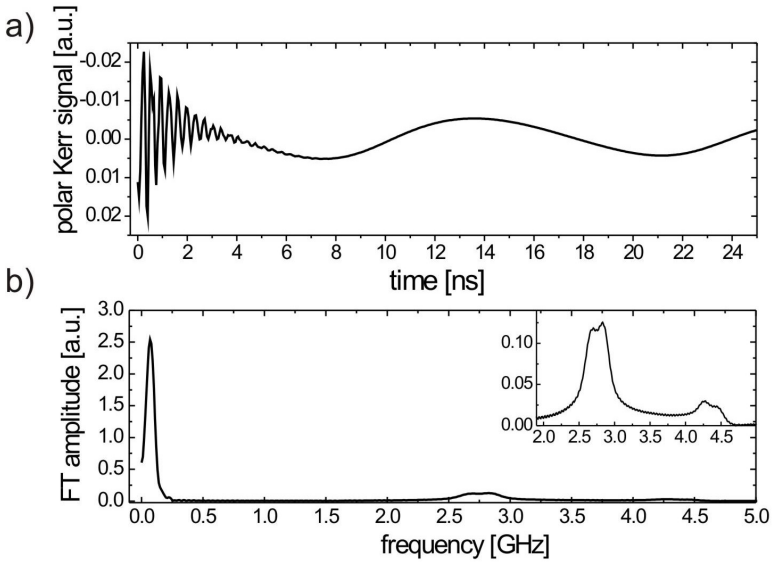

Figure 5.9: *(a) The Kerr signal averaged over the disk center. (b) The Fourier transform reveals a clear peak at 70 MHz which corresponds to the gyrotropic vortex motion. The inset represents a zoom into the normal mode spectrum (see Fig. 5.8(d)).*

series from simulation not only one clear mode with (n = 1, m = 1) is found, but a second mode is observed in the local FT which shows nearly equal features, exemplarily depicted for mode (1, +1) and mode (1, -1) in Fig. 5.10(b). However, these pairs of modes differ in their phase. While the phase of mode (1, +1) seems to circulate clockwise, it seems to circulate counterclockwise around the disk center for mode (1, -1). The splitting of the azimuthal modes, which has already been observed experimentally by Zhu et al. [22] and by Park and Crowell [99], has recently been explained by Ivanov and Zaspel [95]. According to reference [95] the vortex core breaks the azimuthal symmetry of the disk. Coupling between the vortex core and the magnetostatic spin waves lifts the degeneracy of the clockwise and counterclockwise travelling magnons. As a consequence of the frequency splitting, the two magnons circulate with different velocities around the disk center. Therefore, their superposition, namely mode (1, ±1), appears to be tilted with respect to the direction of the exciting field pulse [99]. In fact, when the central part of the disk is removed in the simulation neither peak splitting nor a tilting of the modes is observed as shown in Fig. 5.11. In Fig. 5.11(a) the global Fourier transform of a simulated image sequence for a 4 micron disk is shown where the central 20 nm have been removed. Consequently, the disk shows no perpendicular magnetization component at the center. One immediately finds that the peak splitting observed in Fig. 5.8(d) has disappeared and the peak position assumes a value between the two peaks of Fig. 5.8(d).

Although a very broad peak is obtained in the experiment with a clear shoulder at 3.0 GHz in the global FT of the fundamental mode (1, 1) (see Fig. 5.8(c)), no second mode with opposite circulating phase was observed in the local Fourier transform of the data from TR-SKEM. This might come from imperfections of the real sample, which leading to pinning centers for the vortex core. Hence, the gyrotropic motion might be disturbed and the interaction with the normal modes may be attenuated.

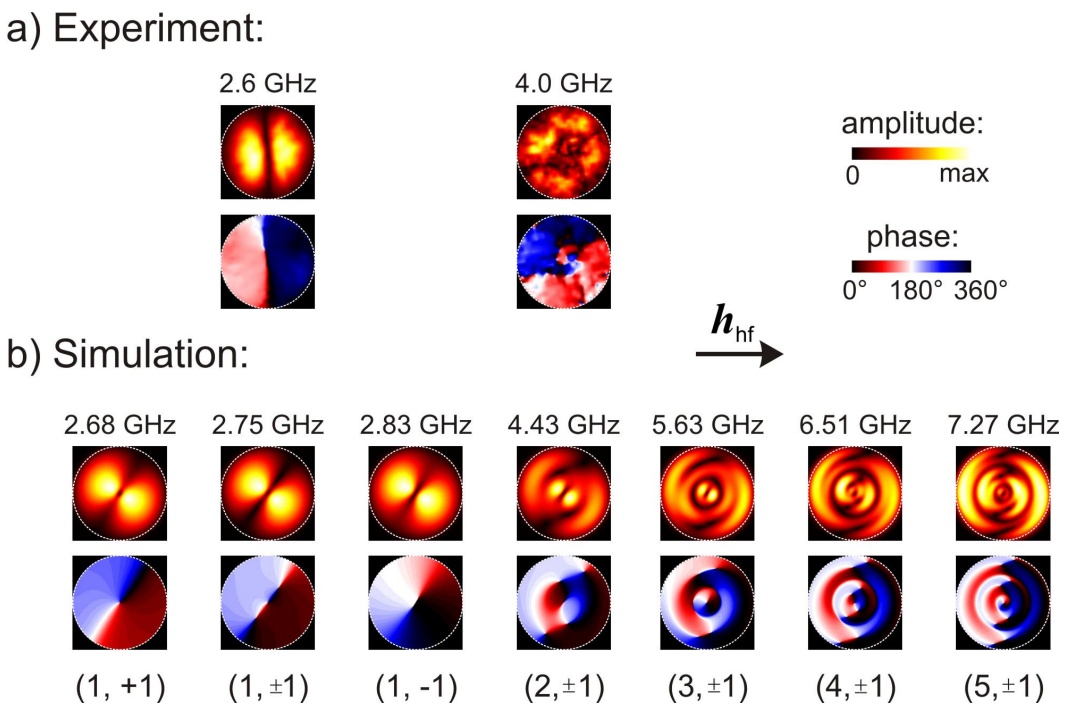

Figure 5.10: *Amplitude (upper row) and phase (lower row) generated by local Fourier transform of the time domain data obtained from TR-SKEM (a) and micromagnetic simulations (b) at zero bias field. The modes are labelled by (n, m) according to their number of radial (n) and azimuthal (m = 1) nodes. Both peaks of the doublet structure observed in the global FT from simulation in Fig. 5.8 are exemplarily shown for the fundamental mode (1, ±1). The phase of mode (1, +1) and mode (1, -1) seems to circulate clockwise and counterclockwise around the center, respectively. In addition, the superposition is shown, which was found at the frequency between the two modes. For mode (2, 1) to mode (5, 1) only the superpositions (±-mode) of the doublet structures are shown.*

Moreover, the splitting of the doublet structure is expected to be of the order of the vortex gyrotropic frequency [99], which with 70 MHz is rather small for the investigated disks. However, when decreasing the lateral dimensions of the disk, the frequency of the vortex motion increases, which in turn should increase the splitting of the normal azimuthal modes. Consequently, the splitting was indeed observed experimentally in disks with diameter smaller than 3 μm by Park and Crowell [99] and by Hoffmann et al. [100].

An alternative experimental approach to investigate the modal spectrum of the disks, is to exclusively excite the different modes by means of a continuous wave excitation [9, 69]. This can be realized by combining the resonant excitation (VNA) with the magneto-optical detection scheme (FMR-SKEM) as described in Subsection 3.2.3. If the magnetic excitations are eigenmodes of the disks, the dynamic response obtained from the pulsed and cw technique are expected to be transformable into each other via Fourier transformation. However, since the magnetization is subjected to forced precession, the continuous wave technique employed for the measurements of this work does not allow to study the temporal evolution of the modes. For this reason the mutual

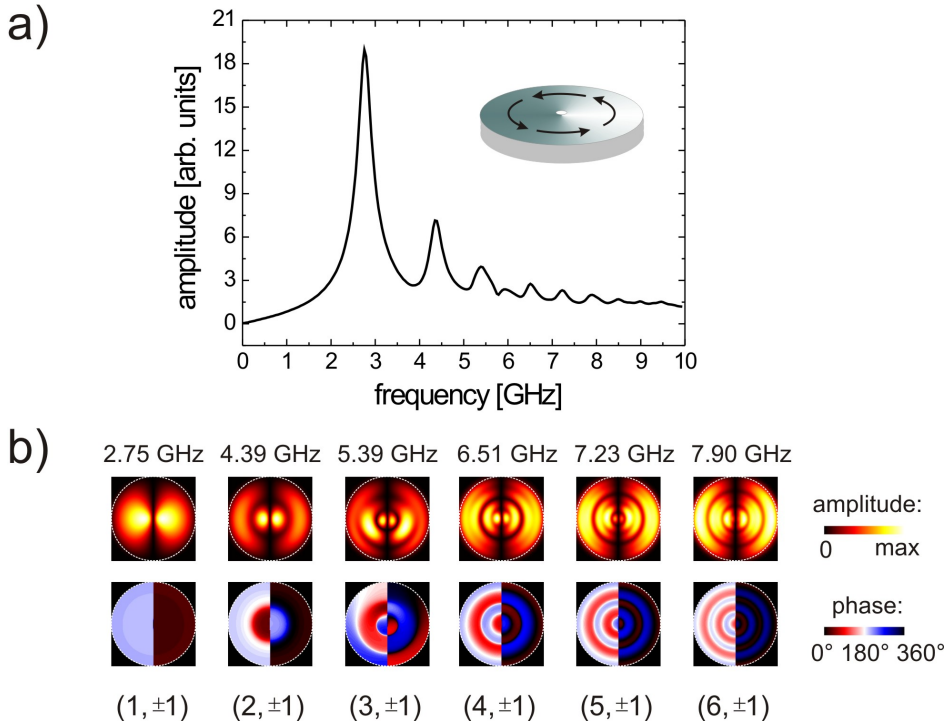

Figure 5.11: *The global (a) and local (b) Fourier transform of the time evolution of the magnetization for a disk with a hole (20 nm diameter) at its center obtained from simulation. The schematic sketch illustrates the corresponding magnetization configuration lacking the perpendicular magnetization component in the center. For the disk with a hole located at the center the peaks in the global FT do not show any splitting as it was observed for regular disks without a hole. In addition, no tilt of the modes is observed in this case (see (b)).*

coupling of the normal modes with each other and to the vortex core is not accessible by means of FMR-SKEM. However, one advantage of exclusively exciting single modes instead of triggering a complicated superposition of modes is the possibility to observe higher order modes. Due to the strong decay of the overall signal using pulsed excitation, only mode (1, 1) and (2, 1) could be extracted from the experimental data from TR-SKEM (see Fig. 5.10(a)). In contrast, using cw excitation, normal modes (n, 1) could indeed be detected up to n = 5. Fig. 5.12(a) shows the normal modes up to fifth radial order obtained from FMR-SKEM measurements. The frequencies of the modes are in good agreement with both the pulsed experiment and the simulations. Again only modes with an azimuthal nodal line were observed. As discussed above, this arises from the symmetry breaking due to the in-plane hf field. Thus, when applying out-of-plane excitation also purely radial modes were found. Fig. 5.12(b) shows the normal modes (n, 0) up to n = 3 accessible to out-of-plane excitation for a disk with 3 μm diameter.

It is important to note, that on account of the cw excitation the black/white contrast of the obtained images encodes amplitude combined with the phase of the modes. Therefore, from now on amplitude A and phase φ of the local FT data from the simulation are combined by $A\sin(\varphi+\varphi_0)$, in order to directly compare them to data from FMR-

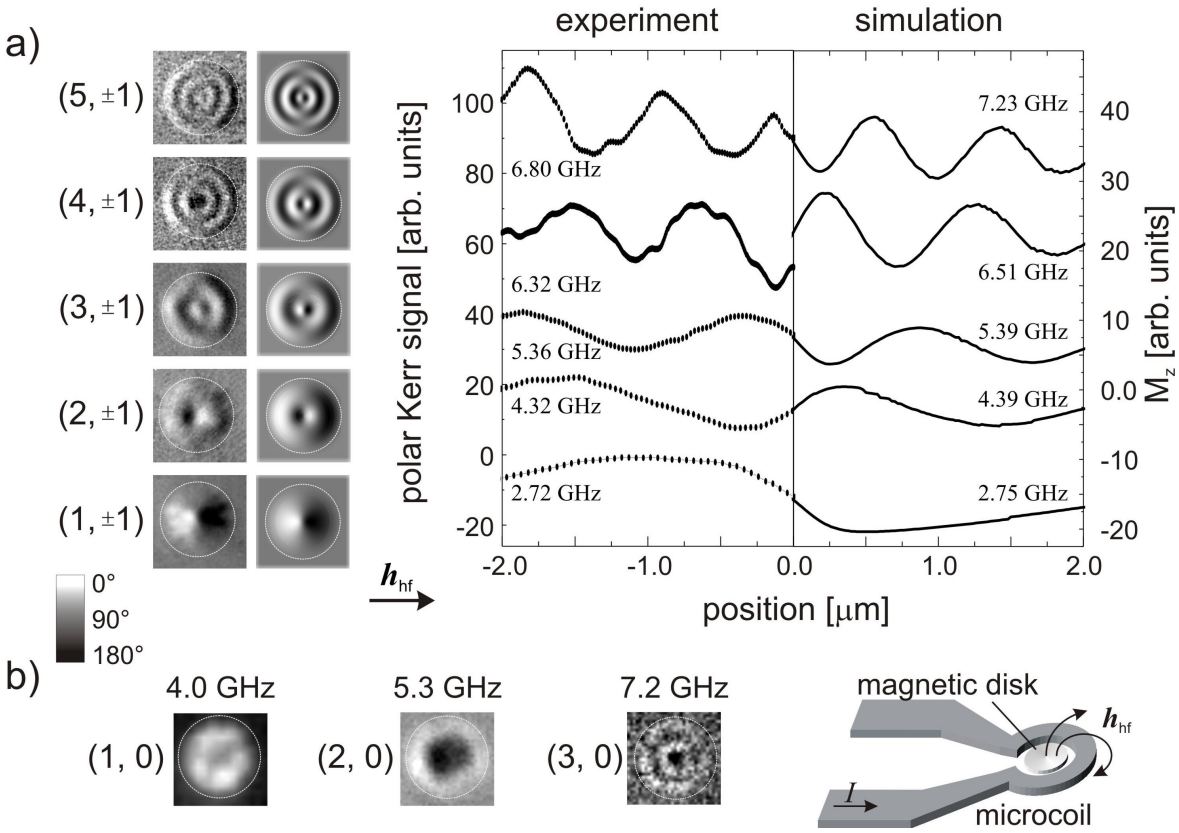

Figure 5.12: *The images show the Kerr rotation and the z-component of* $\boldsymbol{M}$ *obtained from experiment (FMR-SKEM) (left rows in (a)) and simulation (right rows in (a)), respectively. The black/white contrast represents amplitude combined with phase. (a) Applying in-plane excitation only modes with an azimuthal nodal line can be observed as discussed in the text. Line-scans across the disk center parallel to* $\boldsymbol{h}_{\mathrm{hf}}$ *reveal the modal structure obtained from experiment (from -2.0 to 0.0 μm) and from simulation (from 0.0 to 2.0 μm). The modes are labelled by (n, m = 1) according to their number of radial (n) and azimuthal (m) nodes. (b) The normal modes of a disk with 3 μm diameter excited by an out-of-plane hf field. The perpendicular excitation was applied by means of a microcoil surrounding the disk as illustrated on the right.*

SKEM. In the experiment the phase offset φ_0 is adjusted such to obtain maximum contrast. In order to expose the detailed modal structure, line-scans were performed across the disk center parallel to the hf field $\boldsymbol{h}_{\mathrm{hf}}$, which confirm the excellent agreement between the experimental and the simulated data, shown on the right hand side of Fig. 5.12(a).

5.2.4 Modal Spectrum as a Function of an External Bias Field

In this subsection the evolution of the modes as a function of an in-plane bias field applied along the x-direction, perpendicular to the hf field is discussed. First the frequency dependence of mode (1, 1) as measured using inductive VNA-FMR is addressed.

Figure 5.13(a) shows raw data from a VNA-FMR measurement carried out at $\mu_0 H_0 = 15$ mT with a resonance peak at $f = 3.6$ GHz . The field behavior of the fundamental mode (1, 1) accessible by in-plane excitation is depicted in Fig. 5.13(b) (open circles). Starting from its zero field value of 2.7 GHz the modal frequency decreases to about 2.2 GHz at a bias field of ~ 3 mT. It then starts to increase again and approaches the behavior expected from the Kittel equation (solid line in Fig. 5.13(b)), which describes the uniform precession of the magnetic moments throughout the element. In order to account for the aspect ratio of the investigated disks, the Kittel equation 2.33 is corrected for the effective demagnetizing factor $N_{\text{eff}} = N_z - N_x$. Since $N_x \sim N_y$ the resonance frequency reads

$$f = \frac{\mu_0 \gamma}{2\pi} \sqrt{H_0 (H_0 + N_{\text{eff}} M_{\text{S}})}, \tag{5.1}$$

where the gyromagnetic ratio is $\gamma = g \times 97.9$ GHz/T. The aspect ratio of the investigated disks leads to $N_{\text{eff}} = 0.97$ [101]. The g-factor was allowed to vary and was used as a fitting parameter resulting in $g = 2.09$, which is in good agreement with values found in the literature [102]. For the single domain disk (the vortex is expelled at $\mu_0 H_0 \sim 4.0$ mT), this behavior is expected as soon as the spins are mostly aligned along the field direction. In fact, at higher field values, the behavior is well described by the Kittel formula.

From the linewidth Δf (half width at half maximum) of the measured resonance curves one can determine the effective damping parameter by using $\alpha^* = 4\pi \, \Delta f / (\gamma \mu_0 (2H_0 + N_{\text{eff}} M_{\text{S}}))$. Figure 5.14 shows the resulting effective damping parameter extracted from VNA-FMR (dots) and FMR-SKEM (stars) measurements. The clear peak at 2.5 mT observed in the data from VNA-FMR might result from the integrative nature of the technique, since the averaged signal of the whole array of 100 disks is measured.

Because the vortex displacement as a function of bias field might be different for each disk one measures various resonance curves at different frequencies. As a consequence, the linewidth of the resulting resonance curve is much wider than it would be for a single disk. This interpretation is confirmed by the effective damping extracted from FMR-SKEM investigations of a single disk. In contrast, to the VNA-FMR data no clear peak is observed as shown in Fig. 5.14 (stars).

The low signal to noise ratio of the VNA-FMR compared to FMR-SKEM allows only to investigate the fundamental mode (1, 1). In addition in the simulations carried out using the Object Oriented Micromagnetic Framework (OOMMF) [73] and in the optical measurements, the modal spectrum could be investigated in more detail. Consequently as shown in Figure 5.13(b), the frequency scans using FMR-SKEM (stars) as well as the micromagnetic simulations (squares) reveal a second mode appearing in the vortex to single domain transition region. One realizes that in the intermediate region where the vortex has not left the disk yet ($\mu_0 H_0 < 4.0$ mT), the SNR of the inductive VNA-FMR measurements is not sufficient to resolve this second mode found at higher frequencies.

As discussed in detail in Subsection 5.1.1, an in-plane bias field displaces the vortex core transverse to the field. As a result the two large regions with maximum torque now differ in size, as illustrated in Fig. 5.15(c). Since the change of size of the two domains

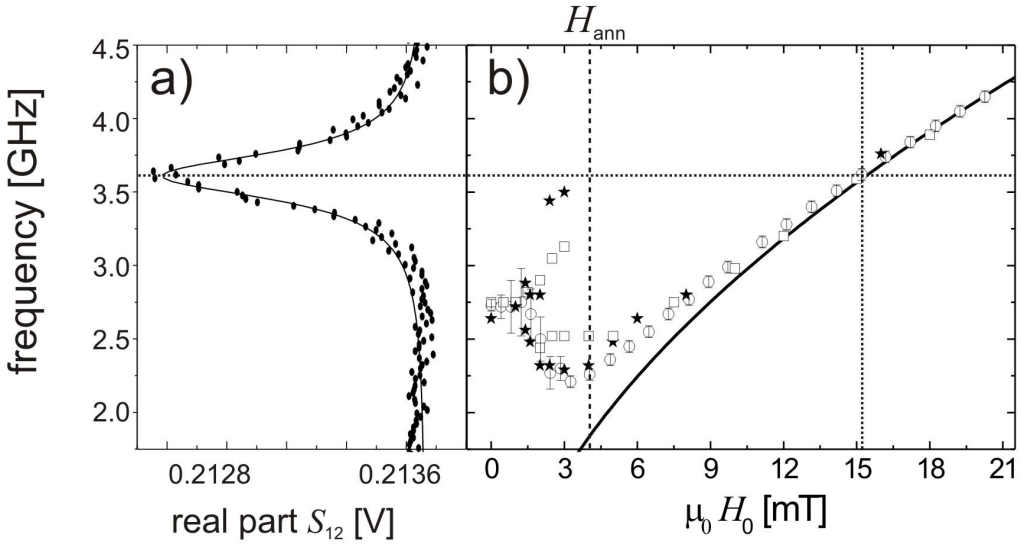

Figure 5.13: *(a) raw data from VNA-FMR measurements (dots) and the fit to a Lorentzian line. (b) the extracted resonance frequency of the fundamental mode (1, 1) as a function of the bias field obtained from VNA-FMR measurements (open circles), micromagnetic simulations carried out using OOMMF (open squares), and frequency sweeps using FMR-SKEM measurements (stars). The fit to the Kittel equation 5.1 is represented by the solid line in (b). The vortex annihilation field H_{ann} is indicated by the vertical dashed line.*

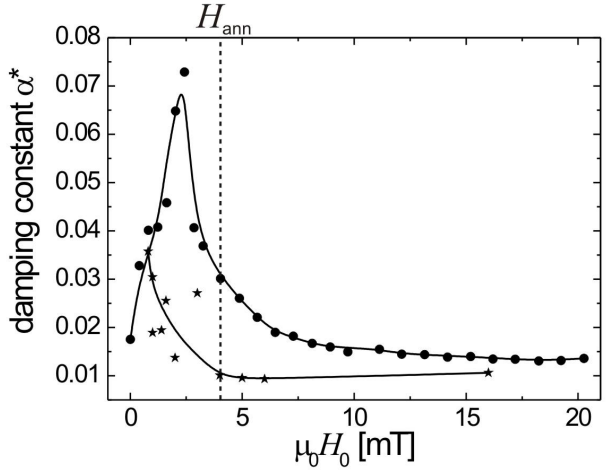

Figure 5.14: *The effective damping parameter α^* extracted from VNA-FMR (dots) and FMR-SKEM (stars) measurements. The lines are guides to the eye. The vortex annihilation field H_{ann} is indicated by the vertical dashed line.*

also alters the width of the corresponding potential wells (cf. Subs. 2.2.3), the modal frequencies immediately differ for the two regions. The frequency of the smaller domain slightly increases and the one of the larger domain slightly decreases. When the vortex is further displaced, the contribution of the exchange energy within the smaller domain dominates and the frequency increase becomes larger. Eventually, the frequency of the

mode in the domain which is 'growing' as a function of bias field, merges with the quasi uniform mode of the single domain configuration. Figure 5.15(a) shows in detail the evolution of the two coexisting modes as a function of the bias field obtained from spatially resolved frequency scans using the resonant Kerr technique (stars). Moreover, images of the modal structure shown in Fig. 5.15(a) confirm the described behavior. Due to forced oscillation inside the domain which is not at resonance with the exciting field, the images in Fig. 5.15(a) show amplitude distribution in both domains. However, as soon as the vortex is expelled from the disk above the annihilation field of $\mu_0 H_0 \sim 4.0$ mT (see Fig. 5.15(d)), the mode located in the 'shrinking' region disappears and the one located in the growing domain shows quasi uniform precession (see image in the lower right corner in Fig. 5.15(a).

Due to the disappearance of the vortex core the element assumes a quasi single domain state and the magnetization is now pointing along the x-direction leading to magnetic poles at the edges of the disk. The resulting stray field in turn locally softens the effective internal field of the system. This effect has first been observed by Hiebert et al. [5]. Fig. 5.16 depicts the resulting internal effective field for the entire disk (a) and as a line-scan across the disk center parallel to the external field (b) for $\mu_0 H_0 = 20$ mT. Due to the localized inhomogeneity of the internal field near the edges two regions inside the disk can be distinguished with respect to the effective field: a quasi homogeneous region around the center of the disk and a strongly inhomogeneous region in the vicinity of the disk edges.

First the homogeneous region near the disk center is emphasized. The modal spectrum of this area at $\mu_0 H_0 = 5$ mT was investigated by means of spatially resolved FMR-

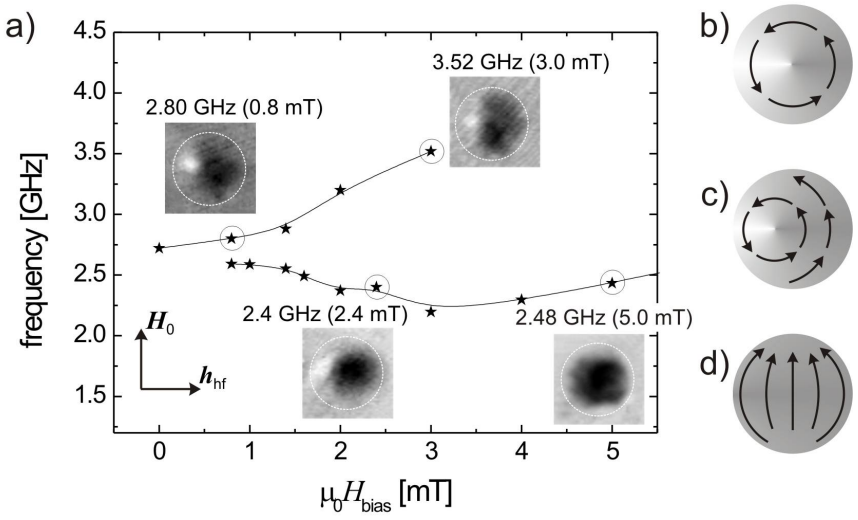

Figure 5.15: *The transition region from vortex to single domain state where a coexistence of two modes with different field behavior was observed. (a) data points were obtained from local frequency scans using FMR-SKEM. The images of the modal structure recorded by means of FMR-SKEM correspond to the encircled data points. Illustrations on the right show the magnetization configuration at zero bias field (b), at* $0 < \mu_0 H_0 < 4$ *mT (c), and at* $\mu_0 H_0 \geq 4$ *mT (d).*

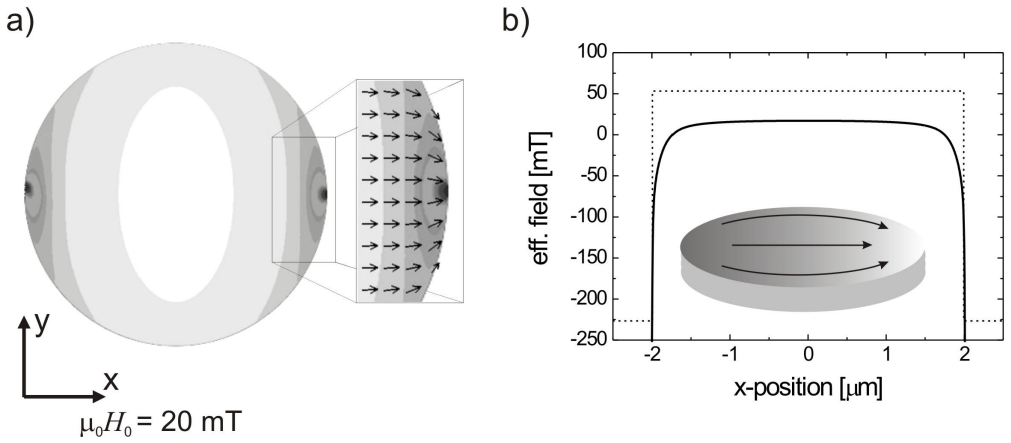

Figure 5.16: *(a) the effective internal field of the entire disk encoded by a black/white contrast at $\mu_0 H_0 = 20$ mT. In order to relate the static magnetization configuration $\boldsymbol{M}$ (represented by the arrows) to the effective field a small area of the edge region is enlarged. (b) a line-scan along the external bias field reveals the field profile as a function of the position. All data was extracted from micromagnetic simulation.*

SKEM measurements and micromagnetic simulations (see Fig. 5.17(a) and upper part of (b)). At 2.48 GHz (2.0 GHz) in the experimental (simulated) data a mode was observed which roughly spreads throughout the entire region of quasi homogeneous internal field (cf. Fig. 5.16(a)). At $f = 5.28$ GHz (5.2 GHz) and 7.12 GHz (7.2 GHz) modes with four and eight nodal lines, respectively, parallel to the applied field $\boldsymbol{H}_0$ were detected exemplarily in experiment (simulation). Consequently, these modes are quantized transverse to the bias field and to the static magnetization. In addition, the mode frequency increases with increasing node number, hence these modes are reminiscent of Damon Eshbach like modes (cf. Subs. 2.2.3). Note that also the modes with 2 and 6 nodal lines should be observable in the experiment. However, with the SNR of the FMR-SKEM setup these modes could not be detected. In fact, micro-focus BLS should be allow to reveal also these modes on account of its higher SNR [24, 31].
The modes observed in the simulations at $\mu_0 H_0 = 5$ mT are disturbed with respect to the orientation of the their nodal lines, see upper part of Fig. 5.17(b). However, simulations carried out at $\mu_0 H_0 = 80$ mT (see lower part of Fig. 5.17(b)) show the same modes without any deviation. The differences between the corresponding static magnetization configurations are depicted on the right hand side of Fig. 5.17(b). While the disk is magnetized quasi uniformly at $\mu_0 H_0 = 80$ mT, the magnetization configuration at $\mu_0 H_0 = 5$ mT reveals considerable deviations of the magnetic moments from the direction of the external field. The disturbances found in the modal pattern at $\mu_0 H_0 = 5$ mT are therefore attributed to arise from the nonhomogeneous magnetization configuration. The mode structure obtained by the experiment do not show these disturbances even at such a low bias field. This might come from uncertainties of the thickness as well as surface roughness of the real disk. Since both phenomena could reduce the effective stray field, the internal field and in turn also the magnetization configuration would be more homogeneous.
Compared to the higher order modes, the fundamental mode shows less accordance

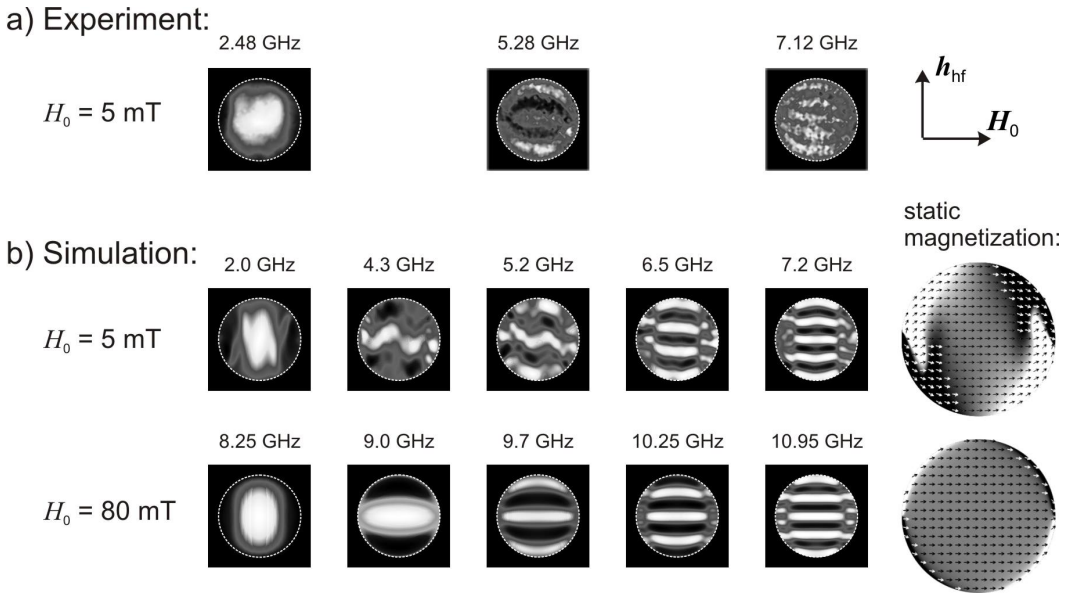

Figure 5.17: *Spatially resolved images from FMR-SKEM measurements (a) and from micromagnetic simulations (b) at $\mu_0 H_0 = 5.0$ mT and 80.0 mT. Pulsed excitation was employed for the simulations. The corresponding static magnetization configurations (arrows) and the y-components (encoded by the black/white contrast) obtained from micromagnetic simulations are shown on the right hand side of (b).*

in terms of the resonance frequency between experiment and simulation (2.48 GHz and 2.0 GHz). This may also come from a lowering of the internal field due to the demagnetizing field which might be more effective for the simulated disk as discussed above. In fact, a comparison of the modal spectra from simulation at $\mu_0 H_0 = 5$ mT and 80 mT (see Fig. 5.17(b)) reveals that the slope of the dispersion relation decreases with increasing internal field. This might be understood in the following way: the effective field determines the 'stiffness' of the magnetic system. Thus, the cone angle of the magnetic precession decreases when raising the effective field, which in turn causes a decrease of the dynamic magnetization component $\boldsymbol{m}$. For this reason the effect, responsible for the increase of the mode frequency with rising node number in Damon Eshbach like modes discussed in Subsection 2.2.3 is reduced. As discussed above, the effective field inside the real sample seems to be raised regarding the simulated disk. Therefore, the slope of the dispersion relation of the measured disk should be lower compared to the simulated disk. This behavior can indeed be observed in Figures 5.17(a) and top row in (b): While a poor accordance in frequency is found for the small wave vector mode (mode 1: $f = 2.48$ GHz (experiment) and $f = 2.0$ GHz (simulation)), the frequencies from experiment and simulation accord very well for higher order modes: mode 3: $f = 5.28$ GHz (exp.) and $f = 5.2$ GHz (sim.); mode 5: $f = 7.12$ GHz (exp.) and $f = 7.2$ GHz (sim.).

Now the edge region showing a strong inhomogeneous internal field as depicted in Fig. 5.16 is focused. Spatially resolved images from FMR-SKEM measurements show that in addition to the modes in the center, modes are found localized at the disk edges

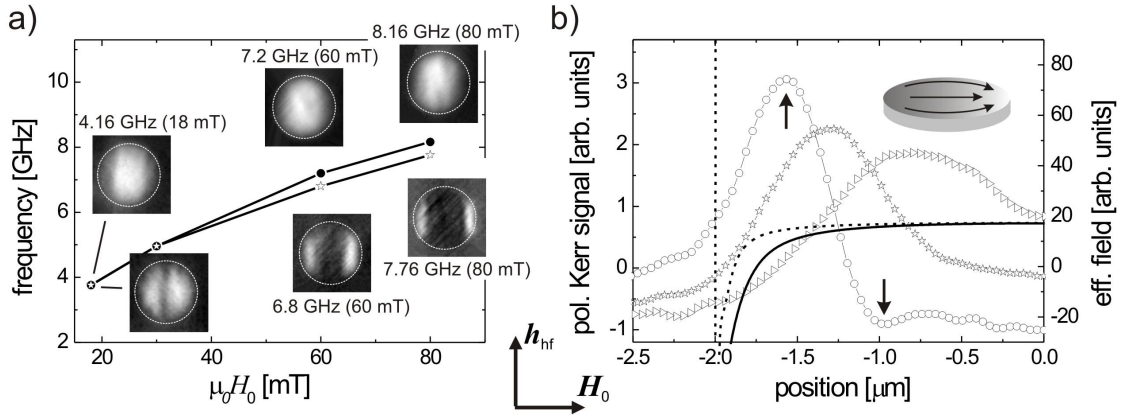

Figure 5.18: *(a) the quasi uniform (dots) and the localized edge modes (open stars) as a function of the bias field obtained from frequency scans using FMR-SKEM. Corresponding images disclose the structure of the different modes. While the center and the edge mode are found at the same frequency below 30 mT, the different dispersion relations lead to a splitting in frequency above 60 mT. (b) horizontal line-scans for the edge modes across the center of the disk for 4.16 GHz (triangles), 6.8 GHz (stars), and 7.76 GHz (dots) are shown for one half of the disk. The effective fields at $\mu_0 H_0 = 20$ mT and 80 mT obtained from micromagnetic simulations are represented by the solid and dashed curve, respectively. The vertical dotted line marks the left boundary of the disk. The arrows indicate the two antinodes found in the edge mode at $\mu_0 H_0 = 80$ mT.*

(see Fig. 5.18(a)). Figure 5.18(a) shows both, the resonance frequencies and the modal structures as a function of the external bias field. The data points were obtained from spatially resolved resonance Kerr microscopy (FMR-SKEM). While the upper images depict the quasi uniform fundamental mode of the center region, the lower images reveal another mode localized in the edge region of the disk. Its spatial distribution is reminiscent of localized edge modes as described in [10, 13, 14]. The inhomogeneous internal field within the disk leads to a 'potential well' for magnetic excitations [18, 103] at the edges. In the experiment the quasi uniform mode in the disk center and the localized edge mode are observed at the same frequency up to an external bias field of 30 mT. Though, the two modes cannot be separated in frequency, the small deviation between their resonance frequencies leads to different phase lags with respect to the excitation. These phase lags allow to detect their maximum amplitudes separately at different phases (see images at $\mu_0 H_0 = 18$ mT in Fig. 5.18(a)). When increasing the bias field, the different dispersion relations increase the frequency splitting of the two modes. This effect can be observed experimentally above $\mu_0 H_0 = 60$ mT (see Fig. 5.18(a)). At the maximum bias field of 80 mT applied in the experiment the frequency splitting was found to be $\Delta f = 400$ MHz.

In order to investigate the spatial distribution of the edge modes as a function of the external bias field line-scans were performed across the disk center parallel to the bias field (see Fig. 5.18(b)). Furthermore, the effective field profile of the disk is plotted in Fig. 5.18(b) for $\mu_0 H_0 = 20$ mT (solid line) and $\mu_0 H_0 = 80$ mT (dashed line). The amplitude distribution of the edge localized modes was found to shift toward the disk

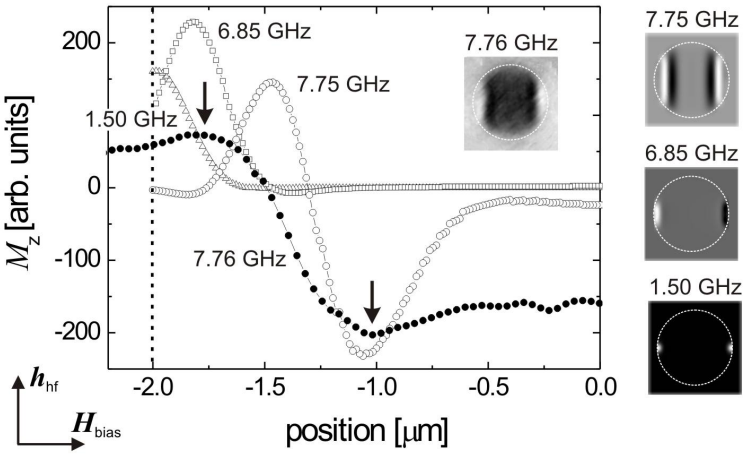

Figure 5.19: *Images and line-scans from experiment (inset and solid dots) and from simulation (images on the right and open symbols) depict the amplitude distribution of the localized edge modes at $\mu_0 H_0 = 80$ mT. The line-scans are performed across the center of the disk parallel to the bias field. Open symbols showing the amplitude distribution for $f = 1.5$ GHz (triangles), $f = 6.85$ GHz (squares), and $f = 7.75$ GHz (dots) represent simulation. The two antinodes which can be clearly seen in the data from simulation ($f = 7.75$ GHz) are also indicated in the data from experiment (arrows). The vertical dotted lines mark the left boundary of the disk.*

boundaries as the bias field increases, which is caused by a corresponding decrease of the inhomogeneous edge region [18, 104].
A comparison to micromagnetic simulations carried out at $\mu_0 H_0 = 80$ mT reveals three quantized modes localized in the edge region (see Fig. 5.19). This is expected, since also higher order edge localized modes are expected to appear when the width of the 'well' decreases [103]. However, in the experiment no additional nodes for the edge modes could be detected below $\mu_0 H_0 = 80$ mT. In fact, for the edge mode at 80 mT two antinodes are observed at position -1.0 μm and -1.6 μm (see arrows in Fig. 5.18(b)). By further investigating the structure of the edge mode, at $\mu_0 H_0 = 80$ mT additional evidence for a two antinode mode was found. The arrows in Fig. 5.19 indicate the two antinodes observed in the experimental data at position -1.1 μm and -1.8 μm. As a consequence, the edge mode at $f = 7.76$ GHz which was found in the experiment likely corresponds to a higher order mode in agreement with results from the simulated data.

These edge localized modes have already been found previously in small stripe elements [10, 13, 18, 103]. However, as indicated in Figure 5.17, the transverse quantization of the DE-like modes was observed not only in the center region but also in the edge region. This finding was confirmed by recording the resonant modal pattern at $\mu_0 H_0 = 20$ mT as shown in Fig. 5.20 both for experiment (left) and simulation (right). It is important to note that the simulation shown in Fig. 5.20 was carried out with the LLG code by applying a continuous wave excitation. When employing a short field pulse the mode localized at the disk edges could not be observed clearly (cf. Fig. 5.17(b)). The reason for this might be the interaction of the modes with other normal modes of the disk.

Since with pulsed excitation, all modes are triggered simultaneously, the formation of the edge modes could be disturbed by the other dominating modes. When resonantly exciting the disk by means of a continuous wave hf field, one observes a standing wave located around the center with a wave vector of $k_{\parallel}^{\text{center}} = 2\,\pi/\lambda = 7.1 \times 10^6 \text{m}^{-1}$ (see solid dots in Fig. 5.20). At the same frequency a standing wave is found near the edges of the disk (with respect to the direction of $\boldsymbol{M}$) with a wave vector of $k_{\parallel}^{\text{edge}} = 8.2 \times 10^6 \text{m}^{-1}$ (see open dots in Fig. 5.20). The corresponding internal field is depicted by the black/white contrast in Fig. 5.16(a). Note that the wave vector does not change continuously with the increasing curvature of the disk boundary. Instead, two distinct regions – at the center and the edge of the disk – with approximately constant wave numbers are found. These two regions are reminiscent of the two different regions responsible for the localized edge modes observed parallel to $\boldsymbol{M}$ (see Figs. 5.16(b) and 5.18). Although, the Damon Eshbach modes are quantized transversely to $\boldsymbol{M}$, the field parallel to the magnetization determines the corresponding wave numbers. In addition, as observed for the localized edge modes (see Fig. 5.18), despite of the strong inhomogeneity found in the internal field the spatial distribution of the modes near the edges is rather uniform (see images in Fig. 5.20). Although, the quantization of the edge modes could not be observed clearly in the simulation when applying pulsed excitation, the local Fourier transform of the time domain data reveals the quantized modes in the center region. Consequently, their wave numbers could be extracted from a pulsed simulation and are shown in Fig. 5.21 (dots). A comparison of the obtained dispersion behavior to the theoretically derived relation shown in Fig. 2.4, reveals the observed modes to be purely dipole dominated. Fitting the data points from simulation to the

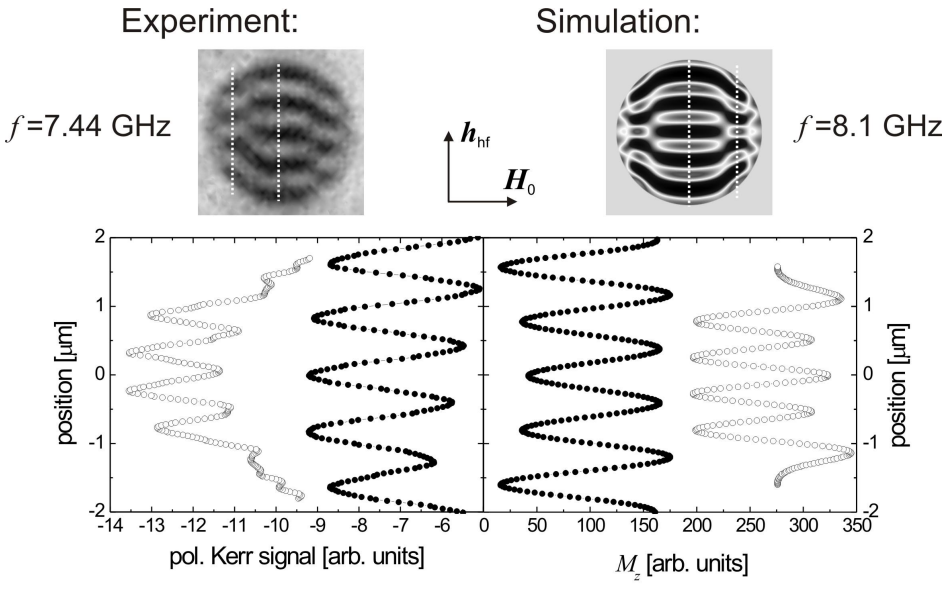

Figure 5.20: *The Damon Eshbach like mode obtained from FMR-SKEM (left - f = 7.44 GHz) and simulation (right - f = 8.1 GHz) at $\mu_0 H_0 = 20$ mT. Line-scans performed along the vertical dotted lines indicated in the images, expose the dependence of the excitation wavelength on the position. The simulation was performed with sinusoidal excitation.*

dispersion relation of the Damon Eshbach mode (Eq. 2.40) with the disk thickness as the only free parameter, results in $t = 20.5$ nm. As for the fit to the Kittel equation 5.1, the aspect ratio of the disk was accounted for by the effective demagnetizing factor $N_{\text{eff}} = 0.97$. The fitted curve is represented by the solid line in Fig. 5.21 and shows excellent agreement with simulations for both data from pulsed (dots) and continuous wave (square) excitation. The saturation magnetization and the effective internal field were determined by SQUID measurements and micromagnetic simulations, respectively ($\mu_0 M_{\text{S}} = 1$ T and $\mu_0 H_{\text{eff}} = 17$ mT). Using the same parameters and only assuming a weaker internal field ($\mu_0 H_{\text{eff}} = 6$ mT), one obtains a dispersion relation from Eq. 2.40, which traverses the data point obtained from the continuous wave excitation for the mode in the edge region (see dashed line and square in Fig. 5.21). Indeed, due to the weaker effective field inside the edge region, the corresponding dispersion relation is shifted to lower frequencies with respect to the dispersion relation of the center region. Therefore the modes in the two regions have different wave numbers as observed in Figure 5.20, even though they are excited at the same resonance frequency as illustrated by the dotted horizontal and vertical lines in Figure 5.21. This effect might be employed in order to determine the effective internal field from measuring the wave vectors $k_{\parallel}$.

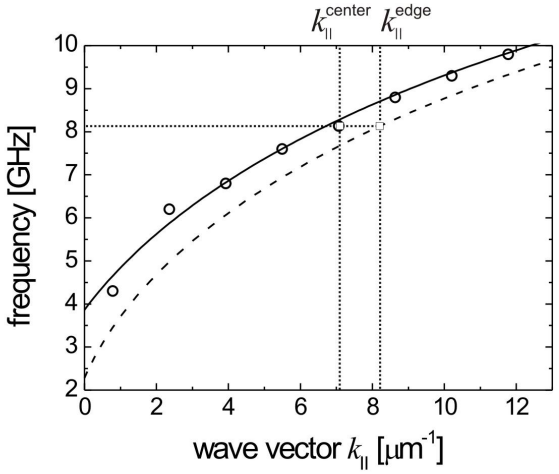

Figure 5.21: *The frequencies of the Damon Eshbach modes from simulation (symbols) and from Eq. 2.40 (lines). Data points from simulation with continuous wave and pulse excitation are represented by squares and dots, respectively. The theoretically derived dispersion relations are obtained by assuming different effective fields as described in the text. As a result different wave numbers ($k_{\parallel}^{\text{center}}$ and $k_{\parallel}^{\text{edge}}$) are observed in the different regions at the same excitation frequency, indicated by the horizontal and vertical dotted lines.*

6 Confined Magnetic Structures II – Cylindrical Rings

The investigation of cylindrical disks presented in the preceding chapter, revealed a considerable dependence of the resonant modes on the underlying magnetization configuration and the geometry of the system. In particular the effect of removing the vortex core on the normal mode spectrum has been discussed. By removing the material of the disk center, the perpendicular magnetization component of the vortex core is taken away on the one hand, but on the other hand since a ring structure is obtained, an additional parameter to tune the properties of the sample is introduced via the ring width. In case of the flux-closure configuration the ring geometry is totally free of stray field on account of the absence of the vortex core. For this reason ring structures have recently attracted much attention, though so far, primarily concerning their static properties [32–36]. First dynamic experiments on ring structures were carried out by Giesen et al. [105, 106] using vector network analyzer ferromagnetic resonance (cf. Subs. 3.1.2). This novel inductive technique gives an insight into the modal spectrum averaged over many rings with respect to the frequency and the effective damping of the various magnetic modes. However, the VNA-FMR technique does not reveal the spatial structure of the modes, which is essential for a detailed understanding. Zhu et al. [22] carried out the first experiments on ring structures using time resolved scanning Kerr microscopy (cf. Subs. 3.2.2) by exciting the rings with a field pulse and then observing the time evolution of the magnetization. This technique probes a superposition of several eigenmodes but does not expose the nature of the separate eigenmodes. For a more thorough comprehension of the individual eigenmodes, Co rings were studied by means of both VNA-FMR and ferromagnetic resonance scanning Kerr microscopy (cf. Subs. 3.2.3). The corresponding results are presented and discussed in the first part of this chapter. Moreover, dynamic dipolar coupling between the rings in an array was investigated and is addressed in the second part. The corresponding results are again compared to micromagnetic simulations.

6.1 Static Characterization

An array of 2×350 Co rings was fabricated using electron beam lithography and a lift-off technique [107] directly on top of the signal line in direct contact with the coplanar waveguide (signal line width $w = 10$ μm). For 1 mW output power from the VNA, the transverse hf field amplitude is found by employing Eq. A.2 to be 0.19 mT[1]. The precise hf field profile is given in Appendix A.2. Details concerning the fabrication

[1] An attenuation of -2 dB from the hf signal source (VNA) to the sample was assumed

of the rings can be found in Appendix A.4. A scanning electron microscopy image of rings with different widths on top of a waveguide is depicted in Figure 6.1(a) and demonstrates the well defined geometry achieved by this procedure. The thickness of the investigated Co rings was 32 nm, their inner diameter was 1.7 μm, and their width was 500 nm. An inter-ring spacing of 100 nm along the waveguide and 900 nm in transverse direction was chosen. Figure 6.1(b) shows a picture of the investigated rings added by their dimensions, acquired with the SKEM setup by measuring the reflectivity of the laser beam as a function of its position on the sample.

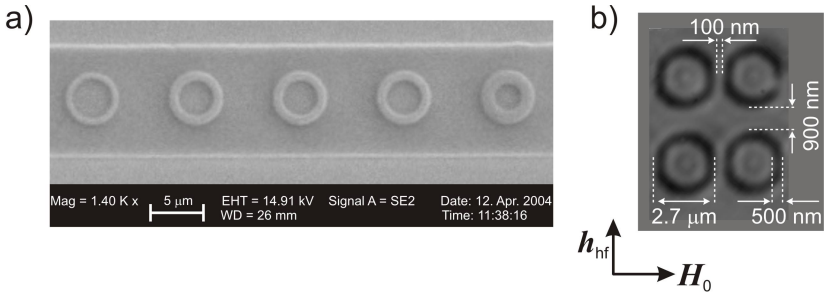

Figure 6.1: *(a) Co ring elements with different widths on top of a waveguide, imaged by scanning electron microscopy. The rings were fabricated by means of electron beam lithography and lift-off process as described in Appendix A.4. (b) the geometry and distances of the investigated rings. The image was obtained from locally measuring the reflectivity of the laser beam using the SKEM setup.*

Earlier publications [32, 36, 108] already demonstrated that in contrast to disks, ring shaped elements can exhibit two distinct remanent magnetic states, namely the vortex and the so called 'onion' state. In addition, to the flux-closure vortex state (see illustration in Fig. 6.2), the onion state is characterized by two head-to-head domain walls as illustrated by the sketches on the left and top right hand side in Fig. 6.2.
The geometrical parameters of the rings (inner diameter, width, and thickness) were adjusted in order to ensure a two step transition [32, 108], namely onion to vortex to reverse onion. The onion and vortex states involved in the observed double switching process are remanent states of the system (see Fig. 6.2). Thus, the magnetization configuration shows hysteretic behavior as can be seen in the static magneto-optical Kerr effect loops, shown in Fig. 6.2. While the remanent onion state can be obtained reversibly from saturation, the vortex state is accessible by applying a static field opposite to the onion configuration of approximately 26 mT. As displayed by the minor loop (see inset in Fig. 6.2), when subsequently decreasing the field to zero, the vortex configuration is conserved. Consequently, both remanent states were accessible by applying in-plane magnetic fields.
All micromagnetic simulations reported in this chapter were carried out using the LLG Micromagnetics Simulator [72]. Edge corrections were applied both to the inner and the outer boundary of the ring. In order to compare experimental to simulated data, the time domain output from simulations was again transformed into the frequency domain by performing the phase-sensitive local Fourier transform procedure described in Subsection 3.3. Subsequently, the data was filtered by a 100 nm two-dimensional

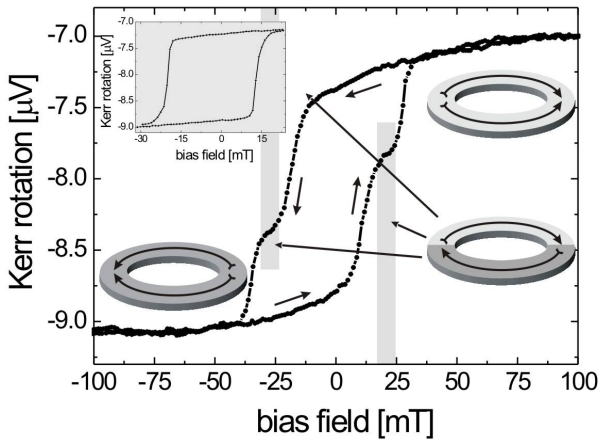

Figure 6.2: *Static hysteresis loops of the rings show a double switching process from onion to vortex to reverse onion. The field was applied along the small inter-ring spacing. Sketches illustrate the corresponding magnetization configurations. The shaded region and the minor loop shown in the inset represent the vortex configuration.*

Gaussian window in order to compare it to the experimental results.

6.2 Dynamic Characterization of the Double Switching Process

First, inductive VNA-FMR measurements were carried out in order to obtain the frequencies of the eigenmodes as a function of the external bias field. Fig. 6.3(b) shows the absorption spectrum from a VNA-FMR measurement with 5 distinct resonance lines at different frequencies measured at $\mu_0 H_0 = 80$ mT applied along the waveguide. The frequencies of the modes were extracted by fitting the peaks to Lorentzian lines. By performing this procedure as a function of the bias field one obtains Fig. 6.3(a), which shows the absorption spectrum of the rings for an up-sweep of the applied field (sweeping from negative to positive bias fields). Coming from negative bias fields one single mode (mode 1) remains when approaching zero field at a frequency of $f = 12.9$ GHz. Increasing the field, the rings switch into the vortex state at $\mu_0 H_0 = 20$ mT which causes a splitting of mode 1 into two branches with opposite slope. A detailed description of this process is given later in this section. At $\mu_0 H_0 = 40$ mT and $f = 14$ GHz a second mode (mode 2) appears below mode 1. Proceeding the up sweep, a third mode (mode 3) at $\mu_0 H_0 = 61$ mT and $f = 14.1$ GHz, and a fourth one (mode 4) at $\mu_0 H_0 = 80$ mT and $f = 14.1$ GHz is found. Additionally, a mode lying clearly lower in frequency (mode 5) appears at $\mu_0 H_0 = 51$ mT and $f = 6.2$ GHz.
The double switching process [32] which was observed in the static MOKE loops in Fig. 6.2, is responsible for the asymmetric bias field behavior of mode 1 (see Fig. 6.3) and thus is found to be evident also in the dynamic response of the rings. In order to further clarify this behavior the resonance frequency (solid dots) and the intensity

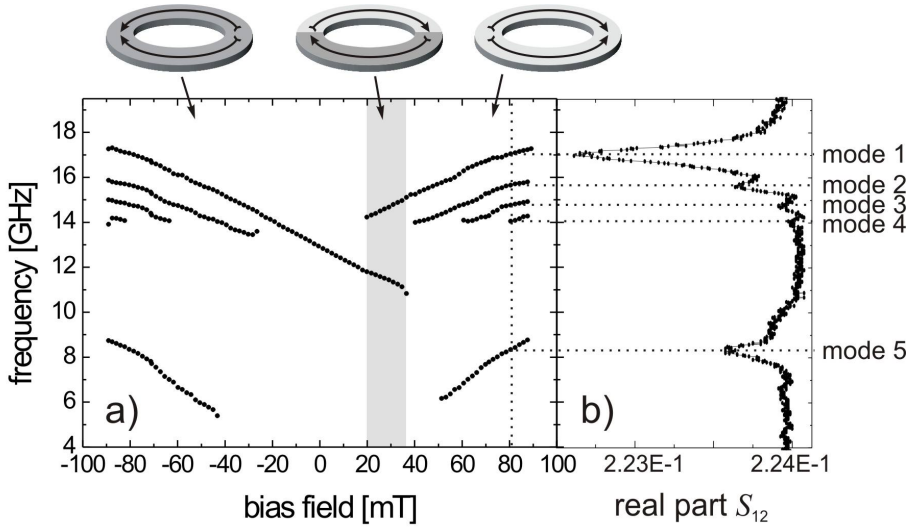

Figure 6.3: *(a) frequencies (dots) of the various modes as a function of the magnetic bias field for an up-sweep obtained by inductive* VNA-FMR *measurements. The shaded field region corresponds to the vortex state. The schematic drawings on top illustrate the corresponding onion and vortex configuration. Plot (b) shows raw data with 5 distinct resonance lines at a bias field of* $\mu_0 H_0 = 80$ *mT. The resonance peaks discussed in the text are labeled from 1 to 5.*

(open symbols) of the absorption peaks of mode 1 are presented in Figure 6.4(a). Additionally, the modal structures obtained from FMR-SKEM and micromagnetic simulations are depicted in Fig. 6.4(c)-(g) for selected bias field values during the up-sweep. Approaching zero field, the fundamental mode of the remanent onion state was observed as shown in Fig. 6.4(c) ($f = 12.8$ GHz). Since in the onion state both 'arms' of the ring are magnetized parallel, the magnetization in the two arms precesses in phase. Therefore, the dynamic response shows the same symmetry as the onion configuration relative to the x-axis (along the waveguide). By increasing the bias field up to $\mu_0 H_0 = 29$ mT the rings switch into the vortex state and an additional branch appears in the resonance spectrum of (a) and (b). Now the two arms of the ring are magnetized antiparallel, so that the two regions precess with a phase lag of π, as it was found in the vortex state of the disks (cf. Subs. 5.2.3). In agreement with the VNA-FMR measurements two resonances at different frequencies ($f = 14.6$ GHz and $f = 11.6$ GHz) were found by FMR-SKEM (see Fig. 6.4(f) and (g)). The spatially resolved images show that the two modes are located in opposite arms of the rings. This behavior arises due to the influence of the bias field on the effective field inside the rings. In the arm magnetized parallel to the field, the effective field is raised whereas in the arm magnetized antiparallel it is lowered by the external field causing higher and lower resonance frequencies, respectively. Moreover, the intensity of the left branch in Fig. 6.4(b) suffers a significant drop when the second branch appears, since the amount of magnetic moments which are in resonance is now limited to one arm of the ring. Sequentially, further increasing the bias field decreases both the intensity and the frequency of the fundamental left branch, whereas the intensity and the frequency

of the right branch increases.
Reducing the field from 29 mT back to zero bias field (minor loop), both regions show resonance at the same frequency as shown in Fig. 6.4(d) ($f = 12.9$ GHz) which corresponds to the fundamental mode of the remanent vortex configuration. Data obtained from micromagnetic simulations (Fig. 6.4(c) and (d) labelled by S) confirm this interpretation of the experimental results. When increasing the bias field up to $\mu_0 H_0 = 50$ mT, the vortex to reverse onion transition occurs, so that the left resonance branch disappears. Thus, the intensity of the right branch in (b) increases and the fundamental modes in the two arms of the ring are found at the same frequencies (see Fig. 6.4(e)). A similar bias field behavior of ring elements was already observed by Giesen et al. [105].
The intensity of the absorption peaks reaches a maximum at approximately $\mu_0 H_0 =$

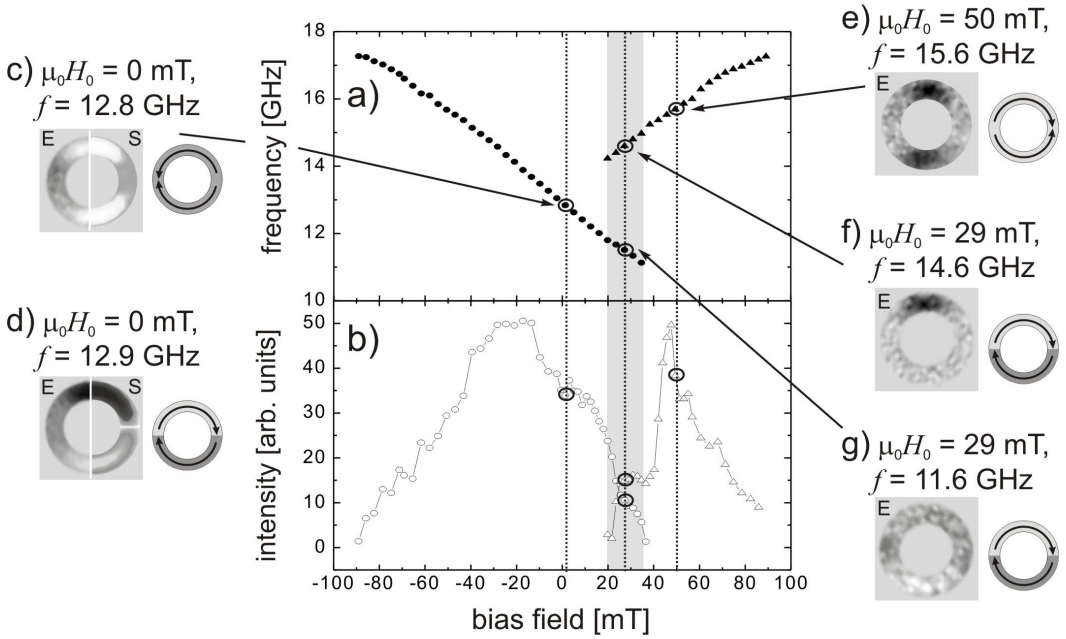

Figure 6.4: *The up-sweep regarding mode 1. The images show the local Kerr rotation obtained from experimental* FMR-SKEM *(labeled* E*) and micromagnetic simulations (labeled* S*). Black and white represent the amplitude and have a phase difference of π. (a) depicts the resonance frequency (solid symbols) of mode 1 (cf. Fig. 6.3(a)). (b) the intensities of the left (open dots) and right branch (open triangles) of mode 1. The shaded field region corresponds to the vortex state. Images (c) and (d) show the fundamental mode of the remanent onion and vortex state, respectively. Images (f) and (g) are recorded at $\mu_0 H_0 = 29$ mT and reveal that the two resonance branches in (a) and (b) appear due to the vortex configuration with the parallel and antiparallel magnetized arms of the ring regarding the bias field. (e) at $\mu_0 H_0 = 50$ mT both arms of the ring are in resonance at the same frequency, which indicates the reverse onion configuration. The schematic drawings illustrate the corresponding static magnetization configuration. The intensity behavior of the two branches in (b) gives additional evidence of the observed double switching process.*

−17 mT and 48 mT for the left and right branch, respectively. Thus, the asymmetry caused by the double switching process seems to be reflected also in this feature of the dynamic response. However, the reason for why the intensities decrease for high external bias fields shown in Fig. 6.4(b) is not yet clarified. Since the peaks of the left and right branch are shifted with respect to zero field, the observed intensity behavior, in fact appears to depend on the static magnetization configuration. Note that even though the stiffness of the system is expected to increase with the in-plane external field, the intensity should not decrease, as the VNA-FMR technique is sensitive to the absorbed power.

6.3 Modal Spectrum at 80 mT Bias Field

In order to reveal the structure of the additional modes found by VNA-FMR at bias fields above $\mu_0 H_0 = 40$ mT, FMR-SKEM measurements were carried out at $\mu_0 H_0 = 80$ mT. The corresponding images (labelled E) are shown together with data obtained from micromagnetic simulations (labelled S) in Fig. 6.5 (mode 1 - mode 5). In order to extract the modal structure from the images as a function of the azimuthal angle φ, angular scans averaged over the hole width of the ring were performed for the various modes. The experimental and simulated data are shown for $0° \leq \varphi \leq 180°$ and $180° \leq \varphi \leq 360°$, respectively. For all modes the symmetry of the underlying onion state is retained, meaning that the modes are symmetric with respect to the horizontal axis (parallel to the bias field). As discussed in Subsection 2.2.3 the modes are terminated at the boundaries of the 'potential well'. Therefore, the number of nodes is assigned by accounting for each termination of the modes at the boundary by a 1/2 node. According to this convention mode 1 has one azimuthal node. Note that for mode 1 to 4 when increasing the mode number, the number of nodal lines always increases by two for the next higher mode. This implies that these modes show an odd number of nodes only. It was possible to detect modes with an even number of nodes neither in the experiment nor in the simulation. This is exactly what one can expect from an uniform excitation geometry. The quasi uniform magnetization within the arms of the rings is excited by an uniform hf field. In this case the net dynamic magnetization vanishes for an even number of nodes, which in turn causes also the net torque applied to the magnetization by the exciting field to vanish. As a consequence, the selection rule for excitation implies that the number of half wavelengths should be odd, as has already been stated by Kittel [109]. Indeed, the modes with an even number of nodes should be detectable by applying a small symmetry breaking field or in Brillouin light scattering experiments, which offer the possibility to study the thermally activated spin wave spectrum.
The discrepancy between experiment and simulation in the frequency of less than 9 % probably arises from the uncertainty concerning the sample thickness.
In the following wave numbers $k_\varphi = 2\,\pi/\lambda$ are assigned for the various modes extracted[2] from the angular scans in Fig. 6.5. The resulting dispersion relations for the

[2]The termination of the modes was determined at the point where the amplitude of the outer antinode has decreased to 10% of its initial value.

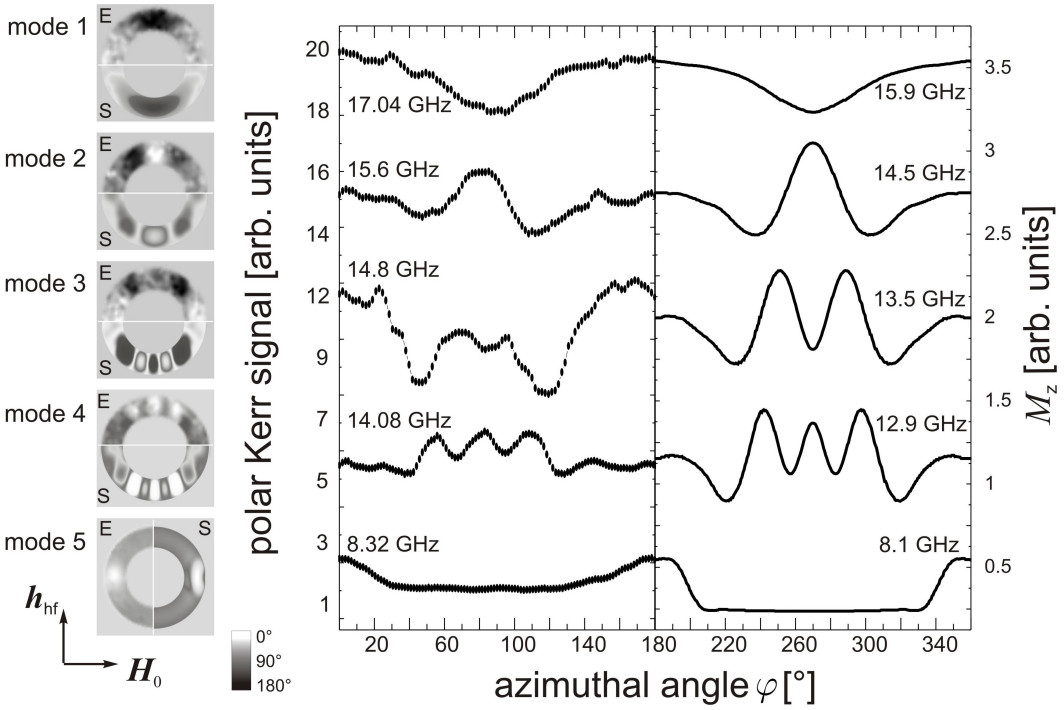

Figure 6.5: *The various modes at $\mu_0 H_0 = 80\ mT$. The images show the local Kerr rotation obtained from experimental FMR-SKEM investigations (labelled* E*) together with data from micromagnetic simulations (labelled* S*). Angular scans along the ring perimeter obtained from experiment ($0° \leq \varphi \leq 180°$) and from simulation ($180° \leq \varphi \leq 360°$) provide the Kerr signal as a function of the azimuthal angle φ.*

experimental and the simulated data depicted in Fig. 6.6 show negative slopes, i.e. the frequency decreases with increasing wave number. This is a consequence of the orientation of the wave vectors $\boldsymbol{k}$ being approximately parallel to the magnetization $\boldsymbol{M}$. Hence, these modes are reminiscent of magnetostatic backward volume waves (cf. Subs. 2.2.3). For the experimentally determined wave-numbers an error of $\sim 10\%$ arises from uncertainties when extracting the wavelengths. The resonance frequency of the modes could be determined experimentally with an error of $\sim 1.5\%$.
In order to confirm the observed frequency behavior, the frequencies can be derived from the dispersion relation of the MSBVW (cf. Eq. 2.41). For simplicity, two different approximations are attended. In a first approach the dispersion is calculated for an infinite film with 32 nm thickness. The resulting curve is represented by the dashed line in Fig. 6.6(a) and shows, except for mode 1, poor agreement with the experimental and simulated data. Therefore, a refined model proposed by Giesen et al. [110] was employed, where the arms of the ring are approximated by uniformly magnetized rectangular rods, as shown in Fig. 6.6(b). The geometry of the rod is accounted for by introducing the demagnetizing factors N_i (cf. Eq. 2.15) into the dispersion relation 2.41:

$$\omega^2_{\mathrm{MSBVW}} := \omega_r \left[\omega_r + \omega_M \left(\frac{1 - e^{-k_\parallel t}}{k_\parallel t} \right) \right], \tag{6.1}$$

where ω_r is given by Eq. 2.33. Since the rod shape considerably deviates from an ellipsoid, the demagnetizing field is a function of the position inside the sample. However, in this simple model the position dependence was neglected and the averaged demagnetizing factors were determined by means of the LLG code [72] to be $N_x = 0.035$, $N_y = 0.079$, and $N_z = 0.886$. When fitting the obtained dispersion relation to the experimental data, with the saturation magnetization as free parameter, one obtains $\mu_0 M_S = 1.6$ T, which is significantly reduced with respect to the value ($\mu_0 M_S = 1.79$ T) reported in literature [111]. This deviation might arise from the fact, that this very simple model does not account for the curvature of the ring structure. The demagnetizing field caused by the ring curvature likely decreases the effective field inside the ring. As a result the effective saturation magnetization for the ring should be reduced as it was indeed found.
For a better comprehension of the nature of the observed modes the detailed static magnetization configuration was determined by micromagnetic simulations. Fig. 6.7(a) shows the static spin configuration represented by the arrows together with the y-component of the magnetization $\boldsymbol{M}$ encoded by the black/white contrast. The dynamic modal structure of mode 1 and mode 5 (grey scale) is depicted together with the static magnetization configuration (arrows) in Figs. 6.7(b) and (c), respectively. One finds that modes 1 to 4 are located in the regions where the magnetization is approximately parallel with respect to the bias field and the ring edges (see Fig. 6.7(a) and (b)). Figure 6.7(a) and (c) expose mode 5 in contrast, to be localized at the position of the transverse domain wall [16, 23] of the onion state, where the magnetization is also aligned parallel to the external magnetic field but perpendicular to the edges of the rings. The resulting demagnetizing field lowers the total effective field in this area

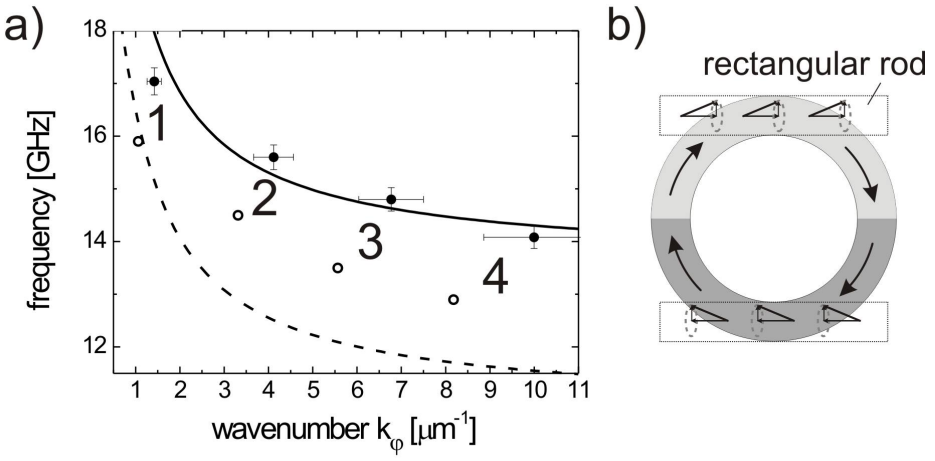

Figure 6.6: *(a) the frequencies of mode 1 - 4 as a function of their wave numbers at $\mu_0 H_0 = 80$ mT obtained by experiment (solid dots) and by simulation (open circles). The solid and dashed line represents the theoretically derived dispersion for a rod (see (b)) and for an infinite film, respectively. The numbers label the different modes. (b) in a simple model proposed by Giesen et al. [110], the arms of the ring can be approximated by uniformly magnetized rectangular rods (confer to the solid line in (a)).*

with respect to the arm region leading to the lower resonance frequency of this mode. When considering the information obtained from the spatially resolved investigations, the bias field behavior of the modal spectrum shown in Fig. 6.3(a) can be understood as follows: the total internal field of the rings is dominated by the demagnetizing field, so that the resonance frequency is determined by the demagnetizing factors and the external field. Since the observed modes have magnetostatic backward volume character, the introduction of additional nodes leads to a reduction of the effective demagnetizing field. This reduction can be compensated by the application of an external bias field. Therefore, the resonance of higher modes is observed at higher fields. According to this model, the onset of higher modes should appear at lower frequencies. However, since the magnetic response is averaged over 700 rings, a strong decrease of the inductive signal is observed as the onset threshold is approached. At the same time the inductive signal decreases with increasing node number (see Fig. 6.3(b)), which leads to an upshift of the detectible onset threshold for higher modes. As a consequence, mode 1 to 4 appear to start nearly at the same frequency.

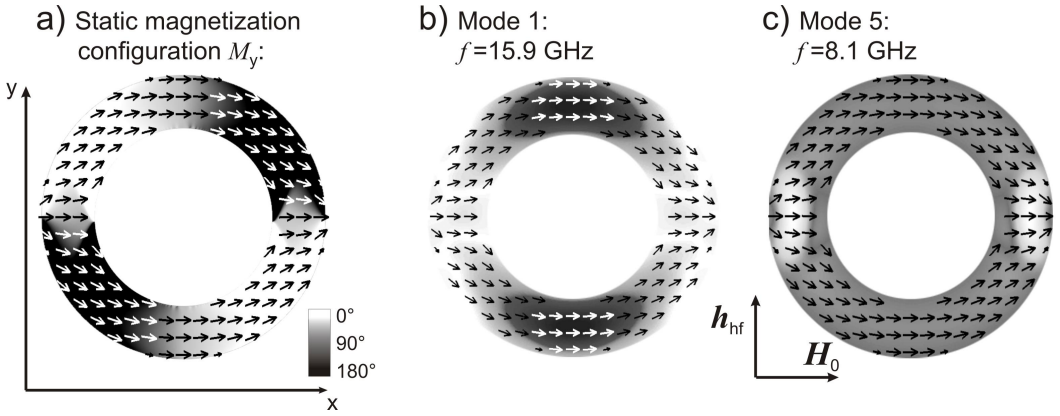

Figure 6.7: *Simulation of the static magnetization configuration together with the dynamic modal structure at $\mu_0 H_0 = 80$ mT. The arrows indicate the direction of the magnetization. In (a) the static y-component of the magnetization $\boldsymbol{M}$ is represented by the black/white contrast (negative and positive y-directions). Figures (b) and (c) show the dynamic modes 1 and 5 superimposed by the static spin configuration, respectively. It can be seen that these modes are localized in the 'arms' of the ring (b) and the domain wall area (c).*

6.4 Dynamic Inter-Ring Coupling

Due to the small spacing of the rings along the x-direction, static magnetic coupling was observed by means of MOKE loops. The stray field of the onion state leads to dipolar coupling of neighboring rings, which energetically increases the onion to vortex transition threshold. This coupling causes a narrowing of the hysteresis loop as reported by Kläui et al. [112]. In the case of the investigated Co rings the static coupling causes a narrowing of approximately 2 mT for small inter-ring spacing.

In order to investigate the effect of coupling on the dynamic properties, some rings of the array were removed by means of a focused ion beam. Consequently, single rings with inter-ring spacing larger than 900 nm could be investigated. As already demonstrated in Section 5.2.4 the FMR-SKEM setup allows to perform spatially resolved frequency sweeps which yield the resonance frequency of a single mode. The open and solid dots in Fig. 6.8(a) show the frequency sweeps performed on a ring in the onion state with small and large spacing to the adjacent rings, respectively. The frequency shift of the fundamental MSBVW mode arising from neighboring rings, was found to be $\Delta f \sim 160$ MHz. In order to confirm this result, simulations were carried out for a single ring and for a row of rings using periodic boundary conditions. The Fourier transform for the fundamental mode in the onion state is represented by the bold dashed and solid lines in Fig. 6.8(a) for the coupled and the single ring, respectively. According to the simulation the frequency shift is $\Delta f = 200$ MHz. In addition, micromagnetic simulations were carried out for the vortex state and revealed the same frequency shift for coupled and single ring environments. The fact that the frequency shift was found to be the same for the modes in the onion and the nominally stray-field free vortex state implies that the origin of the coupling cannot be static. Therefore, the frequency shift is attributed to result from dynamic dipole coupling.
A likely mechanism of the dynamic inter-ring coupling is illustrated in Fig. 6.8(b). The wavelength of the exciting sinusoidal hf field is of the order of 1 cm, hence much larger than the distance of 1.8 μm between neighboring rings. Thus, the magnetic moments in adjacent rings precess with the same phase so that their dynamic stray field $h_{\mathrm{hf}}^{\mathrm{stray}}$ mutually increases the effective field inside the neighboring rings. As a consequence, even the small dynamic deviations of the spins from the stray field free static vortex

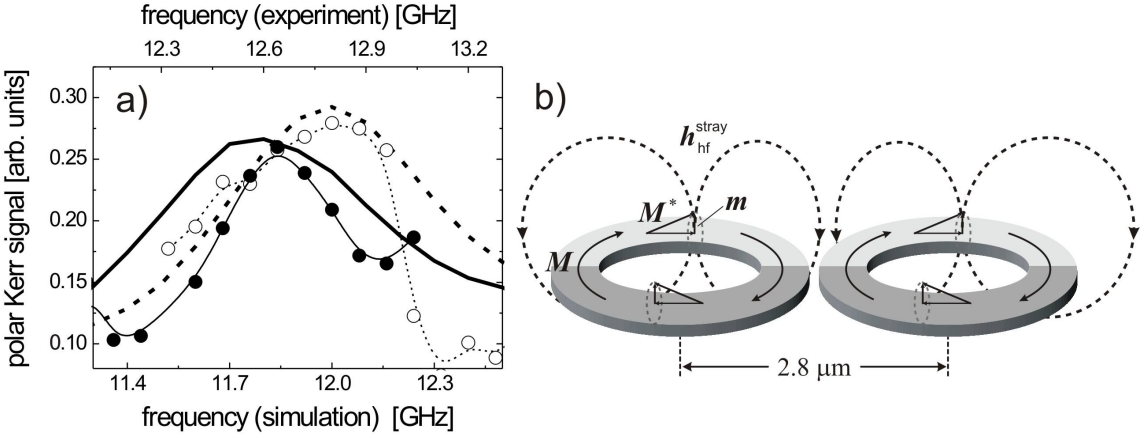

Figure 6.8: *(a) experimental data from frequency sweeps using FMR-SKEM (dots and lines) together with global Fourier transformations of simulated (bold lines) data for the remanent onion state at $H_0 = 0$. Simulated and experimental data correspond to the bottom and top frequency axis, respectively. The solid and the dashed lines represent the single and the coupled ring, respectively. (b) illustration of the effect of inter-ring coupling for adjacent rings mediated by the dynamic stray field $\boldsymbol{h}_{\mathrm{hf}}^{\mathrm{stray}}$.*

state are sufficient to mediate significant coupling. The coupling field H_{coup} enters the dispersion relation of the magnetostatic backward volume wave (Eq. 2.41) in an additive way: $H_{\mathrm{eff}} = H_{\mathrm{int}} + H_{\mathrm{coup}}$. When estimating its strength from the frequency shift one obtains ~ 0.5 mT. In doing so the arms of the ring are approximated by uniformly magnetized rectangular rods, as shown in Fig. 6.6(b).

7 Summary and Outlook

7.1 Summary

The aim of this thesis was to study the effects of confining the geometrical dimensions on the dynamic eigenmode spectra of ferromagnetic systems. For this purpose both inductive and spatially resolved optical techniques were developed and employed.

In **Chapter 4** at first the results from vector network analyzer ferromagnetic resonance (VNA-FMR) measurements of an epitaxial 16 ML thick Fe film fabricated on GaAs(001) substrate were presented and discussed. Data obtained from reflection and transmission measurements were compared to the theoretically derived susceptibility. Even though only measurements of the reflection parameter with a shorted waveguide can be transformed directly into the dynamic susceptibility, the presented results demonstrate that the resonance frequency and the linewidth can be reliably extracted also from transmission measurements, which offer a considerably higher signal to noise ratio (SNR). The effect of inhomogeneous waveguide excitation on the dynamic response was evaluated and found to be negligible for the ultrathin Fe film. In order to test the reliability of the novel frequency domain technique, in the second part of Chapter 4, the results from VNA-FMR were compared to pulsed inductive microwave magnetometry (PIMM), time resolved scanning Kerr microscopy (TR-SKEM) (both methods in the time domain), and conventional ferromagnetic resonance (FMR) in terms of position and width of the ferromagnetic resonance. Concerning the frequency very good agreement with theoretical expectations was found for all four techniques. For the measured effective damping good agreement between the techniques but a deviation from the intrinsic bulk value was found. The observed enhancement was attributed to the modified electronic structure of the ultrathin film in combination with impurity and interface scattering. Finally, the various techniques were compared with respect to their signal to noise ratio. The highest SNR per spin was obtained using TR-SKEM. However, concerning the inductive techniques the highest SNR per spin was obtained by using the VNA-FMR technique.

On account of this high SNR per spin and the fact that the external magnetic field is not required to be changed during the measurement, the VNA-FMR technique allows to investigate small magnetic elements with nonuniform magnetization configuration. This was demonstrated in the first part of **Chapter 5**, where the absorption spectrum of permalloy disks with a diameter of 200 nm and a thickness of 15 nm could be recorded both in the vortex and in the saturated state. In doing so up to 8 distinct resonance peaks were observed in the absorption spectrum. The spatial structure of the corresponding modes was derived from numerical calculations and revealed that both

dipole and exchange dominated azimuthal modes up to the 5^{th} order were observed inductively.
In the second section of Chapter 5 the eigenmode spectrum of larger permalloy disks with a diameter of 4 μm and a thickness of 20 nm was presented and discussed. In a first approach, the modal structure of the disks was recorded at zero bias field, by means of spatially resolved techniques using Kerr microscopy. A comparison of the results from pulsed excitation to micromagnetic simulations exposes disturbed azimuthal normal mode patterns. The disturbance could be attributed to the interaction of the normal modes with the perpendicular magnetization component at the center of the flux-closure vortex configuration. Moreover, employing a novel spatially resolved ferromagnetic resonance scanning Kerr microscopy (FMR-SKEM) technique allowed to detect the normal modes up to the 5^{th} radial order.
The second part of the section addresses the microwave response of the disks as a function of an external in-plane magnetic field, by employing VNA-FMR and spatially resolved FMR-SKEM techniques. Below the vortex annihilation field the fundamental mode (1, 1) was found to split into two modes with different field behavior induced by the displacement of the vortex core. Above the vortex annihilation field, two different regions could be distinguished in terms of the effective field inside the disk. In the homogeneous region around the disk center, Damon Eshbach (DE) like modes quantized transversely to the external field were observed up to the 9^{th} order. In addition, a strongly inhomogeneous field distribution in the vicinity of the disk edges (perpendicular to the external field) was observed to cause localized edge modes quantized parallel to the external field. Finally, in addition to the center region, Damon Eshbach like modes were found also in the inhomogeneous edge region. Due to the diverse effective fields, the dispersion relation of the DE mode in the edge region was found to be shifted towards lower frequencies with respect to the DE mode in the center region. As a consequence, two distinct mode patterns with different wave numbers, were found at the same frequency. These results clearly disclose an influence of the effective field along the external field on the transversely quantized DE modes. Generally, the experimental results were found to be in good agreement with those from micromagnetic simulations.

In **Chapter 6** the eigenmode spectra of cylindrical ring magnets were presented and discussed. In the first part of the chapter the dynamic response of the rings was studied as a function of an external in-plane magnetic bias field by employing inductive VNA-FMR technique. Up to five resonant eigenmodes were observed in the frequency range from 0.045 to 20 GHz. The intensities of the resonance lines from VNA-FMR as well as the modal pattern obtained from spatially resolved FMR-SKEM investigations, allowed to study the hysteretic two step transition from onion to vortex to reverse onion in terms of its dynamical features.
The second part of Chapter 6 presents the eigenmode structure in ferromagnetic rings at 80 mT bias field. Magnetostatic backward volume like modes were observed up to the 4^{th} odd order. These modes are localized in the arms of the ring parallel to the external field. When approximating the arms by a rectangular rod, the comparison of the experimental results to the theoretically derived dispersion relation of the MSBVW yields good agreement. Furthermore, an additional mode was found in the transverse

domain wall of the onion configuration. Since the demagnetizing field lowers the effective field in this region, this mode was found to lie much lower in frequency with respect to the MSBVW modes.
In the third part of Chapter 6 dynamic inter-ring coupling was discussed for the first time. Frequency scans by means of FMR-SKEM were performed in order to determine spatially resolved resonance lines of single rings. As a result the frequency shift of the fundamental MSBVW mode of the rings with 100 nm and 900 nm (edge to edge) inter-ring spacing was determined to be $\Delta f \sim 160$ MHz. The shift was addressed to a dynamic dipolar coupling process occurring between the elements. For all the results of Chapter 6 very good agreement between the experiment and the micromagnetic simulations was again observed.

7.2 Outlook

In recent years much effort has been put into the identification of the eigenmodes in small magnetic elements with a flux-closure vortex configuration since these elements might be the key to high density recording media. Indeed, when decreasing the dimensions of the magnetic elements into the nanometer regime the interaction of the normal modes with the vortex core has to be taken into account. As discussed in Subsection 5.2.3, the influence of the vortex core on the azimuthal modes has been shown by Park and Crowell [99] using time resolved scanning Kerr microscopy. However, by employing continuous wave excitation the gyrotropic vortex motion might be excited independently from the normal modes allowing one to explicitly study their mutual interaction.
Buess et al. [68] reported of the effect of normal mode conversion in permalloy disks having a vortex configuration. Since the normal modes were found to be eigenfunctions of the system, for a consistent explanation one has to take into account a disturbance of the eigenmodes which might be introduced by the vortex core motion. Using resonant microwave packets might allow to combine the advantages of the pulsed and continuous wave excitation. The temporal evolution and conversion of the modes could be investigated independently. Furthermore this technique may be applied in order to investigate precessional switching by means of pulsed continuous wave excitation.

A Appendix

A.1 Vector Network Analyzer Operation Mode

The most common application of network analyzers is communications engineering where it is employed to determine the microwave properties of circuits. However, the features of this device constitute a promising alternative for the investigation of magnetization dynamics, which occurs in the microwave frequency range. Its principle architecture is schematically depicted in Fig. A.1. The internal oscillator (hf source) generates a sinusoidal signal with a frequency f. In order to provide a reference signal for ratio measurements this signal is divided into incident and reference waves by means of a directional coupler operated in forward direction. The impedance and transmission characteristic of the Device Under Test (DUT) determines the portion of reflected and

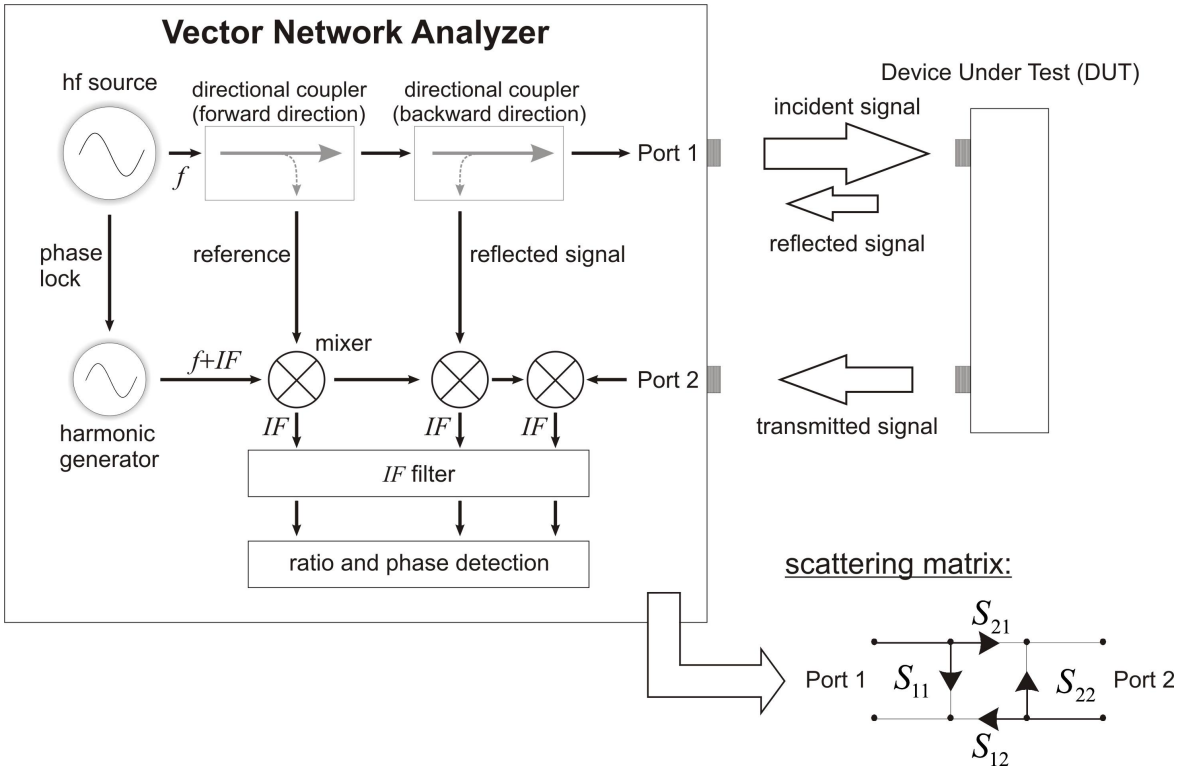

Figure A.1: *The fundamental architecture of a vector network analyzer as used for a S_{21} (transmission from port 1 to port 2) and S_{11} (reflection from port 1 back to port 1) measurement. The scattering matrix for a two port network can describe the four possible types of measurements as illustrated by the diagram bottom right.*

transmitted waves. The signal reversed by the DUT is guided to the detector by means of a directional coupler operated in reverse direction. The detection and processing of signals in the microwave range is very difficult and sometimes not even possible. Therefore, the high frequency signals are transformed to an intermediate frequency IF in the range of a few kHz. For this purpose an additional hf source generates a signal with frequency $f + IF$ phase locked to the signal f. This second wave is compared to the reference, reflected, and transmitted waves by means of microwave mixers. In doing so the mixers transform the original signal to the frequency IF. Subsequent filtering and amplification of the signal by means of Low Noise Amplifiers (LNA), enhances the signal to noise ratio. In order to investigate the dynamic properties of the DUT, the frequency of the hf source is set to sweep over a specified bandwidth [113, 114].
The maximum frequency range of the VNA employed in this thesis (Agilent PNA E8362A) is from 45 MHz to 20 GHz with a dynamic range of more than 110 dB. Fig. A.1 shows the layout of the microwave circuit for a reflection measurement from port 1 back to port 1 and for transmission measurement from port 1 to port 2. Network analyzers are usually able to perform bidirectional measurements. Therefore, a so-called scattering matrix S_{ij} can be defined (see bottom right in Fig. A.1), which is given by the ratio of the voltages of the outgoing to the incident waves at ports i and j of the DUT, respectively:

$$S_{ij} = \left. \frac{V_i^{out}}{V_j^{in}} \right|_{V_k=0 \text{ for } k \neq j} \tag{A.1}$$

The incident waves coming from all other ports except port j are set to zero. Consequently, S_{ii} are the reflection and S_{ij} the transmission coefficients, which can be directly measured as a function of the frequency using the network analyzer. The concept of scattering parameters is discussed in more detail in Appendix A.3.1.
There are two types of network analyzers, namely scalar and vector analyzers. The scalar type only measures the amplitude ratio, whereas the vector analyzer in addition determines the phase correlation of the complex high frequency signals. As shown in

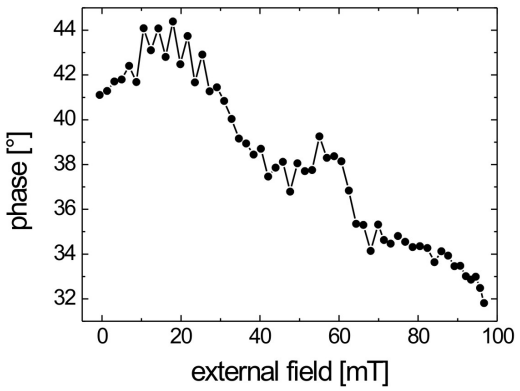

Figure A.2: *The phase shift of the asymmetric resonance line as a function of the external magnetic bias field.*

Subsection 2.2.2 the dynamic response of a magnetic system is governed by the complex microwave susceptibility $\chi = \chi' + i\chi''$. Thereby, the real part χ' corresponds to a variation of the electrical length, while the imaginary part χ'' corresponds to the resonant absorption by the magnetic sample. The complex scattering parameters obtained from VNA measurements offer the possibility to measure both real and imaginary parts of χ. Note that the real and imaginary part of S_{ij} correspond to the imaginary and real part of the susceptibility, respectively. Since real and imaginary part of χ are connected via the Kramers-Kronig relations [115], a variation of one component inevitably causes a change of the other one. In practice, changing χ' is connected with a variation of the sample's dielectric constant and hence alters the propagation velocity of the waves travelling along the waveguide. This in turn causes a phase-lag of the detected signal with respect to the reference signal near the resonance frequency. In addition, also the external bias field leads to a change of the propagation characteristic of the waveguide, which again results in a phase-lag of the detected signal. However, this phase-lag is constant at constant bias field and thus can be accounted for by adding a constant phase shift to the measured phase. Fig. A.2 shows the phase shift of the asymmetric resonance line as a function of the external bias field. Because of this correlation of both parts of χ, only vectorial measurements allow to separately determine both phase and amplitude of the hf signal and thus are necessary to extract χ'' from the experimental data. Fig. A.3(a) shows data from VNA-FMR measurements of the 16 ML thick Fe film at $\mu_0 H_0 = 46$ mT (cf. Chapter 4). In order to increase the signal to noise ratio reference data is subtracted from the data recorded at the corresponding bias field as described in Section 3.1. For this reason a phase lag between the reference and the measurement leads to an asymmetric resonance line. However, by adding a phase offset, the resonance lines can be transformed into purely symmetric and antisymmetric curves as demonstrated in Fig. A.3(b). These symmetric and antisymmetric shaped curves correspond to the imaginary and real part of the susceptibility found in Subsection 2.2.2.

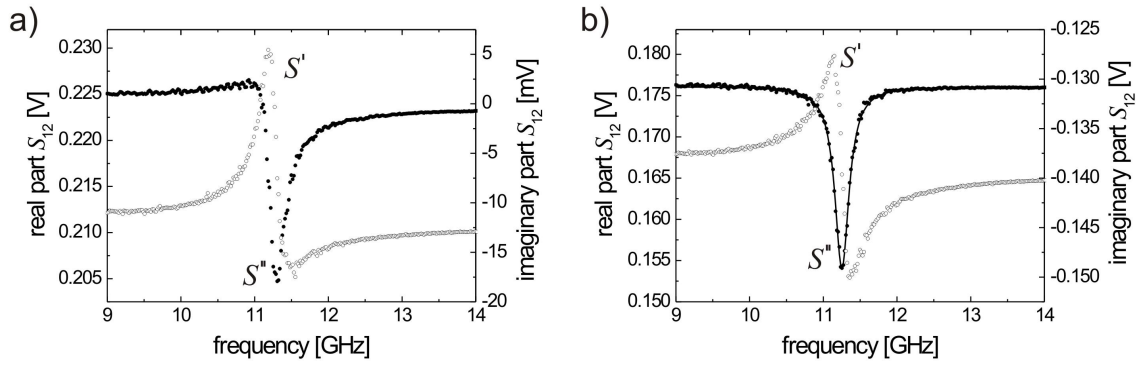

Figure A.3: *The real (solid dots) and imaginary (open dots) parts obtained by VNA measurements. Both parts of the unprocessed data in (a) show an asymmetric shape. By shifting the phase of the complex data the real and imaginary part becomes purely symmetric and antisymmetric Lorentzian lines, respectively (b). The solid line in (b) represents a fit to a Lorentzian curve.*

A.2 Waveguide Characterization

The gyromagnetic ratio γ acts as a pre-factor in the LLG equation and hence determines the relevant frequency regime of the magnetization dynamics. It is given by $\gamma = g \times 13.996$ GHz/T, where the g-factor is of the order of 2 for ferromagnetic materials. Consequently, the precession of the magnetic moments typically takes place in the frequency range starting at hundreds of MHz up to several tens of GHz depending on the applied magnetic field. This frequency range corresponds to the electromagnetic microwave spectrum. As a consequence, in order to resonantly excite the magnetic samples microwaves are required. Due to the properties of the electromagnetic waves carefully designed waveguides are required to guide the microwaves to the investigated sample. In the present work coplanar waveguides (see Fig. A.4) were employed which consist of a central conductor carrying the current i. This signal line is surrounded by ground planes at a distance s on each side carrying the current $-i/2$. All waveguides were fabricated in the clean room facility at the chair of Prof. Weiss. Details concerning the preparation can be found in Appendix A.4. Two different center conductor widths were employed, namely 10 and 90 μm. In order to match the impedance of the waveguides to 50 Ω the ratio between the signal line width and its distance to the ground planes was found by using a commercial electro-magnetic software package [78] to be best at 10:7 for GaAs substrate. The corresponding transmission of a waveguide is shown in Fig. A.5 in units of dB ($= 10\, log_{10}(P_{out}/P_{in})$). Apart from some peaks the transmitted power is above -1.5 dB throughout the total frequency range, which corresponds to 71% of the incident power.

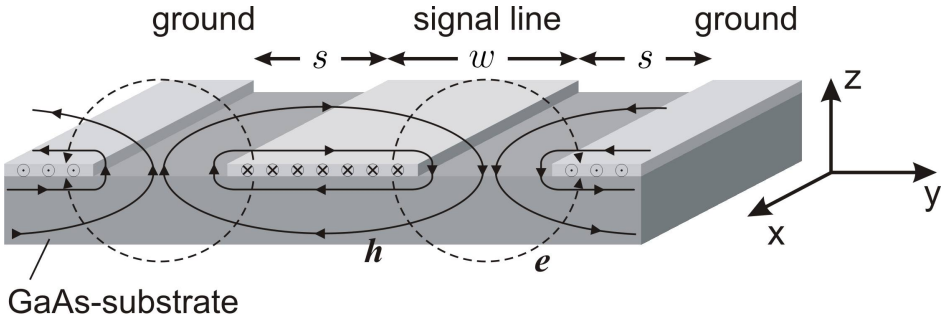

Figure A.4: *The coplanar waveguide consisting of a central signal line which carries the current* $\boldsymbol{i}$*. Each surrounding ground plane carries the current* $-\boldsymbol{i}/2$*. Induced by the current flow a magnetic field* $\boldsymbol{h}$ *curls around the conductors (solid lines) and an electric field* $\boldsymbol{e}$ *points from the central line towards the ground planes (dashed lines).*

The current travelling along the waveguide generates a transverse magnetic field mainly in y-direction above the conductors and a perpendicular field mainly in z-direction near the edges of the conductors (see Fig. A.4). The magnetic fields above a two dimensional gapped recording head can be approximated by means of the Karlqvist equation [116]. In the derivation of this formula one assumes boundary conditions of linearly increasing potential across the gap. This approximation is still valid for calculating the field due

to a current sheet (see [117], p. 51). The resulting transverse and perpendicular fields are given by

$$H_y = \frac{\mu_0}{\pi}\frac{I}{2w}\left[\arctan\left(\frac{(w/2)+y}{z}\right)+\arctan\left(\frac{(w/2)-y}{z}\right)\right] \tag{A.2}$$

and

$$H_z = \frac{\mu_0}{\pi}\frac{I}{4w}\; ln\left(\frac{((w/2)-y)^2+z^2}{((w/2)+y)^2+z^2}\right), \tag{A.3}$$

respectively. With I being the current inside the sheet and w being the signal line width. For the definition of the coordinates see Fig. A.4. Assuming uniform current density throughout the conductors, the field profile for the transverse and perpendicular components according to Eqs. A.2 and A.3 is depicted in Figs. A.7(a) and (b), respectively.

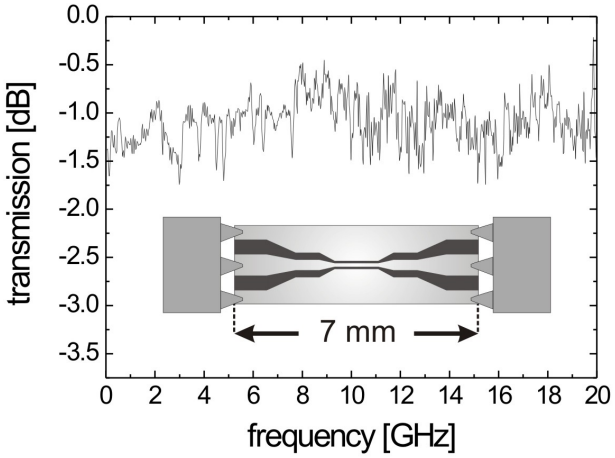

Figure A.5: *The transmission loss of a coplanar waveguide with a length of 7 mm measured with the VNA. The waveguide is connected by using air coplanar probes. In order to enhance the magnetic hf field amplitude the signal line was tapered in two steps from 90 µm at the edges down to 10 µm in the center where the magnetic sample is placed. The image shows a schematic sketch of the waveguide connected to the probes.*

For high frequency signals the skin effect causes the current to accumulate at the boundaries of the conductor and to vanish at its center. The skin depth is given by $\delta_s = 1/\sqrt{\pi\,\mu_0\,\sigma\,f}$, where σ is the conductivity of the material. For Cu and Au the skin depth is above 400 nm at $f = 10$ GHz. Thus, for the employed waveguides with a thickness of less than 400 nm the skin effect can be neglected. Nevertheless, the numerical solution of Maxwell's equations exposes a nonuniform density of the hf current traversing the waveguide. Indeed, the current density is found to rise towards the conductor edges [118]. This effect known as edge singularities [119] increases with the frequency. The realistic current distribution is given by Eq. 4.17. One can determine the proportionality factor C by fitting Eq. 4.17 to the current density profile obtained from commercial E-M software [78] as shown in Fig. A.6. When inserting this current density into Eqs. A.2 and A.3, one obtains the transverse and perpendicular hf field

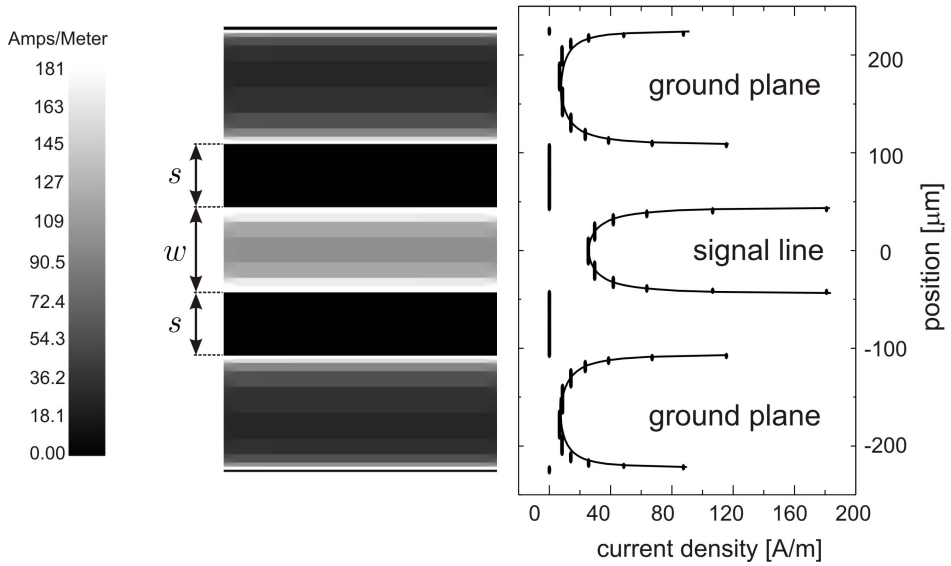

Figure A.6: *The current density calculated for a coplanar waveguide with a signal line width of $w = 90$ μm and a gap of $s = 63$ μm. A sinusoidal signal with a frequency of $f = 10$ GHz and a power of 1 mW was assumed. The data encoded by the black/white contrast was obtained from a simulation using an E-M software package [78]. The dots in the graph represent a vertical line scan of the simulated data. Discretization of the waveguide leads to jumps in the current density profile. The solid lines represent fits to Eq. 4.17.*

profiles shown in Figs. A.7(c) and (d), respectively. A comparison to the magnetic field for uniform current density (Figs. A.7(a) and (b)) exposes considerable changes of the field profile for both components of h_{hf}. While the transverse field is quasi uniform above the conductors for uniform current density, on account of the edge singularities pronounced peaks at the conductor edges appear for realistic current density (cf. Fig. A.7(a) and (c)). A similar behavior can be observed for the perpendicular field. Though it shows already maxima near the conductor edges for the uniform case, the field in the center region vanishes almost totally for the nonuniform current density. Indeed, this effect leads to approximately purely in-plane transverse field at the center of the signal line.

Assuming a coplanar waveguide with a 10 μm wide signal line the transverse in-plane hf field amplitude at the center calculated by the Karlqvist formulas is 0.22 mT and 0.19 mT for uniform and realistic current density, respectively. The calculations were carried out for the same electrical parameters as used for the calculations shown in Fig. A.7. However, the distance above the waveguide was assumed to be 10 nm, since the 10 μm wide signal line was used only for magnetic elements fabricated directly on top of the metallization.

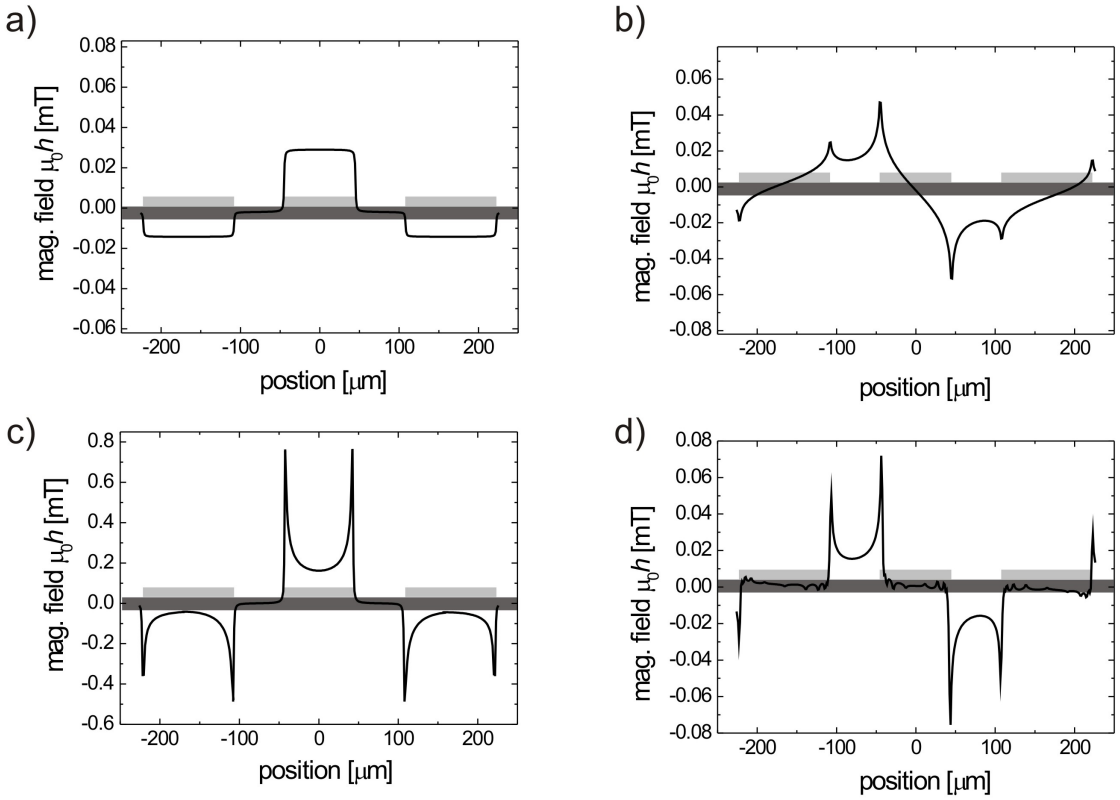

Figure A.7: *The y- (plot (a) and (c)) and z-components (plot (b) and (d)) of the magnetic field generated by a coplanar waveguide at a distance of 0.5 μm above the metallization. When assuming uniform current density throughout the conductors the obtained field profile is given by plot (a) and (b). Considering edge singularities for the current distribution (see Fig. A.6), one obtains a more realistic field profile shown in plot (c) and (d) for $f = 10$ GHz. Schematic sketches illustrate the waveguide cross section in the graphs. For calculating the field profile by means of the Karlqvist equations A.2 and A.3 a waveguide with 90 μm signal line width, 63 μm gap, and 114 μm ground plane width was considered. The input power of 1 mW was assumed to suffer -2 dB attenuation.*

A.3 From Scattering Parameters to Magnetic Susceptibility

A.3.1 The Concept of Scattering Parameters

It has been shown in Subsection 2.2.2 that by employing resonance techniques the response is given by the hf susceptibility of the magnetic sample. However, for the conversion of the measured parameter into the dimensionless susceptibility one needs to account for the particular detection scheme. This section outlines the conversion from scattering parameters obtained from VNA-FMR measurements into susceptibility.

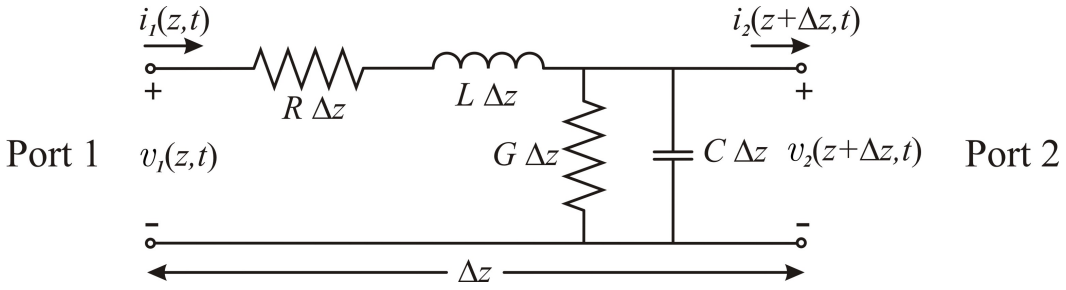

Figure A.8: *The coplanar waveguide can be regarded as composed of lumped elements as shown here (see [113]). Thus, the current i and voltage v can be assumed to be constant along the length Δz of each element.*

The key problem of the analysis for microwave circuits applications is that the wavelength is of comparable size as the physical dimensions of the circuit. Thus, both the magnitude and the phase of the voltages and currents usually vary over the length of the circuit. Therefore, it becomes necessary to treat the circuit like a lumped-element model [113] as shown in Fig. A.8. To do this it is important to realize that the waveguide supports quasi Transverse-Electro-Magnetic (TEM) modes, which is guaranteed for coplanar waveguides in the relevant frequency range. Within this model the waveguide is divided into small elements, hence the current and voltage can be assumed to be constant along their length. Every element is characterized by:

- L, the total self inductance of the conductors per unit length.
- R, the series resistance per unit length caused by the finite conductivity of the metallization.
- G, the shunt conductance per unit length caused by dielectric losses from the substrate.
- and C, the shunt capacitance per unit length caused by the close proximity of the signal line and the ground planes.

This model allows to define the characteristic impedance which corresponds to the hf resistance of the waveguide. Just like its static analogon the hf impedance is defined

as the ratio of the voltage V_0 to the current I_0 of the waves

$$Z_0 = \sqrt{\frac{R + i\omega L}{G + i\omega C}} = \frac{V_0^{in}}{I_0^{in}} = \frac{-V_0^{out}}{I_0^{out}}, \tag{A.4}$$

where V_n^{in} is the voltage amplitude of the wave incoming at port n and V_n^{out} is the voltage amplitude of the wave coming out of port n. In the case of a two port circuit as shown in Fig. A.8 the currents and voltages at port 1 and port 2 are related to each other via the impedance matrix:

$$\begin{bmatrix} V_1 \\ V_2 \end{bmatrix} = \begin{bmatrix} Z_{11} & Z_{12} \\ Z_{21} & Z_{22} \end{bmatrix} \begin{bmatrix} I_1 \\ I_2 \end{bmatrix}. \tag{A.5}$$

However, it is difficult to directly measure the waves travelling along a waveguide. A more practical approach to analyze a circuit at microwave frequencies is the concept of scattering parameters, which are directly measured by means of a network analyzer. As already shown in Appendix A.1, these parameters relate the voltages of the incoming and outgoing waves of the network at port i and j. For the 2-port network shown in Fig. A.8, the related scattering matrix is defined by

$$\begin{bmatrix} V_1^{out} \\ V_2^{out} \end{bmatrix} = \begin{bmatrix} S_{11} & S_{12} \\ S_{21} & S_{22} \end{bmatrix} \begin{bmatrix} V_1^{in} \\ V_2^{in} \end{bmatrix}. \tag{A.6}$$

Conversion of the scattering matrix $\underline{S}$ into the impedance matrix $\underline{Z}$ can be achieved by using the relation

$$\underline{Z} = (\underline{U} - \underline{S})^{-1} (\underline{U} + \underline{S}), \tag{A.7}$$

with $\underline{U}$ being the unit matrix. For a shorted waveguide, i.e. only port 1 remains, this conversion simplifies to

$$Z_{11} = Z_0 \frac{1 + S_{11}}{1 - S_{11}}. \tag{A.8}$$

The purpose of this brief introduction into the concept of microwave impedance and scattering parameters does not claim completeness. Further details can be found in [113].

A.3.2 Conversion to Susceptibility

In the following a magnetic film is placed on top of the signal line of a coplanar waveguide. This situation corresponds to the measurement of the Fe film presented in Chapter 4. However, the concepts developed here can be extended to confined magnetic elements. The crucial question is how to obtain the hf susceptibility starting from the scattering parameters measured by the vector network analyzer. The effect of placing a magnetic sample on top of a waveguide is to change the magnetic flux Φ

surrounding the waveguide. The general expression of a magnetic flux penetrating the area F is given by [120]

$$\Phi = \int_A \boldsymbol{B}\, dF. \tag{A.9}$$

In the case of the waveguide, the area F corresponds to the expansion of the film along the waveguide l times its thickness t. The magnetic induction generated by the high frequency signal reads $B = \mu\, h_{\mathrm{hf}}$. Where $\mu = \mu_0(\mu_r - 1)$ being the magnetic permeability which is related to the susceptibility by $\mu = \mu_0\chi$. Uniform current density is considered, thus the in in-plane hf component of the magnetic field h_{hf} is supposed to be constant above the signal line. With this assumptions the magnetic flux is given by

$$\Phi = \int_0^l \int_0^t \mu_0\, \chi\, h_{\mathrm{hf}}\, dx' dz' = \mu\, l\, t\, h_{\mathrm{hf}}. \tag{A.10}$$

As a result the change of the magnetic flux due to the presence of the magnetic film is accounted for by the susceptibility

$$\Delta\Phi = \mu_0\, \chi\, h_{\mathrm{hf}}\, l\, t. \tag{A.11}$$

Applying Faraday's law the voltage induced into a conductor due to a change of the magnetic flux is given by

$$v_{\mathrm{hf}} = -\frac{\mathrm{d}\Phi}{\mathrm{d}t} = \mu_0\, \chi\, l\, t\, \frac{\mathrm{d}h_{\mathrm{hf}}}{\mathrm{d}t} \;=\; -i\,\omega\,\mu_0\,\chi\, l\, t\, h_{\mathrm{hf}}. \tag{A.12}$$

Here the time dependence of the sinusoidal high frequency field was assumed to be of the form $e^{i\omega t}$. The impedance of the waveguide $\Delta Z = v_{\mathrm{hf}}/i_{\mathrm{hf}}$ was derived above. It follows that the corresponding change of the impedance is given by

$$\Delta Z = \frac{-i\,\omega\,\mu_0\,\chi\, l\, t\, h_{\mathrm{hf}}}{i_{\mathrm{hf}}}. \tag{A.13}$$

From this equation one finally arrives at an expression for the susceptibility [121]

$$\chi(\omega) = \frac{i_{\mathrm{hf}}\, \Delta Z}{i\,\omega\,\mu_0\, h_{\mathrm{hf}}\, l\, t}. \tag{A.14}$$

For reflection measurements the impedance is simply connected to the scattering parameter S_{11} by Eq. A.8. This implies that Z_0 is dependent on ω. However, as described in Section 3.1, the VNA-FMR measurements were carried out by subtracting a reference measurement from the actual data. As a consequence, the frequency dependence of the characteristic impedance of the waveguide is eliminated, i.e. one can assume $Z_0/\omega \sim Z_0/\omega_r$ in good approximation. Finally, the susceptibility as a function of the scattering parameter S_{11} reads

$$\chi = \frac{i_{\mathrm{hf}}\, Z_0}{\omega_r\, \mu_0\, h_{\mathrm{hf}}\, l\, t}\; \frac{2Im - i(1 - Re^2 - Im^2)}{1 - 2Re + Re^2 + Im^2}, \tag{A.15}$$

where Im and Re correspond to the measured real and imaginary part of S_{11}. As shown in Appendix A.2, h_{hf} can be calculated by applying Eq. A.2.

A.4 Sample Dimensions and Preparation

Not all of the investigated samples were fabricated by my self in the clean room facility at the chair of Prof. Weiss. Therefore, the preparation differs for the various samples. In the following an itemization of preparation procedures is given:

1. **Waveguides:**

   The metallization of the waveguides was defined onto the high-resistivity GaAs by means of standard optical lithography, thermal evaporation, and a subsequent lift-off process. The fabrication in detail:

   - Cleaning the GaAs-substrate in Aceton and Propanol
   - Spinning (1 s at 3000 U/min + 30 s at 6000 U/min) the optical photo resist AR-P (374 1:0) onto the substrate
   - Illumination of the resist for approximately 30 s
   - Developing of the resist for approximately 30 s in 10 ml NaOH / 30 ml H_2O
   - Growth of the metallization at a base pressure of $\sim 3 \times 10^{-4}$ Pa (Leybold Univex):
     - Adhesion to the surface is enhanced by first sputtering the substrate with Ar for 2 min (2 kV, 20 mA) and subsequently depositing 10 nm Ti onto the GaAs by means of electron gun vaporization
     - As metallization of the waveguide material 200 nm Cu and subsequently 150 nm Au is evaporated onto the adhesion layer by means of thermal vaporization from a shuttle
   - Lift-off in Aceton

   The fabricated waveguides have a dc resistance of less than 10 Ω.

2. **Ultrathin Fe Film:**

   The ultrathin 16 ML thick Fe(001) film was prepared by means of molecular beam epitaxy by G. Woltersdorf [59]. Semi-insulating, epi-ready GaAs(001) wafers were used as templates. The GaAs substrate was heated to 400° C in ultra high vacuum for 10 hours in order to desorb contaminants. Residual oxides and carbon were removed by reactive desorption using an atomic hydrogen source at 400° C. After 1 hour of hydrogen treatment the surface contamination was below the detection limit of Auger electron spectroscopy. Subsequent annealing at up to 600° C was monitored using Reflection High Energy Electron Diffraction (RHEED) until a well ordered 4×6 reconstruction appeared. The Fe and Au films were grown at room temperature from a thermal source at a base pressure of less then 2.7×10^{-8} Pa with a deposition rate of ~ 1 ML/min [122]. The film thickness was monitored by a quartz crystal microbalance and RHEED intensity oscillations. The Fe film was capped by 20 ML Au for protection under ambient conditions.

3. Confined Elements:

All small elements were fabricated by means of electron beam lithography, thermal evaporation, and a subsequent lift-off process. The fabrication is described in detail for the Py disks with 4 μm diameter prepared in the clean room facility in Regensburg.

a) Py disks with 200 nm diameter:
The (2×2) mm^2 sized array of permalloy (Py – $Ni_{81}Fe_{19}$) disks with a diameter of $d = 200$ nm, a thickness of $t = 15$ nm and a separation of $s = 200$ nm (edge to edge) was fabricated using electron gun deposition in a vacuum of $\sim 1 \times 10^{-6}$ Pa by T. Okuno [123]. The array was placed onto a thermally oxidized Si substrate.

b) Py disks with 4 μm diameter:
The Py disks with a diameter of $d = 4$ μm, a thickness of $t = 20$ nm, and a separation of $s = 200$ μm (edge to edge) were fabricated directly on top of the waveguide by means of thermal evaporation. The fabrication process in detail:

- Cleaning the waveguide in Aceton and Propanol
- Spinning (5 s at 3000 U/min + 30 s at 8000 U/min) the first layer of the electron beam resist (PMMA 200 K, 7%) onto the waveguide
- Post-bake at 150 °C for 5 min
- Spinning (5 s at 3000 U/min + 30 s at 8000 U/min) the second layer of the electron beam resist (PMMA 950 K, 2%) onto the first layer
- Again post-bake at 150 °C for 5 min
- Defining the dots into the resist by means of a scanning electron microscope (SM 510) (spot-size 8, current 360 pA, area-dose 230 pC/cm^2)
- Developing the electron beam resist for 3 minutes in Methylisobutylketon (MIBK)
- Evaporation of the magnetic material at a base pressure of $\sim 3 \times 10^{-4}$ Pa (Leybold Univex). For protection against corrosion the magnetic material is subsequently capped with 2 nm Al
- Lift-off in Aceton

c) Co rings:
An array of 2×350 rings was grown by molecular beam epitaxy in ultra-high vacuum at a base pressure of 3×10^{-8} Pa directly on top of a coplanar waveguide by L. Heyderman, D. Backes, and C. A. F. Vaz [107]. The rings were capped by 4 nm Au for corrosion protection. The thickness of the Co rings was $t = 32$ nm, their inner diameter was 1.7 μm, and their width was 500 nm. An inter-ring spacing of $s = 100$ nm along the waveguide and 900 nm in the transverse direction was chosen.

Publications

Part of the work discussed in Chapter 4 has been submitted as:

- **Comparison of frequency, field, and time domain ferromagnetic resonance methods**
  I. Neudecker, G. Woltersdorf, B. Heinrich, T. Okuno, G. Gubbiotti, and C.H. Back
  J. Magn. Magn. Mat.

Part of the work discussed in Chapter 5 has been submitted as:

- **Modal Spectrum of Permalloy Disks Excited by In-Plane Magnetic Fields**
  I. Neudecker, K. Perzlmaier, F. Hoffmann, G. Woltersdorf, M. Buess, D. Weiss and C. H. Back
  Phys. Rev. B

Part of the work discussed in Chapter 6 has been published as:

- **Spatially resolved dynamic eigenmode spectrum of Co rings**
  I. Neudecker, M. Kläui, K. Perzlmaier, D. Backes, L. J. Heyderman, C. A. F. Vaz, J. A. C. Bland, U. Rüdiger, and C.H. Back
  Phys. Rev. Lett. **96**, 057207 (2006)

Publications in collaboration:

- **Spatially resolved ferromagnetic resonance: Imaging of ferromagnetic eigenmodes**
  A. Puzic, B. Van Waeyenberge, K. W. Chou, P. Fischer, H. Stoll, G. Schütz, T. Tyliszczak, K. Rott, H. Brückl, G. Reiss, I. Neudecker, T. Haug, M. Buess, and C. H. Back
  J. Appl. Phys. **97**, 10E704-1 (2005)

- **Vortex dynamics in coupled ferromagnetic multilayer structures**
  K. W. Chou, A. Puzic, B. Van Waeyenberge, H. Stoll, G. Schütz, T. Tyliszczak, K. Rott, G. Reiss, H. Brückl, I. Neudecker, D. Weiss, and C. H. Back
  J. Appl. Phys. (accepted)

- **Fast magnetic vortex core switching effected by resonant excitation**
  B. Van Waeyenberge, A. Puzic, H. Stoll, K. W. Chou, T. Tyliszczak, H. Brückl, K. Rott, G. Reiss, I. Neudecker, C. H. Back , D. Weiss , G. Schütz
  Nature (submitted)

- **Magnetization Dynamics of the Ferrimagnet CoGd near the compensation point**
  M. Binder, A. Weber, O. Mosendz, G. Woltersdorf, M Izquierdo, I. Neudecker, J. Dahn, T. Hatchard, J.-U. Thiele, C. H. Back, M. R. Scheinfein
  Phys. Rev. Lett. (submitted)

Bibliography

[1] S. Blundell. *Magnetism in Condensed Matter.* Oxford University Press, New York (2001).

[2] J.-G. Zhu, Y. Zheng, and G. A. Prinz. "Ultrahigh density vertical magnetoresistive random access memory (invited)". *J. Appl. Phys.* **87**, 6668 (2000).

[3] G. A. Prinz. "Magnetoelectronics applications". *J. Magn. Magn. Mat.* **200**, 57 (1999).

[4] J. Akerman. "Toward a universal memory". *Science* **308**, 508 (2005).

[5] W. K. Hiebert, A. Stankiewicz, and M. R. Freeman. "Direct observation of magnetic relaxation in a small permalloy disk by time-resolved scanning Kerr microscopy". *Phys. Rev. Lett.* **79**, 1134 (1997).

[6] R. J. Hicken and J. Wu. "Observation of ferromagnetic resonance in the time domain". *J. Appl. Phys.* **85**, 4580 (1999).

[7] J. Jorzick, S. O. Demokritov, B. Hillebrands, B. Bartenlian, C. Chappert, D. Decanini, F. Rousseaux, and E. Cambril. "Spin-wave quantization and dynamic coupling in micron-size circular magnetic dots". *Appl. Phys. Lett.* **75**, 3859 (1999).

[8] Y. Acremann, C. H. Back, M. Buess, O. Portmann, A. Vaterlaus, D. Pescia, and H. Melchior. "Imaging precessional motion of the magnetization vector". *Science* **290**, 492 (2000).

[9] S. Tamaru, J. A. Bain, R. J. M. van de Veerdonk, T. M. Crawford, M. Covington, and M. H. Kryder. "Imaging of quantized magnetostatic modes using spatially resolved ferromagnetic resonance". *J. Appl. Phys.* **91**, 8034 (2002).

[10] J. P. Park, P. Eames, D. M. Engebretson, J. Berezovsky, and P. A. Crowell. "Spatially resolved dynamics of localized spin-wave modes in ferromagnetic wires". *Phys. Rev. Lett.* **89**, 277201 (2002).

[11] V. Novosad, M. Grimsditch, K. Y. Guslienko, P. Vavassori, Y. Otani, and S. D. Bader. "Spin excitations of magnetic vortices in ferromagnetic nanodots". *Phys. Rev. B* **66**, 052407 (2002).

[12] B. Hillebrands and K. Ounadjela. *Spin Dynamics in Confined Magnetic Structures I.* Springer Verlag, Berlin (2002).

[13] J. Jorzick, S. O. Demokritov, B. Hillebrands, M. Bailleul, C. Fermon, K. Y. Guslienko, A. N. Slavin, D. V. Berkov, and N. L. Gorn. "Spin wave wells in nonellipsoidal micrometer size magnetic elements". *Phys. Rev. Lett.* **88**, 047204 (2002).

[14] M. B. an D. Olligs and C. Fermon. "Micromagnetic phase transitions and spin wave excitations in a ferromagnetic stripe". *Phys. Rev. Lett.* **91**, 137204 (2003).

[15] G. Gubbiotti, G. Carlotti, T. Okuno, T. Shinjo, F. Nizzoli, and R. Zivieri. "Brillouin light scattering investigation of dynamic spin modes confined in cylindrical permalloy dots". *Phys. Rev. B* **68**, 1844091 (2003).

[16] J. P. Park, P. Eames, D. M. Engebretson, J. Berezovsky, and P. A. Crowell. "Imaging of spin dynamics in closure domain and vortex structures". *Phys. Rev. B* **67**, 020403(R) (2003).

[17] M. Belov, Z. Liu, R. D. Sydora, and M. R. Freeman. "Modal oscillation control in internally patterned $Ni_{80}Fe_{20}$ thin film microstructures". *Phys. Rev. B* **69**, 094414 (2004).

[18] C. Bayer, J. P. Park, H. Wang, M. Yan, C. E. Campbell, and P. A. Crowell. "Spin waves in an inhomogeneously magnetized stripe". *Phys. Rev. B* **69**, 134401 (2004).

[19] L. Giovannini, F. Montoncello, F. Nizzoli, G. Gubbiotti, G. Carlotti, T. Okuno, T. Shinjo, and M. Grimsditch. "Spin excitation of nanometric cylindrical dots in vortex and saturated magnetic states". *Phys. Rev. B* **70**, 172404 (2004).

[20] S. B. Choe, Y. Acremann, A. Scholl, A. Bauer, A. Doran, J. Stöhr, and H. A. Padmore. "Vortex core–driven magnetization dynamics". *Science* **304**, 420 (2004).

[21] M. Buess, R. Höllinger, T. Haug, K. Perzlmaier, U. Krey, D. Pescia, M. R. Scheinfein, D. Weiss, and C. H. Back. "Fourier transform imaging of spin vortex eigenmodes". *Phys. Rev. Lett.* **93**, 077207 (2004).

[22] X. Zhu, M. Malac, Z. Liu, H. Qian, V. Metlushko, and M. R. Freeman. "Broadband spin dynamics of permalloy rings in the circulation state". *Appl. Phys. Lett.* **86**, 262502 (2005).

[23] J. Raabe, C. Quitmann, C. H. Back, F. Nolting, S. Johnson, and C. Buehler. "Quantitative analysis of magnetic excitations in Landau flux-closure structures using synchrotron-radiation microscopy". *Phys. Rev. Lett.* **94**, 217204 (2005).

[24] K. Perzlmaier, M. Buess, C. H. Back, V. E. Demidov, B. Hillebrands, and S. O. Demokritov. "Spin-wave eigenmodes of permalloy squares with a closure domain structure". *Phys. Rev. Lett.* **94**, 057202 (2005).

[25] T. Gerrits, H. A. M. van den Berg, J. Hohlfeld, L. Bär, and T. Rasing. "Ultrafast precessional magnetization reversal by picosecond magnetic field pulse shaping". *Nature* **418**, 509 (2002).

[26] H. W. Schumacher, C. Chappert, P. Crozat, R. C. Sousa, P. P. Freitas, J. Miltat, J. Fassbender, and B. Hillebrands. "Phase coherent precessional magnetization reversal in microscopic spin valve elements". *Phys. Rev. Lett* **90**, 017201 (2003).

[27] H. W. Schumacher, C. Chappert, R. C. Sousa, P. P. Freitas, and J. Miltat. "Quasiballistic magnetization reversal". *Phys. Rev. Lett* **90**, 017204 (2003).

[28] G. N. Kakazei, P. E. Wigen, K. Y. Guslienko, V. Novosad, A. N. Slavin, V. O. Golub, N. A. Lesnik, and Y. Otani. "Spin-wave spectra of perpendicularly magnetized circular submicron dot arrays". *Appl. Phys. Lett.* **85**, 443 (2004).

[29] U. Ebels, L. D. Buda, K. Ounadjela, and P. E. Wigen. In : *Spin Dynamics in Confined Magnetic Structures I,* edited by B. Hillebrands and K. Ounadjela. Springer Verlag, Berlin (2002).

[30] M. R. Freeman, W. K. Hiebert, and A. Stankiewicz. "Time-resolved scanning Kerr microscopy of ferromagnetic structures (invited)". *J. Appl. Phys.* **83**, 6217 (1998).

[31] V. E. Demidov, S. O. Demokritov, B. Hillebrands, and M. Laufenberg. "Radiation of spin waves by a single micrometer-sized magnetic element". *Appl. Phys. Lett.* **85**, 2866 (2004).

[32] J. Rothman, M. Kläui, L. Lopez-Diaz, C. A. F. Vaz, A. Bleloch, J. A. C. Bland, Z. Cui, and R. Speaks. "Observation of a bi-domain state and nucleation free switching in mesoscopic ring magnets". *Phys. Rev. Lett.* **86**, 1098 (2001).

[33] S. P. Li, D. Peyrade, M. Natali, A. Lebib, Y. Chen, U. Ebels, L. D. Buda, and K. Ounadjela. "Flux closure structures in cobalt rings". *Phys. Rev. Lett.* **86**, 1102 (2001).

[34] F. J. Castano, C. A. Ross, C. Frandsen, A. Eilez, D. Gil, H. I. Smith, M. Redjdal, and F. B. Humphrey. "Metastable states in magnetic nanorings". *Phys. Rev. B* **67**, 184425 (2003).

[35] M. Kläui, C. A. F. Vaz, L. Lopez-Diaz, and J. A. C. Bland. "Vortex formation in narrow ferromagnetic rings". *J. Phys.: Condensed Matter* **15**, 985 (2003).

[36] T. Uhlig and J. Zweck. "Direct observation of switching processes in permalloy rings with Lorentz microscopy". *Phys. Rev. Lett.* **93**, 047203 (2004).

[37] S. X. Wang and A. M. Taratorin. *Magnetic Information Storage Technology.* Academic Press, London (1999).

[38] J. M. Luttinger and C. Kittel. "A note on the quantum theory of ferromagnetic resonance". *Helv. Phys. Acta* **21**, 480 (1948).

[39] L. Landau and E. Lifshitz. "On the theory of the dispersion of magnetic permeability in ferromagnetic bodies". *Physik. Z. Sowjetunion* **8**, 153 (1935).

[40] T. L. Gilbert. "A lagrangian formulation of the gyromagnetic equation of the magnetization field". *Phys. Rev.* **100**, 1243 (1955).

[41] R. Arias and D. L. Mills. "Extrinsic contributions to the ferromagnetic resonance response of ultrathin films". *Phys. Rev. B* **60**, 7395 (1999).

[42] D. Mills and S. Rezende. In : *Spin Dynamics in Confined Magnetic Structures II,* edited by B. Hillebrands and K. Ounadjela. Springer Verlag, Berlin (2003).

[43] M. Sparks. *Ferromagnetic Relaxation Theory.* Mc-Graw-Hill, New York (1966).

[44] H. Suhl. "Theory of the magnetic damping constant". *IEEE Trans. Magn.* **34**, 1834 (1998).

[45] C. Kittel. "On the theory of ferromagnetic resonance absorption". *Phys. Rev.* **73**, 155 (1948).

[46] L. R. Walker. "Magnetostatic modes in ferromagnetic resonance". *Phys. Rev.* **105**, 390 (1957).

[47] D. D. Stancil. *Theory of Magnetostatic Waves.* Springer Verlag, New York (1993).

[48] R. Damon and J. Eshbach. "Magnetostatic modes of a ferromagnetic slab". *J. Appl. Phys.* **31**, 104S (1960).

[49] B. A. Kalinikos and A. N. Slavin. "Theory of dipole-exchange spin wave spectrum for ferromagnetic films with mixed exchange boundary conditions". *J. Phys. C* **19**, 7013 (1986).

[50] T. Schneider. *Bestimmung und Beeinflussung der Phaseneigenschaften von Spinwellen in Yttrium-Eisen-Granat-Wellenleiterstrukturen.* Diplomathesis, TU Kaiserslautern (2005). Available at *http://www.physik.uni-kl.de/w_hilleb/phd_diploma.html.*

[51] T. D. Rossing. "Chladni's law for vibrating plates". *Am. J. Phys.* **50**, 271 (1982).

[52] D. Kverno and J. Nolen. "Investigation of the vibration of circular, square and rectangular plates with unbound edges". Available at *http://www.phy.davidson.edu/stuhome/derekk/chladni/pages/menu.htm.*

[53] M. Buess, T. P. J. Knowles, R. Höllinger, T. Haug, U. Krey, D. Weiss, D. Pescia, M. R. Scheinfein, and C. H. Back. "Excitations with negative dispersion in a spin vortex". *Phys. Rev. B* **71**, 104415 (2005).

[54] S. O. Demokritov and B. Hillebrands. In : *Spin Dynamics in Confined Magnetic Structures I,* edited by B. Hillebrands and K. Ounadjela. Springer Verlag, Berlin (2002).

[55] M. Sparks. "Magnetostatic modes in an infinite circular disk". *Solid State Comm.* **8**, 731 (1970).

[56] G. T. Rado and J. R. Weertmann. "Spin-wave resonance in a ferromagnetic metal". *J. Phys. Chem. Solids* **11**, 315 (1959).

[57] K. Y. Guslienko, S. O. Demokritov, B. Hillebrands, and A. N. Slavin. "Effective dipolar boundary conditions for dynamic magnetization in thin magnetic stripes". *Phys. Rev. B* **66**, 132402 (2002).

[58] B. Heinrich and J. Bland. *Ultrathin Magnetic Structures II.* Springer Verlag, Berlin (1994).

[59] G. Woltersdorf. *Spin pumping and two magnon scattering in magnetic multilayers.* Dissertation, Simon Fraser University, Burnaby, Canada (2004).

[60] W. Dietrich, W. E. Proebster, and P. Wolf. "Nanosecond switching in thin magnetic films". *IBM Journal of Research and Development* **4**, 189 (1960).

[61] T. J. Silva, C. S. Lee, T. M. Crawford, and C. T. Rogers. "Inductive measurement of ultrafast magnetization dynamics in thin-film permalloy". *J. Appl. Phys.* **85**, 7849 (1999).

[62] S. Ganzer. *Dynamisches Verhalten von Magneto-Kopplern und ferromagnetischen Nano-Schichten.* Dissertation, Universität Regensburg, Regensburg, Germany (2004).

[63] J. Kerr. "On the magnetism of light and the illumination of magnetic lines of force". *Rep. Brit. Ass.* **S5**, 85 (1876).

[64] J. Kerr. "On the rotation of the plane of polarization by reflection from the pole of a magnet". *Phil. Mag.* **3**, 321 (1876).

[65] A. Hubert and R. Schäfer. *Magnetic Domains - The Analysis of Magnetic Microstructures.* Springer Verlag, Berlin, Heidelberg (2000).

[66] Bergmann and Schaefer. *Optics of waves and particles.* de Gruyter, Berlin (1999).

[67] T. Gerrits, H. A. M. van den Berg, J. Hohlfeld, O. Gielkens, K. J. Veenstra, L. Bär, and T. Rasing. "Picosecond precessional magnetization reversal by magnetic field pulse shaping". *IEEE Trans. Magn.* **38**, 2484 (2002).

[68] M. Buess, T. Haug, M. R. Scheinfein, and C. H. Back. "Micromagnetic dissipation, dispersion and mode conversion in thin permalloy platelets". *Phys. Rev. Lett.* **94**, 127205 (2005).

[69] A. Puzic, B. V. Waeyenberge, K. W. Chou, P. Fischer, H. Stoll, G. Schütz, T. Tyliszczak, K. Rott, H. Brückl, G. Reiss, I. Neudecker, T. Haug, M. Buess, and C. H. Back. "Spatially resolved ferromagnetic resonance: Imaging of ferromagnetic eigenmodes". *J. Appl. Phys.* **97**, 10E704 (2005).

[70] B. E. Argyle, E. Terrenzio, and J. C. Slonczewski. "Magnetic vortex dynamics using the optical Cotton-Mouton effect". *Phys. Rev. Lett.* **53**, 190 (1984).

[71] M. Buess. *Pulsed Precessional Motion*. Dissertation, ETH Zürich, ISBN: 3-8325-0981-X (2005).

[72] M. R. Scheinfein. The LLG code can be found at *http://llgmicro.home.mindspring.com/*.

[73] Object Oriented MicroMagnetic Framework. The OOMMF code can be found at *http://math.nist.gov/oommf/*.

[74] B. Heinrich and J. F. Cochran. "Ultrathin metallic magnetic films: magnetic anisotropies and exchange interactions". *AinP* **42**, 523 (1993).

[75] M. Brockmann, M. Zölfl, S. Miethaner, and G. Bayreuther. "In-plane volume and interface magnetic anisotropies in epitaxial Fe films on GaAs(001)". *J. Magn. Magn. Mat.* **198-199**, 384 (1999).

[76] R. Urban, G. Woltersdorf, and B. Heinrich. "Gilbert damping in single and multilayer ultrathin films: Role of interfaces in nonlocal spin dynamics". *Phys. Rev. Lett.* **87**, 217204 (2001).

[77] P. R. Emtage. "Generation of magnetostatic surface waves by a microstrip". *J. Appl. Phys.* **53**, 5122 (1982).

[78] Sonnet. High Frequency Electromagnetic Software, available at *http://www.sonnetsoftware.com*.

[79] J. Pelzl, R. Meckenstock, D. Spoddig, F. Schreiber, J. Pflaum, and Z. Frait. "Spin–orbit-coupling effects on g-value and damping factor of the ferromagnetic resonance in Co and Fe films". *J. Phys. Condens. Matter* **15**, S451 (2003).

[80] G. Counil, J.-V. Kim, T. Devolder, and C. Chappert. "Spin wave contributions to the high-frequency magnetic response of thin films obtained with inductive methods". *J. Appl. Phys.* **95**, 5646 (2004).

[81] Z. Frait and D. Fraitová. "Ferromagnetic resonance and surface anisotropy in iron single crystals". *J. Magn. Magn. Mat.* **15-18**, 1081 (1980).

[82] V. Savonov and H. N. Bertram. "Linear stochastic magnetization dynamics and microscopic relaxation mechanisms". *J. Appl. Phys.* **94**, 529 (2003).

[83] J. Lindner, K. Lenz, E. Kosubek, K. Baberschke, D. Spodding, R. Meckenstock, J. Pelzl, Z. Frait, and D. L. Mills. "Non-Gilbert-type damping of the magnetic relaxation in ultrathin ferrromagnets: Importance of magnon-magnon scattering". *Phys. Rev. B* **68**, 060102(R) (2003).

[84] Y. Acremann, M. Buess, C. H. Back, M. Dumm, G. Bayreuther, and D. Pescia. "Ultrafast generation of magnetic fields in a Schottky diode". *Nature* **414**, 51 (2001).

[85] M. Bauer, R. Luposnik, J. Fassbender, and B. Hillebrands. "Suppression of magnetic-field pulse-induced magnetization precession by pulse tailoring". *Appl. Phys. Lett.* **76**, 2758 (2000).

[86] Z. Celinski and B. Heinrich. "Ferromagnetic resonance linewidth of Fe ultrathin films grown on a bcc Cu substrate". *J. Appl. Phys.* **70**, 5935 (1991).

[87] T. Shinjo, T. Okuno, R. Hassdorf, K. Shigeto, and T. Ono. "Magnetic vortex core observation in circular dots of permalloy". *Science* **289**, 930 (2000).

[88] J. Raabe, R. Pulwey, R. Sattler, T. Schweinböck, J. Zweck, and D. Weiss. "Magnetization pattern of ferromagnetic nanodisks". *J. Appl. Phys.* **88**, 4437 (2000).

[89] A. Wachowiak, J. Wiebe, M. Bode, O. Pietzsch, M. Morgenstern, and R. Wiesendanger. "Direct observation of internal spin structure of magnetic vortex cores". *Science* **298**, 577 (2002).

[90] M. Schneider, H. Hoffmann, S. Otto, T. Haug, and J. Zweck. "Stability of magnetic vortices in flat submicron permalloy cylinders". *J. Appl. Phys.* **92**, 1466 (2002).

[91] M. Heumann, T. Uhlig, and J. Zweck. "True single domain and configuration-assisted switching of submicron permalloy dots observed by electron holography". *Phys. Rev. Lett.* **94**, 077202 (2005).

[92] Webpage of the group: *http://ghost.fisica.unipg.it*.

[93] M. Buess, Y. Acremann, A. Kashuba, C. H. Back, and D. Pescia. "Pulsed precessional motion on the "back of an envelope"". *J. Phys.: Condens. Matter* **15**, R1093 (2003).

[94] K. Y. Guslienko, W. Scholz, R. W. Chantrell, and V. Novosad. "Vortex-state oscillations in soft magnetic cylindrical dots". *Phys. Rev. B* **71**, 144407 (2005).

[95] B. A. Ivanov and C. E. Zaspel. "High frequency modes in vortex-state nanomagnets". *Phys. Rev. Lett.* **94**, 027205 (2005).

[96] R. Zivieri and F. Nizzoli. "Theory of spin modes in vortex-state ferromagnetic cylindrical dots". *Phys. Rev. B* **71**, 014411 (2005).

[97] A. A. Thiele. "Steady-state motion of magnetic domains". *Phys. Rev. Lett.* **30**, 230 (1973).

[98] K. Y. Guslienko, X. F. Han, D. J. Keavney, R. Divan, and S. D. Bader. "Magnetic vortex core dynamics in cylindrical ferromagnetic dots". *Phys. Rev. Lett.* **96**, 067205 (2006).

[99] J. P. Park and P. A. Crowell. "Interactions of spin waves with a magnetic vortex". *Phys. Rev. Lett.* **95**, 167201 (2005).

[100] F. Hoffmann, G. Woltersdorf, K. Perzlmaier, and C. H. Back (2006). In preparation. See also F. Hoffmann, Diploma-Thesis, Universität Regensburg, Regensburg, Germany.

[101] D. Chen, J. A. Brug, and R. B. Goldfarb. "Demagnetizing factors for cylinders". *IEEE-Transactions-on-Magnetics* **27**, 3601 (1991).

[102] G. Gubbiotti, O. Kazakova, G. Carlotti, M. Hanson, and P. Vavassori. "Spin-wave spectra in nanometric elliptical dots". *IEEE Trans. Mag.* **39**, 2750 (2003).

[103] C. Bayer, S. O. Demokritov, B. Hillebrands, and A. N. Slavin. "Spin-wave wells with multiple states created in small magnetic elements". *Appl. Phys. Lett.* **82**, 607 (2003).

[104] S. O. Demokritov, B. Hillebrands, and A. N. Slavin. "Brillouin light scattering studies of confined spin waves: linear and non-linear confinement". *Physics Reports* **348**, 441 (2001).

[105] F. Giesen, J. Podbielski, T. Korn, M. Steiner, and D. Grundler. "Hysteresis and control of ferromagnetic resonances in rings". *Appl. Phys. Lett.* **86**, 112510 (2005).

[106] F. Giesen, J. Podbielski, T. Korn, and D. Grundler. "Multiple ferromagnetic resonance in mesoscopic permalloy rings". *J. Appl. Phys.* **97**, 10A712 (2005).

[107] L. J. Heyderman, C. David, M. Kläui, C. A. F. Vaz, and J. A. C. Bland. "Nanoscale ferromagnetic rings fabricated by electron-beam lithography". *J. Appl. Phys.* **93**, 10011 (2003).

[108] Y. G. Yoo, M. Kläui, C. A. F. Vaz, L. J. Heyderman, and J. A. C. Bland. "Switching field phase diagram of Co nanoring magnets". *Appl. Phys. Lett.* **82**, 2470 (2003).

[109] C. Kittel. "Excitation of spin waves in a ferromagnet by a uniform rf field". *Phys. Rev.* **110**, 1295 (1958).

[110] F. Giesen. *Magnetization dynamics of nanostructured ferromagnetic rings and rectangular elements.* Dissertation, Universität Hamburg, Hamburg, Germany (2005).

[111] R. M. Bozworth. *Ferromagnetism.* D. van Nostrand Company, New York (1951).

[112] M. Kläui, C. A. F. Vaz, J. A. C. Bland, and L. J. Heyderman. "Domain wall coupling and collective switching in interacting mesoscopic ring magnet arrays". *Appl. Phys. Lett.* **86**, 032504 (2005).

[113] D. M. Pozar. *Microwave engineering.* John Wiley & Sons, Inc., New York (1998).

[114] Agilent Technologies. Agilent AN 1287-2 – Exploring the Architecture of Network Analyzers. The application note can be found at *http://emlab.uiuc.edu/ece451/appnotes/Architecture_VNAs.*

[115] J. F. Gregg. In : *Spin Dynamics in Confined Magnetic Structures I,* edited by B. Hillebrands and K. Ounadjela. Springer Verlag, Berlin (2002).

[116] O. Karlqvist. "Calculations of the magnetic field in the ferromagnetic layer of a magnetic drum". *Trans. R. Soc. Technol. (Stockholm)* **86**, 1 (1945).

[117] J. C. Mallinson. *The Foundations of Magnetic Recording, 2nd ed.* Academic Press, San Diego (1993).

[118] Zincke and Brunswig. *Hochfrequenztechnik 1.* Springer, Berlin (1999).

[119] J. C. Rautio and V. Demir. "Microstrip conductor loss models for electromagnetic analysis". *IEEE Trans. on Microwave Theory and Techniques* **51**, 915 (2003).

[120] J. D. Jackson. *Classical Electrodynamics.* Walter de Gruyter, Berlin (2001).

[121] D. Pain, M. Ledieu, O. Acher, A. L. Adenot, and F. Duverger. "An improved permeameter for thin film measurements up to 6 GHz". *J. Appl. Phys.* **85**, 5151 (1999).

[122] T. L. Monchesky, B. Heinrich, R. Urban, K. Myrtle, M. Klaua, and J. Kirschner. "Magnetoresistance and magnetic properties of Fe/Cu/Fe/GaAs(100)". *Phys. Rev. B* **60**, 10242 (1999).

[123] T. Okuno, K. Shigeto, T. Ono, K. Mibu, and T. Shinjo. "MFM study of magnetic vortex cores in circular permalloy dots: behavior in external field". *J. Mag. Mag. Mater.* **240**, 1 (2002).

Acknowledgements

Last but not least I want to thank everyone who contributed to this work in terms of simulations, sample preparations, measurements, and any other kind of support. In particular I want to thank:

- first of all my supervisor Prof. Dr. Christian H. Back for the opportunity to make use of the excellently equipped laboratories and his permanent willingness for fruitful and motivating discussions. He was always very concerned in the progress of the work and provided a very pleasant and prolific working atmosphere.
- Prof. Dr. Dieter Weiss for the access to the clean room facility and for being referee of the dissertation. Furthermore according the sample fabrication I want to thank the whole work group of Prof. Weiss and in particular Josef Biberger for the unhesitant support.
- Dr. Georg Woltersdorf for the fabrication of the high quality ultrathin Fe/GaAs films, the FMR measurements, and for letting me profiting of his impressive knowledge which helped to solve numerous problems and often contributed to a better comprehension of many physical concepts. Moreover, his proofreads are greatly acknowledged.
- Korbinian Perzlmaier and Dr. Rainer Höllinger for the micromagnetic simulations.
- Tobias Stöckl for the construction of experimental setup hardware.
- Frank Hoffmann for time resolved scanning Kerr measurements.
- Dr. Matthieu Bailleul for a lot of advices and support concerning the high frequency technology.
- Dr. Mathias Kläui for the successful collaboration, for altering the inter-ring distance by means of focused ion beam, and his contributions concerning the properties of ring elements. In this context I want to thank also Dr. Laura J. Heyderman, Dirk Backes, and Dr. Carlos A. F. Vaz for the fabrication of the high quality ring elements.
- Dr. Gianluca Gubbiotti for the Brillouin light scattering measurements and the successful collaboration concerning the 200 nm permalloy disks.

- Dr. Hermann Stoll and Aleksander Puzic for the share of knowledge and equipment of high frequency technology.
- Dr. Christoph Quitmann and Dr. Frithjof Nolting from the SIM beamline at the Swiss Light Source for the photo emission electron microscopy measurements.
- Dr. Matthias Buess, Michael Binder, Matthias Kiessling, Alexander Weber, and Dr. Stefan Ganzer for sharing the office, the lab, and a good time.

Additionally, I would like to remark, that enjoying and profiting from the friendly and cooperative atmosphere within the team and the members of the chair of Prof. Back was a great pleasure.

Financial support from the DFG through the Priority Programme 1133 'Ultrathin Fast Magnetization Processes' is gratefully acknowledged.

Finally many thanks are addressed to my parents for their unquestioning support, and

...to Doris and Luca.